FINITE ELEMENT FORMULATIONS FOR KIRCHHOFF-LOVE MICROPLATES

A THESIS SUBMITTED TO
THE GRADUATE SCHOOL OF NATURAL AND APPLIED SCIENCES
OF
MIDDLE EAST TECHNICAL UNIVERSITY

BY

MURAT KANDAZ

IN PARTIAL FULFILLMENT OF THE REQUIREMENTS
FOR
THE DEGREE OF DOCTOR OF PHILOSOPHY
IN
MECHANICAL ENGINEERING

JULY 2020

Approval of the thesis:

FINITE ELEMENT FORMULATIONS FOR KIRCHHOFF-LOVE MICROPLATES

submitted by **MURAT KANDAZ** in partial fulfillment of the requirements for the degree of **Doctor of Philosophy in Mechanical Engineering Department, Middle East Technical University** by,

Prof. Dr. Halil Kalıpçılar
Dean, Graduate School of **Natural and Applied Sciences** ________________

Prof. Dr. M. A. Sahir Arıkan
Head of Department, **Mechanical Engineering** ________________

Assoc. Prof. Dr. Hüsnü Dal
Supervisor, **Mechanical Engineering Dept., METU** ________________

Examining Committee Members:

Prof. Dr. Suha Oral
Mechanical Engineering Dept., METU ________________

Assoc. Prof. Dr. Hüsnü Dal
Mechanical Engineering Dept., METU ________________

Assoc. Prof. Dr. Uğur Polat
Civil Engineering Dept., METU ________________

Assoc. Prof. Dr. Mehmet Ünlü
Electrical and Electronics Engineering Dept., TOBB-ETU ________________

Assoc. Prof. Dr. Cihan Tekoğlu
Mechanical Engineering Dept., TOBB-ETU ________________

Date: 08.07.2020

I hereby declare that all information in this document has been obtained and presented in accordance with academic rules and ethical conduct. I also declare that, as required by these rules and conduct, I have fully cited and referenced all material and results that are not original to this work.

Name, Surname: Murat Kandaz

Signature :

ABSTRACT

FINITE ELEMENT FORMULATIONS FOR KIRCHHOFF-LOVE MICROPLATES

Kandaz, Murat
Ph.D., Department of Mechanical Engineering
Supervisor: Assoc. Prof. Dr. Hüsnü Dal

July 2020, 136 pages

Micro- and nano-electromechanical systems (MEMS-NEMS) are integral parts of the modern world today and have gained importance since they were first introduced. There is still a huge demand for accurate electromechanical analyses of MEMS devices in order to reach even better design and manufacturing methods. It is vital that these devices are accurately modelled and analyzed based on the physical phenomena occurring within their inner structure as a result of the conditions they are subjected to.

Classical continuum mechanics approaches are highly accurate for large scale structures where the structural length scale is several order of magnitudes higher than the microstructural length scale. However, they fail to describe the mechanical behavior of smaller parts, i.e. MEMS-NEMS devices, as the structural length scale becomes comparable to grain size. Hence, the effect of discontinuities in field variables at grain boundaries and other imperfections should be considered. This phenomenon is known as size effect or scale effect. To model such structures in the scale of microns, several techniques have been developed, the dominating and most well-proven being the modified gradient elasticity theories. Within this context, micron-scaled parts and materials are modelled using gradients, and in turn, higher order terms are introduced with relevant length scale parameters into the constitutive theory which take the size effects into account.

In this study, sample microstructures and MEMS-NEMS devices are analyzed using finite element method (FEM) based on variational formulation of modified strain gradient theories. In this framework, new finite elements are developed and verified for Kirchhoff-Love plate theory, making it possible to model complex planar MEMS-NEMS geometries. Structural behavior is elaborated using codes based on numerical analyses, that are also developed within this study. The results are then compared with experimental results and literature for verification. The convergence and validity of model results and the extent upto which they are applicable within the general continuum approach are also discussed. Length scale parameters for gold microstructures are proposed based on theoretical-computational-experimental framework.

Keywords: size effect, higher order finite element method, modified strain gradient theory, length scale parameter, microplates, MEMS, higher order elasticity, higher order Kirchhoff-Love plate theory

ÖZ

KİRCHHOFF-LOVE MİKROPLAKALARI İÇİN SONLU ELEMANLAR FORMÜLASYONLARI

Kandaz, Murat
Doktora, Makina Mühendisliği Bölümü
Tez Yöneticisi: Doç. Dr. Hüsnü Dal

Temmuz 2020 , 136 sayfa

Mikro- ve nano-elektromekanik sistemler (MEMS-NEMS) yaşadığımız modern dünyanın vazgeçilmez parçalarıdır ve ilk kullanmaya başlanıldığı günden beri önem kazanmaya devam etmektedir. Halen daha da iyi tasarım ve üretim yöntemlerine ulaşmak için ilgili yapılarda daha doğru ve hassas elektromekanik analizlere ihtiyaç bulunmaktadır. Bu yapıların maruz kaldıkları şartlara bağlı olarak iç yapılarındaki fiziksel değişim ve olayları baz alarak yapılacak hassas modelleme ve analizler büyük önem taşımaktadır.

Klasik sürekli ortam mekaniği yaklaşımları, büyük boyutlardaki yapılar için doğru sonuçlar vermektedir. Ancak MEMS-NEMS yapıları gibi boyutların birkaç tanecik boyutunda mikro boyuttaki parçaların mekanik davranışını modelleyememektedirler. Bu yüzden alan değişkenlerinin tanecik kenarlarındaki süreksizlikleri ve diğer yapısal bozukluklar dikkate alınmalıdır. Bu fenomen boyut etkisi olarak bilinmektedir. Mikron seviyelerindeki yapıları modellemek için, en etkili ve kanıtlanmış olanı modifiye gradyan elastisite kuramları olmak üzere çok çeşitli yöntemler geliştirilmiştir. İlgili teorilerde mikron boyutta olan parçalar ve malzemeler, gradyanlar kullanarak, ve bunun sonucu olarak esas yapısal denklemlere boyut etkisi parametrelerini içeren yüksek mertebe terimlerinin eklenerek modellenmektedir.

Bu çalışmada örnek mikroyapılar ve MEMS-NEMS yapıları, modifiye gradyan teorilerinin varyasyonel formülasyonuna dayalı sonlu elemanlar yöntemi (SEY) kullanılarak analiz edilmiştir. Bu kapmsada, Kirchhoff-Love plak teorisi için yeni sonlu elemanlar geliştirilmiş, dolayısıyla komplike şekillere sahip düzlemsel MEMS-NEMS yapılarının modellenmesi mümkün olmuştur. İlgili yapıların davranışları sayısal analiz tabanlı olarak gene bu çalışma içerisinde geliştirilen bilgisayar kodları ile gerçekleştirilmiştir. Sonuçlar, yapılan deneyler ve literatürdeki bulgular ile karşılaştırılmıştır. Genel sürekli ortam yaklaşımı içerisinde model sonuçlarının doğruluğu ve yakınsama davranışları ile hangi derecede uygulanabilir olduğu da ayrıca tartışılmıştır. Sözü edilen kuramsal-hesaplamalı-deneysel çerçeve kapsamında altın mikroyapılar için boyut etkisi parametreleri önerilmiştir.

Anahtar Kelimeler: boyut etkisi, yüksek mertebe sonlu elemanlar yöntemi, modifiye gerinim gradyanı teorisi, boyut ölçeği parametresi, mikroplakalar, MEMS, yüksek mertebe elastisite, yüksek mertebe Kirchhoff-Love plaka teorisi

To my Amazing Family.

You always let this heart be still.

ACKNOWLEDGMENTS

The financial support provided by Scientific and Technological Research Council of Turkey (TUBITAK) through grant scheme 1001 under grant number 116M258 is gratefully acknowledged.

TABLE OF CONTENTS

LIST OF TABLES

TABLES

LIST OF FIGURES

FIGURES

LIST OF ABBREVIATIONS

Multi-Word Terms

1D	One-dimensional
2D	Two-dimensional
3D	Three-dimensional
AFM	Atomic force microscopy/microscope
DOF	Degree of freedom
FEA	Finite element analysis
FGM	Functionally graded materials
MCST	Modified couple stress theory
MEMS	Micro-electro mechanical systems
MSGT	Modified strain gradient theory
NEMS	Nano-electro mechanical systems

Operators

A	Assembly of finite element contributions at the local element nodes
$\mathrm{arg}[\bullet]$	Argument of a function
$\mathrm{curl}[\bullet]$	Curl
$\mathrm{div}[\bullet]$	Divergence
$\mathrm{inf}[\bullet]$	Infimum of a set of quantities
$\mathrm{tr}[\bullet]$	Trace operator
$\delta[\bullet]$	Variation
∂	Boundary of a subset of a topological space, i.e. closure without the interior space
$\partial_{[\bullet]}$	Differential operator, i.e. differentiation with respect to $[\bullet]$

$\nabla[\bullet]$	Gradient operator
$\nabla^p[\bullet]$	Permutational gradient, i.e. $\nabla^p[\bullet] = [\bullet]_{jk,i} + [\bullet]_{ki,j} + [\bullet]_{ij,k}$.
$[\bullet]^T$	Transpose operator (second order)
$[\bullet]^{\overset{13}{T}}$	Transpose operator (third order), i.e. $\left([\bullet]^{\overset{13}{T}}\right)_{ijk} = [\bullet]_{kji}$
$[\bullet]^{\overset{23}{T}}$	Transpose operator (third order), i.e. $\left([\bullet]^{\overset{23}{T}}\right)_{ijk} = [\bullet]_{ikj}$
$\cdot$	Dot product
$:$	Double contraction, a.k.a double dot product
$\vdots$	Triple contraction, a.k.a. triple dot product
$\otimes$	Dyadic product

Continuum Mechanics and Elasticity

$\mathcal{A}$	Area (generic)
$\mathbf{b}$	Body force tensor
$\mathcal{B}$	3D Riemannian manifold in an Eucledian space
d	Displacement with respect to applied force
D	Isotropic plate rigidity
E	Isotropic elastic modulus
h	Thickness (generic)
I	Area moment of inertia of a beam cross section
l, l_0, l_1, l_2	Length scale parameters
L	Length of a plate or a beam
$\mathbf{m}$	Couple stress tensor
M	Bending moment
$\mathbf{n}$	Surface normal tensor
$\mathbf{p}$	Pressure gradient tensor
q	External distributed loads
Q	Higher order bending moment
$\mathbf{u}$	Displacement tensor

$\mathbf{t}$	Surface traction tensor
V	Shear force
$\mathcal{V}$	Volume (generic)
w	Vertical displacement
W	Width of a plate
x, y, z	Axes of Cartesian coordinate system
$\boldsymbol{\gamma}$	Dilatation gradient tensor
$\boldsymbol{\varepsilon}$	Elastic strain
$\boldsymbol{\eta}$	Strain gradient tensor
$\boldsymbol{\eta^s}$	Antisymmetric strain gradient tensor
$\boldsymbol{\eta^s}$	Symmetric strain gradient tensor
$\boldsymbol{\eta^0}$	Volumetric strain (expansion-contraction) gradient tensor
$\boldsymbol{\eta^1}$	Deviatoric strain (stretch) gradient tensor
θ	Rotation
$\boldsymbol{\theta}$	Rotation tensor
λ	First Lamé constant
κ	Rotation gradient, i.e. curvature
μ	Shear modulus
ν	Poisson's ratio
$\mathit{\Pi}$	Potential energy function
$\mathit{\Pi}^{ext}$	Work done by external forces
$\mathit{\Pi}^{int}$	Energy stored (in a body)
ρ	Density
$\boldsymbol{\sigma}$	Cauchy stress tensor
$\boldsymbol{\tau}$	Double stress tensor
$\boldsymbol{\chi}$	Rotation gradient (or curvature) tensor
ψ	Free energy function

ψ_{C}	Free energy function incorporating strain tensor
ψ_{H}	Free energy function incorporating strain gradient tensor
$\mathbf{1}$	Unit tensor

Finite Element Method

$\mathbf{d}$, $\mathbf{d}_e$	Nodal displacement vector
$\mathbf{D}$	Global nodal displacement vector
Err	Error function based on residuals
$\mathbf{f}$, $\mathbf{f}_e$	Nodal force vector
F	Nodal force
F_c	Contact force in a MEMS structure
F_e	Electrostatic force in a MEMS structure
F_r	Release force in a MEMS structure
$\mathbf{F}$	Global nodal force vector
$\mathbf{k}$, $\mathbf{k}_e$	Element stiffness matrix
$\mathbf{K}$	Global stiffness matrix
$\mathbf{N}$	Shape function vector
N_i^j	Shape function at the i'th node corresponding to the j'th DOF
n	Number of finite elements
n_{DOF}	Number of degrees of freedoms per node
n_{elem}	Number of finite elements
n_{nodes}	Number of nodes of a finite element

Proper Nouns

ACM	Adini-Clough-Melosh (developers of the relevant finite element)
BFS	Bogner-Fox-Schmit (developers of the relevant finite element)

CHAPTER 1

INTRODUCTION

1.1 Motivation and Problem Definition

The potential application areas of MEMS-NEMS are almost limitless and steadily growing given their small size, low weights, ease of implementation in integrated circuits, low energy consumption and low manufacturing costs. These features earn them vast utilization areas from automotive to defense industry, from biomedical engineering to consumer electronics, and from optics to communication systems. MEMS and NEMS are used in pressure sensors, accelerometers, computer and smart phone hardware, gyros, resonators, micro-power terminals, actuators, RF switches and biomedical devices [9, 10, 11, 12, 13, 14, 15, 16, 17, 18, 19, 20, 21].

The feature size of MEMS and NEMS devices is decreasing day by day and approaching to orders of a few microns and nanometers respectively as given in Figure 1.1. The deformations are almost always in the elastic regime during their applications. It is in fact known that behavior of materials change both elastically and plastically as their feature size decrease to certain limits [22, 23, 24, 25, 26, 27]. This phenomenon is known as *size effect* or *scale effect* in structures which have feature sizes and dimensions in the order of magnitude of their grain sizes, i.e. at mesoscale level as seen in Figure 1.2. Several parameters regarding crystallographic texture, grain morphology, surface morphology, self-diffusion, secondary grain growth, defect structure, and inter-diffusion [28, 29, 30] are responsible for size effects. These factors hinder deformation and make structures at mesoscale level relatively stiffer than their counterparts, making classical theories of continuum mechanics invalid.

In fact, the first of many studies considering these led to the effect named after its

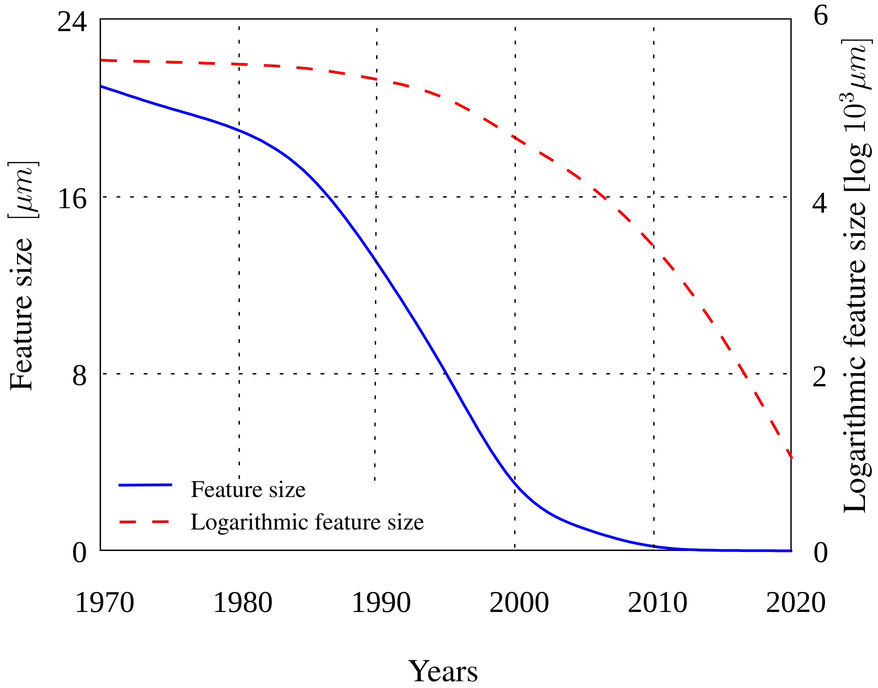

Figure 1.1: Feature sizes of MEMS and NEMS with years

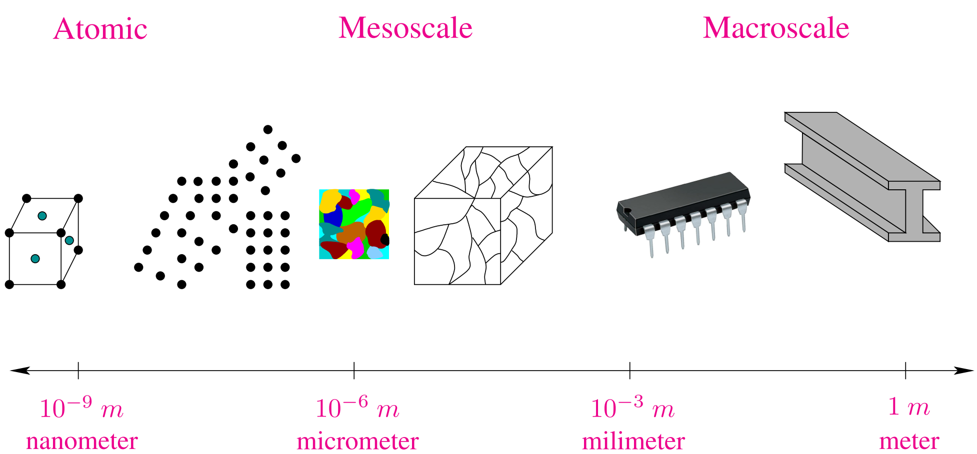

Figure 1.2: Material length scales per [2]

originators, i.e. Hall-Petch effect, that inversely relates yield strength with grain size [31, 32]. In any microstructure, manufacturing and operating conditions, particularly temperature and loading rate, also affect these parameters, as also investigated in literature [33, 34, 35, 36, 37, 38, 39].

Being used in extensive industries and products, requirements and specifications vary for MEMS and NEMS devices depending on application. In turn, they can be made of metallic, polymeric, silicon-based or functionally graded materials. This study focuses on MEMS structures made of gold, since several properties render it a popular material in MEMS and NEMS applications. It possesses excellent mechanical and electrical properties such as electrical conductivity, chemical inertness, resistance to surface wear, relatively lower residual stress after manufacturing due to thermomechanical loads, and relatively lower thermal fluctuation. Size effects in gold micro-structures were also experimentally shown under tensile [40, 41], compressive [42, 43], bending [44, 45, 46] tests, respectively. Also, many studies and tests towards understanding microstructure of gold have been performed in literature, given the fact that gold is one of the most popular materials in MEMS-NEMS community [47, 48, 49, 50, 51, 52, 53, 54].

The early works regarding modelling of size effect in engineering materials were oriented towards understanding the physical phenomena rather than accurate mathematical description. That is for instance, Voigt's pioneering work [55] provided an extensive approach containing kinematics, balance laws, and constitutive relations, but yielded a complicated differential equations set, solutions of which included further simplifying assumptions [56].

1960's became a so-called "renaissance" period for higher order theories [56]. Couple stress concept was introduced [57] which depended on Voigt's work [55], in which surface loads are in fact both force and moment vectors. New theories making use of this concept were introduced in full compliance with continuum approach [58, 59, 60, 61, 62, 63]. Eringen also included micro inertia (which allows incorporation of dynamic effects) and founded *Micropolar Elasticity* [64]. He also developed the notion of *Nonlocal Elasticity* [65] and compiled years of research in his invaluable book [66]. Unlike classical continuum theory, which assumes that the stress at a point is a function of strain at that particular point, the founding principle of nonlocal elasticity is the assumption that the stress at a point is a function of strain variaton in the neighbourhood of the continuum as well [67].

In 2000's, the development of computing power and the increasing demand in microstructures led to pioneering works in nonlocal theory. Many landmark studies and comprehensive contributions were made considering the theories mentioned above.

Those included advanced materials such as functionally graded materials (FGM), as well as various boundary conditions applied in real microstructures [68, 69, 70, 71, 72, 73, 74, 75, 76, 77, 78, 79, 80, 81].

The general theories considering MEMS and NEMS were also developed first in 1960's. Originally, they were oriented towards modelling microstructures with improved accuracy as well as finding satisfactory solutions to problems of singularities in classical elasticity theory, e.g. concentrated loads, regions around crack tips, negative slope regime in stress-strain curve of strain softening [60, 57, 82, 62, 83, 84]. Most of the originating theories of higher order elasticity are also known as "MTK theories" after capitals of Mindlin, Toupin and Koiter. Fleck and Hutchinson [85, 86, 87] used the previous concept of strain gradients and extended them in an improved *Strain Gradient Theories* (SGT) pioneering the framework of higher order theories implemented in this study, originally oriented towards solving plasticity problems. These were fundamentally similar to the nonlocal theories introduced by Eringen [88]. Lam et al. [6] decreased this number from five to three in SGT using new equilibrium conditions and new strain and stress metrics, leading to *Modified Strain Gradient Theory* (MSGT). Yang et al. [89] introduced a new equilibrium equation which decreased the number of independent length scale parameters from two to one, also leading to *Modified Couple Stress Theory* (MCST).

MSGT has been proven to be an accurate, consistent, and mathematically complete model. This enabled the intensive use of MSGT in the analysis microstructures and MEMS [90, 91, 92, 93, 94, 95, 96, 97, 98, 99, 100, 101, 102, 103]. The implementation of MCST can be interpreted as a modification of MSGT, reducing the number of length scale and other parameters from three to one, providing practicality especially in beam applications [104, 105, 106, 107, 108, 95, 109, 110, 111, 112, 113, 114, 115, 116, 117].

Since MEMS and NEMS are evolving to have more geometrically complex shapes, one-dimensional (1D) beam solutions are becoming insufficient in modelling, with the need for two-dimensional (2D) solutions. Despite there are many studies regarding implementation of higher order theories on microbeams as above, microplates did not receive such attention so far [118]. Several valuable contributions provide analytical plate solutions [5, 119, 120, 121, 122], but are applicable to ideal boundary conditions and geometries. However, stable and convergent finite element implementations allow the analysis and design of MEMS and NEMS structures of any geometry.

The most common and proven method to obtain general quadrilateral shapes is discrete Kirchhoff-Love quadrilaterals (DKQ) and discrete Kirchhoff-Love triangles, based on eight serendipity shape functions [123]. Here, the Kirchhoff-Love theory is applied only at certain discrete points on the element boundary, relaxing the requirement of having C^1-continuity [124]. Similarly, forming a general quadrilateral by combining four triangles are also used by Clough and Felippa [125] and de Veubeke [126] to obtain conventional Kirchhoff-Love plate elements applicable to general quadrilaterals. These methods apply static condensation at internal nodes of the triangles forming the quadrilateral. In order to relax Kirchhoff-Love theory requirements, Reissner-Mindlin (RM) theory for moderately thick plates is applied. Therein, the continuity requirement for the displacement interpolation is reduced to C^0 instead of C^1. However, RM plate elements suffer from shear locking. Quadrilateral elements that overcome shear locking problem and decrease parasitic effects have been developed by e.g. [127, 128, 129, 130, 131, 132, 133]. Triangular elements followed the same path. Although many successfully proven non-conforming Kirchhoff-Love elements in C^1 have been formulated [3, 134, 135, 136, 137, 138], insensitiveness to aspect ratio and failure in several patch tests have led to implementations in RM theory in C^0 or similar methods described above to avoid C^1 requirements. Although discrete penalty constraints, reduced interpolation procedures, penalty-strain interpolations, and penalty parameter modifications have been introduced, several schemes may lead to locking [139, 140, 132, 141]. Several examples overcoming locking in bending dominated problems include [142, 143, 144, 145, 146, 147, 148]. These have been successfully used in many applications and considered to overcome bending problems, despite the fact the formulation is quite complicated and computationally expensive considering numerical implementations in complex problems.

This study however, focuses in modelling the divergence of microstructures from those predicted by the classical theories with all aspects - theoretically, numerically, and experimentally. Hence Kirchhoff-Love plate theory and Euler-Bernoulli beam theory are adopted. Another aim is to fill an important gap in bending problems which are the foundations of a majority of design and analysis issues in MEMS and NEMS industry. This is done by introducing novel plate finite elements, so that geometries that can not be reduced to beam structures can be modelled, and without the need for idealized cases that can be solved with finite element analysis. Recognizing most, if not all, of the MEMS and NEMS structures can be modelled with rectangular plate elements, Kirchhoff-Love rectangular plate elements applicable in that domain are developed, from a single basis function that satisfies the higher order plate equation. Also considering a minority of the relevant MEMS and NEMS structures include triangular regions, Kirchhoff-Love triangular plate elements applicable in that domain are also developed, using the same approach in the basis function satisfying the higher order plate equation.

As far as the experiments in the literature are considered, despite the fact that the size effects have been demonstrated for gold, the experimental data have been shared in the form of force-displacement curves in only one study according to the best of the author's knowledge [1]. Moreover, length scale parameters and size effects for gold, a material of wide-range usage and a great potential, haven't been quantified in literature. Hence in this study, the data of Espinosa et al. along with several bending experiments on gold microstructures using atomic force miscoscopy (AFM) are used to propose length scale parameters for gold materials.

1.2 Proposed Methods and Models

The study stands on three pillars for the solutions of the above mentioned problems. These are theoretical, numerical, and experimental aspects in modelling microstructures. Moreover, all of them introduced a novelty in the respective area as discussed in the forthcoming section.

The theoretical framework of the study is performed by first deriving the weak forms. This is done by using variational methods. Then the set of algebraic equations for the numerical formulation are derived. Computer codes using Octave and Matlab® are developed, in which the finite element equations are solved by Gaussian quadrature. New higher order Kirchhoff-Love plate elements are developed, filling an important gap in literature. To compare higher order and classical theories, the numerical study also includes the use of ANSYS® Mechanical to simulate the experiments. The experimental studies involves bending of gold microstructures. Then using the numerical studies, the length scale parameters for gold are found. This in turn yields the size effect for gold microstructures.

Mathematical models for the microstructures are selected to be Euler-Bernoulli beam theory and Kirchhoff-Love plate theory respectively. That is, microstructures are assumed to be relatively thin so that shear effects are negligible. Most MEMS and NEMS structures used in the modern world today are aligned with this assumption. Although thick beam and thick plate assumptions leading to Timoshenko beam and Mindlin-Reissner plate theories have also been utilized in literature, it is evaluated that Euler-Bernoulli beam and Kirchhoff-Love plate theories are both the most widely used and feasible. The gaps between the structures at which they are subjected to loads and deformations are also much lower, even comparable to the thicknesses of the structures. Hence a fully liner elastic regime is assumed for bending of the gold microstructures.

MSGT and MCST are the main higher order theories utilized. MSGT is a mathematically complete, elegant, proven, and one of the most commonly used theories in higher order elasticity, developed by Lam et al [6], as thoroughly explained in Chapter 2. It is also generally accepted in literature as a theory that compromises between accuracy and computational feasibility, with three length scale parameters. The major part of the study focuses on MSGT, with respect to:

- identifying length scale parameters for gold with respect to Euler-Bernoulli microbeams,
- development of a variational model for Kirchhoff-Love plate finite elements,
- development of rectangular and triangular Kirchhoff-Love plate finite elements,
- development of finite element codes based on the newly developed rectangular and triangular Kirchhoff-Love plate elements,
- identifying length scale parameters for gold with the newly developed Kirchhoff-Love plate elements via literature and bending experiments conducted within.

MCST has advantages in practicality, however lacks the mathematical completeness of MSGT. The single length scale parameter makes it very feasible to use. It is also one of the most widely used methods in microstructure modelling, developed by Yang et al [89], as described in Chapter 2. In this study, it is the secondary higher order theory which is used in:

- identifying length scale parameters for gold with Euler-Bernoulli microbeam modelling,
- comparing with MSGT and the classical theories.

1.3 Contributions and Novelties

Bending experiments on gold microbeams and microplates are performed by an atomic force microscope (AFM). Before performing these experiments, all specimens have been assessed in a clean room for dimensions, gaps, initial deformations, and surface roughness parameters. Using these experiments length scale parameters for gold are identified for the first time in literature. These parameters are based on models and numerical methods based on literature (regarding microbeams), as well as the novel models and methods (regarding microplates). Outcomes of limited experimental data from literature are also compared with the results. The beam and plate assumptions are those of Euler-Bernoulli Beam Theory and Kirchhoff-Love Plate Theory respectively.

A complete higher order mathematical model based on variational formulation for Kirchhoff-Love plates are developed based on MSGT. It paves the way for numerical analysis mentioned below.

Several rectangular and triangular higher order Kirchhoff-Love plate finite elements are newly developed for the Modified Strain Gradient Theory. Rectangular elements can be considered as extensions of Adini-Clough-Melosh (ACM) elements [149, 150] and Bogner–Fox–Schmit (BFS) elements [151]. There are four types with 20, 24, 28, and 32 degree of freedoms (DOF's) - corresponding to 5, 6, 7, and 8 DOF's per node. Triangular elements are based on 18 DOF elements with 6 DOF's per node as in

Bell element [135], complementary to 24-DOF rectangular elements. Finite element codes and routines are developed making use of these elements, that is able to model microstructures with both rectangular and triangular finite element meshes. This is also a first in literature, providing means to analyze MEMS and NEMS structures that can not be modelled by beam elements by MSGT.

Real MEMS structures are analyzed with the newly developed higher order rectangular plate elements in MSGT. The necessity of using higher order theories is also demonstrated for these cases, as well as the need for using plate models, again as a novel aspect.

1.4 Thesis Outline

After the brief introduction in Chapter 1, Chapter 2 focuses on higher order continuum mechanics and specifically strain gradient theories, with comparisons, physical and numerical relations to classical theory. Chapter 3 introduces finite element implementation and newly developed rectangular and triangular elements. The conformity, continuity, applicability and patch tests of the proposed elements, as well as the models for the experiments conducted within the scope of this study are discussed in Chapter 4. The experiments conducted with the use of AFM are discussed in Chapter 5. Chapter 6 includes conclusions, recommendations, and several aspects that need to be emphasized or addressed.

CHAPTER 2

FUNDAMENTALS OF HIGHER ORDER CONTINUUM MECHANICS AND STRAIN GRADIENT THEORIES

The foundation of this study, i.e. theoretical framework of higher order elasticity, is laid in this chapter. Implementation to Euler-Bernoulli beam and Kirchhoff-Love plate formulations are performed based on higher order theories. This framework is then utilized in forthcoming sections to be developed numerically and experimentally.

2.1 Variational Formulation of Classical Elasticity

The formulation of finite elasticity for any structure depends on a potential functional in the form

$$\Pi(\boldsymbol{u}) := \Pi^{int}(\boldsymbol{u}) - \Pi^{ext}(\boldsymbol{u})\,. \tag{2.1}$$

Herein, Π^{int} and Π^{ext} are the energy stored in the body and the work associated with external forces respectively, with $\boldsymbol{u}$ as the displacement field. The internal and external potentials are expressed as

$$\Pi^{int}(\boldsymbol{u}) := \int_{\mathcal{B}} \psi(\boldsymbol{\varepsilon}) d\mathcal{V}, \qquad \text{and} \qquad \Pi^{ext}(\boldsymbol{u}) := \int_{\mathcal{B}} \boldsymbol{u}\cdot\rho_0 \boldsymbol{b} d\mathcal{V} + \int_{\partial\mathcal{B}} \boldsymbol{u}\cdot\boldsymbol{t} d\mathcal{A}\,. \tag{2.2}$$

where ρ_0, $\boldsymbol{b}$, $\boldsymbol{t}$ denote density, prescribed body force tensor, and surface traction tensor, respectively. $\mathcal{B}$ refers to any 3D Riemannian manifold in an Eucledian space consisting of material points within. $\boldsymbol{\varepsilon}$ denotes the strain tensor defined as

$$\boldsymbol{\varepsilon} = \frac{1}{2}(\nabla\boldsymbol{u} + \nabla^T\boldsymbol{u})\,. \tag{2.3}$$

The free energy function for the linear isotropic solid is

$$\psi(\boldsymbol{\varepsilon}) = \frac{1}{2}\lambda(\text{tr}\,\boldsymbol{\varepsilon})^2 + \mu\boldsymbol{\varepsilon} : \boldsymbol{\varepsilon}\,, \tag{2.4}$$

where

$$\lambda = \frac{E\nu}{(1-2\nu)(1+\nu)} \quad \text{and} \quad \mu = \frac{E}{2(1+\nu)} \tag{2.5}$$

are the the first Lamé constant and the shear modulus, respectively, whereas E is the isotropic elastic modulus and ν is the Poisson's ratio.

The boundary value problem for the static equilibrium of an isotropic linear elastic solid is governed by the principle of minimum potential energy

$$\boldsymbol{u} = \arg\left\{ \inf_{\boldsymbol{u}\in\mathcal{B}} \Pi(\boldsymbol{u}) \right\} . \tag{2.6}$$

The principle of minimum potential energy requires the variation of the total potential vanish at equilibrium. From (2.1),

$$\delta\Pi = \delta\Pi^{int} - \delta\Pi^{ext} = 0 . \tag{2.7}$$

The Euler-Lagrange equation resulting from the variational formulation is the balance of linear momentum

$$\text{div}\boldsymbol{\sigma} + \rho_0 \boldsymbol{b} = 0 . \tag{2.8}$$

subjected to the following Dirichlet and Neumann-type boundaries

$$\begin{aligned} &1. \qquad \boldsymbol{u} = \bar{\boldsymbol{u}} \quad \text{on} \quad \partial\mathcal{B}_u , \\ &2. \quad \boldsymbol{\sigma}\cdot\boldsymbol{n} = \bar{\boldsymbol{t}} \quad \text{on} \quad \partial\mathcal{B}_t , \end{aligned} \tag{2.9}$$

see Figures 2.1 and 2.2 for beam and plate geometries and corresponding Riemannian manifolds $\mathcal{B}$. Therein $\partial\mathcal{B}_u$ and $\partial\mathcal{B}_t$ may refer to the physically identical surfaces or points, however they are always considered discrete based on the type of boundary conditions, i.e. Dirichlet or Neumann.

The stress tensor for linear isotropic solid can then be derived from the free energy (2.4).

$$\boldsymbol{\sigma} := \partial_{\boldsymbol{\varepsilon}}\psi(\boldsymbol{\varepsilon}) = \lambda \,\text{tr}\, \boldsymbol{\varepsilon}\, \mathbf{1} + 2\mu\boldsymbol{\varepsilon} . \tag{2.10}$$

2.2 Variational Formulation of Strain Gradient Elasticity

Strain gradient elasticity is implemented by the addition of higher order strains into the free energy function in the sense of Mindlin [62]

$$\psi = f(\boldsymbol{\varepsilon}, \boldsymbol{\eta}) \qquad \text{where} \qquad \boldsymbol{\eta} = \nabla\nabla\boldsymbol{u} \tag{2.11}$$

is the second gradient of the displacement field, and hence the higher order strain tensor, or the strain gradient tensor. For isotropic materials, the following specific form is adopted [86, 83] to additively incorporate the higher order strains into the free energy function

$$\psi(\boldsymbol{\varepsilon}, \boldsymbol{\eta}) = \psi_{\mathrm{C}}(\boldsymbol{\varepsilon}) + \psi_{\mathrm{H}}(\boldsymbol{\eta}) \qquad \text{where} \qquad \psi_{\mathrm{C}}(\boldsymbol{\varepsilon}) = \frac{1}{2}\lambda\,(\mathrm{tr}\,\boldsymbol{\varepsilon})^2 + \mu\boldsymbol{\varepsilon} : \boldsymbol{\varepsilon} \tag{2.12}$$

is the same formulation given in Equation 2.4 representing the classical part of the free energy function and

$$\begin{aligned} \psi_{\mathrm{H}}(\boldsymbol{\eta}) &= a_1\,(\boldsymbol{\eta} : \mathbf{1}) \cdot (\boldsymbol{\eta} : \mathbf{1}) + a_2\,(\mathbf{1} : \boldsymbol{\eta}) \cdot (\boldsymbol{\eta} : \mathbf{1}) + a_3\,(\mathbf{1} : \boldsymbol{\eta}) \cdot (\mathbf{1} : \boldsymbol{\eta}) \\ &\quad + a_4\,(\boldsymbol{\eta} \,\vdots\, \boldsymbol{\eta}) + a_5(\boldsymbol{\eta} \,\vdots\, \overset{13}{\boldsymbol{\eta}^{T}}) \end{aligned} \tag{2.13}$$

is the higher order part of the free energy function. Herein, ($:$) and ($\vdots$) represent the double dot product and the triple dot product respectively as given in Appendix A. $\overset{13}{\boldsymbol{\eta}^{T}}$ refers to the third order transpose operator of $\boldsymbol{\eta}$ as also given there. The terms with five additional material parameters a_i in Equation 2.13 represent the most general case for the higher order part of the free energy function.

From $(2.12)_1$, the first variation of the free energy can be derived as

$$\delta\psi = \boldsymbol{\sigma} : \delta\boldsymbol{\varepsilon} + \boldsymbol{\tau} \,\vdots\, \delta\boldsymbol{\eta} \qquad \text{where} \qquad \boldsymbol{\sigma} := \partial_{\boldsymbol{\varepsilon}}\psi_{\mathrm{C}}(\boldsymbol{\varepsilon}) \quad \text{and} \quad \boldsymbol{\tau} := \partial_{\boldsymbol{\eta}}\psi_{\mathrm{H}}(\boldsymbol{\eta}) \tag{2.14}$$

are the second and third order stress tensors, respectively. Here, the stress tensors $\boldsymbol{\sigma}$ and $\boldsymbol{\tau}$ are the work conjugates of the second order strain $\boldsymbol{\varepsilon}$ and the third order strain $\boldsymbol{\eta}$. The strain gradient tensor $\boldsymbol{\eta}$ can be represented as the summation of its symmetric and antisymmetric in the sense of Fleck [86]

$$\boldsymbol{\eta} = \boldsymbol{\eta}^s + \boldsymbol{\eta}^a\,. \tag{2.15}$$

The symmetric part can be additively decomposed into volumetric $\boldsymbol{\eta}^0$ and deviatoric $\boldsymbol{\eta}^{\mathbf{1}}$ parts so that

$$\boldsymbol{\eta} = \boldsymbol{\eta}^{\mathbf{0}} + \boldsymbol{\eta}^{\mathbf{1}} + \boldsymbol{\eta}^{a}\,, \tag{2.16}$$

leading the way to develop MSGT and MCST as introduced in the forthcoming sections.

2.2.1 Modified Strain Gradient Theory (MSGT)

After several manipulations, Lam et al. [6] used another set of strain and stress metrics to develop the modified version of the ansatz (2.11,2.14)

$$\psi = \tilde{\psi}(\boldsymbol{\varepsilon}, \nabla\varepsilon, \boldsymbol{\eta}^{\mathbf{1}}, \boldsymbol{\chi}) \quad \text{leading to} \quad \delta\psi = \boldsymbol{\sigma}{:}\delta\boldsymbol{\varepsilon} + \boldsymbol{p}{\cdot}\delta\nabla\varepsilon + \boldsymbol{\tau}^{\mathbf{1}}{:}\delta\boldsymbol{\eta}^{\mathbf{1}} + \boldsymbol{m}{:}\delta\boldsymbol{\chi}\,, \tag{2.17}$$

which leads to *Modified Strain Gradient Theory* (MSGT) in the sense of Lam et al. [6].

The stress tensors

$$\begin{gathered} \boldsymbol{\sigma} := \partial_{\boldsymbol{\varepsilon}}\psi_{\mathrm{C}}(\boldsymbol{\varepsilon})\,,\ \boldsymbol{p} := \partial_{\nabla\varepsilon}\psi_{\mathrm{H}}(\boldsymbol{\eta}^{\mathbf{1}}, \nabla\varepsilon, \boldsymbol{\chi})\,,\ \ \boldsymbol{\tau}^{\mathbf{1}} := \partial_{\boldsymbol{\eta}^{\mathbf{1}}}\psi_{\mathrm{H}}(\boldsymbol{\eta}^{\mathbf{1}}, \nabla\varepsilon, \boldsymbol{\chi})\,, \\ \text{and}\ \ \boldsymbol{m} := \partial_{\boldsymbol{\chi}}\psi_{\mathrm{H}}(\boldsymbol{\eta}^{\mathbf{1}}, \nabla\varepsilon, \boldsymbol{\chi}) \end{gathered} \tag{2.18}$$

are the work conjugates of the strain tensors $\boldsymbol{\varepsilon}$, $\nabla\varepsilon$, $\boldsymbol{\eta}^{\mathbf{1}}$, $\boldsymbol{\chi}$ respectively. Herein,

$$\begin{aligned} \boldsymbol{\eta}^{\mathbf{1}} &:= \frac{1}{3}\nabla^{p}\boldsymbol{\varepsilon} - \frac{1}{15}\left(\mathbf{1}\otimes\nabla\varepsilon\right) \\ &- \frac{1}{15}\left[2\left(\mathbf{1}\otimes\ \mathrm{tr}(\nabla\boldsymbol{\varepsilon})\right) + \left(\mathbf{1}\otimes\nabla\varepsilon\right)^{\overset{13}{T}} + 2\left(\mathbf{1}\otimes\mathrm{tr}(\nabla\boldsymbol{\varepsilon})\right)^{\overset{13}{T}}\right] \\ &+ \frac{1}{15}\left[\left(\mathbf{1}\otimes\nabla\varepsilon\right)^{\overset{23}{T}} + 2\left(\mathbf{1}\otimes\mathrm{tr}(\nabla\boldsymbol{\varepsilon})\right)^{\overset{23}{T}}\right]\,,\quad \text{and} \\ \boldsymbol{\chi} &:= \frac{1}{2}\left[\nabla\boldsymbol{\theta} + \nabla^{T}\boldsymbol{\theta}\right] \quad \text{where} \quad \boldsymbol{\theta} := \frac{1}{2}\mathrm{curl}\ \boldsymbol{u}\,. \end{aligned} \tag{2.19}$$

$\boldsymbol{p}$, $\boldsymbol{\tau}^{\mathbf{1}}$, $\boldsymbol{m}$ are the pressure gradient vector, the double stress tensor and the couple stress tensor, respectively. ∇^{p} is the permutational gradient defined as $\nabla^{p}\boldsymbol{\varepsilon} = \varepsilon_{jk,i} + \varepsilon_{ki,j} + \varepsilon_{ij,k}$. $\otimes$ refers to the dyadic product, see Appendix A. The higher order strain metrics are the deviatoric strain or namely stretch gradient tensor $\boldsymbol{\eta}^{\mathbf{1}}$ in addition to the rotation gradient tensor or curvature tensor $\boldsymbol{\chi}$, and the dilatation gradient vector $\nabla\varepsilon$.

The total internal energy for MSGT then takes the following form

$$\Pi^{int}(\boldsymbol{u}) := \int_{\mathcal{B}} \tilde{\psi}(\boldsymbol{\varepsilon}, \nabla\varepsilon, \boldsymbol{\eta}^{\mathbf{1}}, \boldsymbol{\chi})\ d\mathcal{V}\,. \tag{2.20}$$

Also,

$$\psi_{\mathrm{H}} = \tilde{\psi}(\nabla\varepsilon, \boldsymbol{\chi}) = \mu l_0^2 \nabla\varepsilon\cdot\nabla\epsilon + \mu l_1^2\ \boldsymbol{\eta}^{\mathbf{1}} \mathbin{\vdots} \boldsymbol{\eta}^{\mathbf{1}} + \mu l_2^2\ \boldsymbol{\chi} : \boldsymbol{\chi}\,. \tag{2.21}$$

Incorporation of the internal potential (2.20) and the external work potential $(2.2)_2$ into the total potential expression (2.1), the Euler-Lagrange equations of the minimization principle (2.6) reads

$$\operatorname{div}\boldsymbol{\sigma} + \nabla[\operatorname{div}\boldsymbol{p}] + \operatorname{div}[\operatorname{div}\boldsymbol{\tau}] + \frac{1}{2}\operatorname{curl}[\operatorname{div}\boldsymbol{m}] + \rho_0 \boldsymbol{b} = 0\,. \tag{2.22}$$

The corresponding stress measures as work conjugates of the strain measures $\boldsymbol{\varepsilon}$, $\boldsymbol{\eta^1}$, $\nabla\varepsilon$ and $\boldsymbol{\chi}$ respectively are

$$\boldsymbol{\sigma} = \lambda\,(\operatorname{tr}\boldsymbol{\varepsilon})\,\boldsymbol{1} + 2\mu\boldsymbol{\varepsilon}\,, \quad \boldsymbol{p} = 2\mu l_0^2\,\nabla\varepsilon\,, \quad \boldsymbol{\tau} = 2\mu l_1^2\,\boldsymbol{\eta^1} \quad \text{and} \quad \boldsymbol{m} = 2\mu l_2^2\,\boldsymbol{\chi}\,, \tag{2.23}$$

where l_0, l_1, l_2 are the three length scale parameters introduced to capture the size effects in MSGT.

2.2.2 Modified Couple Stress Theory (MCST)

Further simplification of MSGT by disregarding the effects of the strains resulting from the stretch gradient $\boldsymbol{\eta^1}$ and the dilatation gradient $\nabla\varepsilon$ leads to *Modified Couple Stress Theory* (MCST) in the sense of Yang et al. [89]. To do this, taking $l_0 = 0, l_1 = 0$ leads to the Euler-Lagrange equations. There is only one length scale parameter $l_2 = l$.

$$\operatorname{div}\boldsymbol{\sigma} + \frac{1}{2}\operatorname{curl}[\operatorname{div}\boldsymbol{m}] + \rho_0\boldsymbol{b} = 0\,, \quad \text{where} \quad \boldsymbol{\sigma} = \lambda\,(\operatorname{tr}\boldsymbol{\varepsilon})\,\boldsymbol{1} + 2\mu\boldsymbol{\varepsilon} \quad \text{and} \quad \boldsymbol{m} = 2\mu l_2^2\,\boldsymbol{\chi}\,. \tag{2.24}$$

The length scale effect is incorporated through single length scale parameter l_2 appearing in the definition of the couple stress tensor $\boldsymbol{m}$.

2.3 Implementation to Euler-Bernoulli Beams

A brief introduction of classical Euler-Bernoulli beams is given in Section 2.3.1, followed by the implementation of MSGT and MCST in Sections 2.3.2 and 2.3.3.

2.3.1 Euler-Bernoulli Beams in Classical Theory

Euler-Bernoulli beam is based on the kinematic assumptions [152] that all rotations are small and plane sections remain plane and perpendicular to the neutral axis during rotation. The displacement field according to Figure 2.1(a) is

$$u_x(x) = -z\frac{\partial w}{\partial x}, \; u_z(x) = w\,, \tag{2.25}$$

and w=$w(x)$. The rotation and curvature can be represented as

$$\theta = \frac{dw}{dx} \quad \text{and} \quad \kappa = \frac{d^2w}{dx^2}\,, \qquad M = EI\kappa\,. \tag{2.26}$$

where I is the area moment of inertia of the beam cross section and the beam geometry is as given in Figure 2.1(a). Accordingly, rotations are assumed to be small and plane sections are assumed to remain plane and perpendicular to neutral axis. The displacement vector $\boldsymbol{u}$ consists of vertical displacements w and rotations θ. Surface traction vector $\boldsymbol{t}$ also consists of shear forces V and moments M.

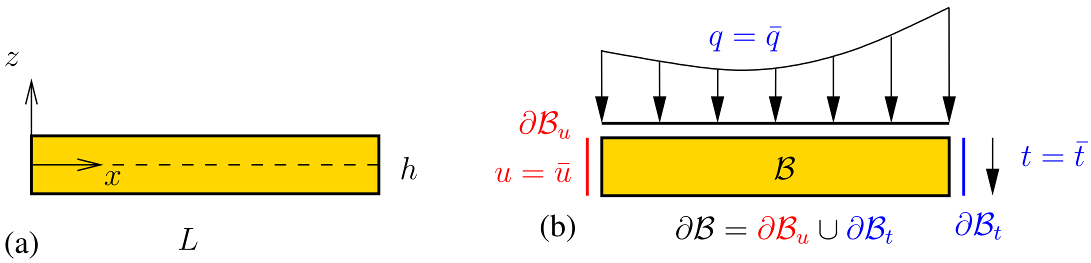

Figure 2.1: (a) Kirchhoff-Love plate geometry and (b) Dirichlet $\partial\mathcal{B}_u$ and Neumann $\partial\mathcal{B}_t$ boundary conditions imposed. Note that $\partial\mathcal{B} = \partial\mathcal{B}_u \cup \partial\mathcal{B}_t$.

Due to kinematic equations, shearing, torsional, longitudinal effects are neglected. Hence strain energy is governed solely by bending action. Incorporation of $(2.26)_1$ and $(2.26)_2$ into (2.2) leads to the internal potential

$$\mathit{\Pi}^{int} = \frac{1}{2}\int_L M\kappa dx = \frac{1}{2}\int_0^L \left[EI\left(\frac{d^2w}{dx^2}\right)^2\right] dx \tag{2.27}$$

for an Euler-Bernoulli beam having a length L in x direction. The external potential has the following form

$$\mathit{\Pi}^{ext} = \int_L \bar{q}wdx + \sum_{\partial\mathcal{B}_t}[Vw]\Big|_{\partial\mathcal{B}_t} + \sum_{\partial\mathcal{B}_t}[M\theta]\Big|_{\partial\mathcal{B}_t}\,. \tag{2.28}$$

As the first variation of the total potential Π has to vanish at the equilibrium state. Incorporation of (2.27) and (2.28) into (2.7) yields

$$\delta\mathit{\Pi} = \int_0^L [\delta\kappa\; EI\; \kappa]\, dx - \int_L q\,\delta w dx - \sum_{\partial\mathcal{B}_t}[V\delta w]\Big|_{\partial\mathcal{B}_t} - \sum_{\partial\mathcal{B}_t}[M\delta\theta]\Big|_{\partial\mathcal{B}_t} = 0\,. \tag{2.29}$$

Use of integration by parts twice leads to

$$\begin{aligned}\delta\Pi = \int\limits_0^L \left(EI\frac{d^4w(x)}{dx^4} - q(x)\right)\delta w dx + \left(-EI\frac{d^3w(x)}{dx^3} - V(x)\right)\delta w\Big|_0^L \\ + \left(-EI\frac{d^2w(x)}{dx^2} - M(x)\right)\delta\theta\Big|_0^L = 0\,.\end{aligned} \tag{2.30}$$

The Euler-Lagrange equation of the minimization principle (2.1) can then be derived as given in e.g. [153]

$$EI\frac{d^4w(x)}{dx^4} - q(x) = 0\,, \tag{2.31}$$

along with the relations

$$V(x) = -EI\frac{d^3w(x)}{dx^3} \qquad \text{and} \qquad M(x) = EI\frac{d^2w(x)}{dx^2} \tag{2.32}$$

for shear force V and bending moment M.

2.3.2 Euler-Bernoulli Beams in Modified Strain Gradient Theory

Making use of the strain expressions (2.19) and the stress expressions (2.23) together with the kinematic assumptions associated with the Euler-Bernoulli beam theory, the following strain energy equation can be found

$$\Pi^{int} = \frac{1}{2}\int_0^L c_1\left(\frac{d^2w}{dx^2}\right)^2 dx + \frac{1}{2}\int_0^L c_2\left(\frac{d^3w}{dx^3}\right)^2 dx \tag{2.33}$$

where

$$c_1 = E^*I + \mu bh\left(2l_0^2 + \frac{8}{15}l_1^2 + l_2^2\right) \qquad \text{and} \qquad c_2 = \mu I\left(2l_0^2 + \frac{4}{5}l_1^2\right)\,, \tag{2.34}$$

where E^* is given as [154]

$$E^* = \frac{E(1-\nu)}{(1-2\nu)(1+\nu)}\,. \tag{2.35}$$

Note that various authors take different values for E^* with an additional simplification of disregarding ν at various points of derivation of equation (2.35). Kahrobaiyan et al. [92] take $E^* = E$ for general case and Zhao et al. [96] take it to be $E^* = E/2(1+\nu)$ for plane strain case. There are also different opinions of the requirement of Poisson's ratio in the relevant formulation. Ma et al. [106] argue that it is necessary, whereas Dehrouyeh-Semnani and Nikkhah-Bahrami [155] argue vice versa. In this study, (2.35) is considered to be valid.

The external potential for the MSGT based beam theory takes the following form

$$\Pi^{ext} = \int_0^L q(x) w dx + [V(x)w]\Big|_0^L + \left[M(x)\frac{dw}{dx}\right]\Big|_0^L + \left[Q(x)\frac{d^2w}{dx^2}\right]\Big|_0^L . \quad (2.36)$$

Here, $Q(x)$ is the higher order moment conjugate to the curvature κ. The first variation of the internal potential leads to

$$\delta\Pi^{int} = \int_0^L \delta\frac{d^2w}{dx^2}\, c_1\, \frac{d^2w}{dx^2}\, dx + \int_0^L \delta\frac{d^3w}{dx^3}\, c_2\, \frac{d^3w}{dx^3} dx\,. \quad (2.37)$$

Making use of integration by parts twice for the first term on the right hand side of the equality (2.37) and three times for the second term leads to

$$\begin{aligned}\delta\Pi^{int} = &\int_0^L \left(c_1\frac{d^4w}{dx^4} - c_2\frac{d^6w}{dx^6}\right)\delta w dx + \left(-c_1\frac{d^3w}{dx^3} + c_2\frac{d^5w}{dx^5}\right)\delta w\Big|_0^L \\ &+ \left(c_1\frac{d^2w}{dx^2} - c_2\frac{d^4w}{dx^4}\right)\delta\theta\Big|_0^L + c_2\frac{d^3w}{dx^3}\delta\kappa\Big|_0^L .\end{aligned} \quad (2.38)$$

Similarly, the first variation of the external work potential can be derived as

$$\delta\Pi^{ext} = \int_0^L q(x)\delta w dx + [V(x)\delta w]\Big|_0^L + [M(x)\delta\theta]\Big|_0^L + [Q(x)\delta\kappa]\Big|_0^L . \quad (2.39)$$

Inserting (2.38) and (2.39) into (2.7):

$$\begin{aligned}\delta\Pi = &\int_0^L \left[c_1\frac{d^4w}{dx^4} - c_2\frac{d^6w}{dx^6} - q(x)\right]\delta w dx + \left[-c_1\frac{d^3w}{dx^3} + c_2\frac{d^5w}{dx^5} - V(x)\right]\delta w\Big|_0^L \\ &+ \left[c_1\frac{d^2w}{dx^2} + c_2\frac{d^4w}{dx^4} - M(x)\right]\delta\theta\Big|_0^L + \left[c_2\frac{d^3w}{dx^3} - Q(x)\right]\delta\kappa\Big|_0^L = 0\end{aligned} \quad (2.40)$$

The Euler-Lagrange equation of the minimization principle based on the MSGT takes the following form

$$c_1\frac{d^4w}{dx^4} - c_2\frac{d^6w}{dx^6} - q(x) = 0\,, \quad (2.41)$$

along with the relations for shear force $V(x)$, bending moment $M(x)$ and higher order moment $Q(x)$

$$V(x) = -c_1\frac{dw^3}{dx^3} + c_2\frac{dw^5}{dx^5}\,,\ M(x) = c_1\frac{dw^2}{dx^2} - c_2\frac{dw^4}{dx^4}\,,\ \text{and } Q(x) = c_2\frac{dw^3}{dx^3}\,. \quad (2.42)$$

Therein (2.41) represents the primary difference in MSGT and classical theory, and MCST in that regard, as will seen in the next section: The beam equation in MSGT is of sixth order, whereas it is of fourth order in classical theory (2.31). The force and moment equations are similarly of two orders more than those in classical theory, with an introduction of a higher order moment term Q.

2.3.3 Euler-Bernoulli Beams in Modified Couple Stress Theory

The strain energy formulation, the starting point in all relevant theories, is independent of dilatation gradient vector $\nabla\,\varepsilon$ and deviatoric stretch gradient tensor $\boldsymbol{\eta}^1$, but dependent on only conventional strain tensor $\boldsymbol{\varepsilon}$ and rotation gradient tensor $\boldsymbol{\chi}$

$$\Pi^{int} = \frac{1}{2}\int_{\mathcal{B}} (\boldsymbol{\sigma} : \boldsymbol{\varepsilon} + \boldsymbol{m}\cdot\boldsymbol{\chi})\, dV. \tag{2.43}$$

With one length scale parameter l_2 as given previously and with $l_0 = l_1 = 0$, the total internal energy becomes

$$\Pi^{int} = \int_0^L \left(E^*I + \mu bhl_2^2\right)\left(\frac{d^2w}{dx^2}\right)^2 dx\,. \tag{2.44}$$

The Euler-Lagrange equation of the minimization principle based on the MCST takes the following form

$$c_1\frac{d^4w}{dx^4} - q(x) = 0\,, \tag{2.45}$$

along with relevant relations given in (2.42) with $c_2 = 0$. The order of the beam, force and moment equations are hence the same as those of the classical theory.

Note that internal potential (2.44) has a similar structure with the classical Euler-Bernoulli beam theory. By replacing $EI \rightarrow c_1$ where $c_1 = E^*I + \mu bhl_2^2$ in the aforementioned variational formulation through equations (2.27-2.32), classical formulation turns into MCST formulation.

2.4 Implementation to Kirchhoff-Love Plates

A majority, if not most of MEMS and NEMS structures can not be modelled by beam theories. Plate theories are required in order to sufficiently design and analyze those.

And since in many MEMS and NEMS structures, thickness is considerably less than the largest dimension (length) of the plate ($t < 0.1L$), Kirchhoff-Love plate theory is adopted in the scope of this study.

A brief introduction of classical Kirchhoff-Love plates is given in Section 2.4.1 below. It is followed by Sections 2.4.2 and 2.4.3 in which the implementation of MSGT and MCST are discussed.

2.4.1 Kirchhoff-Love Plates in Classical Theory

The Kirchhoff-Love plate theory is the extension of Euler-Bernoulli beam theory in 2D. Generally all the formulations presented herewith can be achieved from those in Section 2.3 by including the omitted dimension in y. Accordingly, rotations are assumed to be small and plane sections are assumed to remain plane and perpendicular to neutral axis, based on the displacement field

$$u_x(x,y,z) = -z\frac{\partial w}{\partial x},\ u_y(x,y,z) = -z\frac{\partial w}{\partial y},\ u_z(x,y) = w\,, \tag{2.46}$$

where the plate axes and geometry are as defined as in Figure 2.2(a) and w=$w(x,y)$. Therein L is the length, W is the width, and h is the thickness of the plate. The out-of-plane rotations and the curvatures can be described as

$$\theta_x = \frac{\partial w}{\partial x}, \quad \theta_y = \frac{\partial w}{\partial y}, \quad \kappa_{xx} = \frac{\partial^2 w}{\partial x^2},\ \kappa_{yy} = \frac{\partial^2 w}{\partial y^2}, \quad \text{and} \quad \kappa_{xy} = 2\frac{\partial^2 w}{\partial x \partial y}\,. \tag{2.47}$$

The small-strain linear isotropic material response leads to the constitutive relation between the moment and the curvature

$$\boldsymbol{M} := \boldsymbol{E}\,\boldsymbol{\kappa} \quad \text{where} \quad \begin{bmatrix} M_{xx} \\ M_{yy} \\ M_{xy} \end{bmatrix} = D \begin{bmatrix} 1 & \nu & 0 \\ \nu & 1 & 0 \\ 0 & 0 & \frac{1}{2}(1+\nu) \end{bmatrix} \begin{bmatrix} \kappa_{xx} \\ \kappa_{yy} \\ \kappa_{xy} \end{bmatrix}. \tag{2.48}$$

Herein, ν is the Poisson's ratio, and $D = Eh^3/12(1-\nu^2)$ is the isotropic plate rigidity. The displacement vector $\boldsymbol{u}$ consists of vertical displacements w and rotations θ and surface traction vector $\boldsymbol{t}$ consists of shear forces V and moments M as given in Figure 2.2(b).

Again, due to kinematic equations, shearing, torsional, longitudinal effects are neglected. Therefore strain energy is governed by bending action solely.

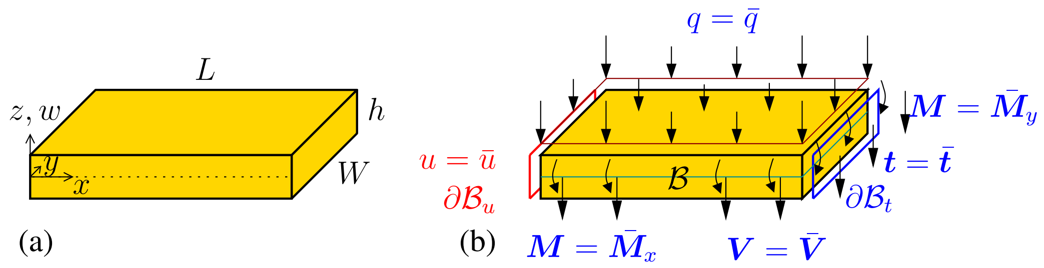

Figure 2.2: (a) Kirchhoff-Love plate geometry and (b) Dirichlet $\partial\mathcal{B}_u$ and Neumann $\partial\mathcal{B}_t$ boundary conditions imposed. Note that $\partial\mathcal{B} = \partial\mathcal{B}_u \cup \partial\mathcal{B}_t$.

For a Kirchhoff-Love plate, incorporation of (2.47) and (2.48) into (2.2) leads to the internal and the external potential

$$\Pi^{int} = \frac{1}{2}\int_{\mathcal{B}} (\boldsymbol{M} : \boldsymbol{\kappa})\, dA \text{ and } \Pi^{ext} = \int_{\mathcal{B}} \bar{q}\bar{w}\, dA + \int_{\partial\mathcal{B}_t} \bar{V}\bar{w}\, ds + \int_{\partial\mathcal{B}_t} \bar{M}\bar{\theta}\, ds\,. \quad (2.49)$$

Herein,

$$\bar{M} = \begin{bmatrix} \bar{M}_x \\ \bar{M}_y \end{bmatrix} \quad \text{and} \quad \bar{\theta} = \begin{bmatrix} \bar{\theta}_x \\ \bar{\theta}_y \end{bmatrix}\,. \quad (2.50)$$

Since the first variation of the total potential Π has to vanish at the equilibrium state, incorporation of $(2.49)_1$ and $(2.49)_2$ into (2.7) yields

$$\begin{aligned} \delta\Pi = &\int_{\mathcal{B}} \left[\delta\kappa_{xx} D(\kappa_{xx} + \nu\kappa_{yy}) + \delta\kappa_{yy} D(\kappa_{yy} + \nu\kappa_{xx}) + \delta\kappa_{xy} D\frac{1}{2}(1-\nu)\kappa_{xy}\right] dA \\ &- \int_{\mathcal{B}} \bar{q}\delta\bar{w}\, dA + \int_{\partial\mathcal{B}_t} \bar{V}\delta\bar{w}\, ds + \int_{\partial\mathcal{B}_t} \bar{M}\delta\bar{\theta}\, ds = 0\,. \end{aligned} \quad (2.51)$$

The Euler-Lagrange equation of the minimization principle (2.1) can be derived as

$$D\left(\frac{\partial^4 w(x,y)}{\partial x^4} + 2\frac{\partial^2 w(x,y)}{\partial x^2 \partial y^2} + \frac{\partial^4 w(x,y)}{\partial y^4}\right) - q(x,y) = 0 \quad \text{or} \quad D\nabla^2\nabla^2(w) - q = 0\,, \quad (2.52)$$

where $\nabla^2\nabla^2(\bullet)$ is the biharmonic operator. The Dirichlet (essential) and Neumann (natural) boundary conditions are respectively,

$$\begin{aligned} &1.\ \ w = \bar{w} \quad \theta_x = \bar{\theta}_x \quad \theta_y = \bar{\theta}_y \quad \text{at} \quad \partial\mathcal{B}_u\,, \\ &2.\ \ V = \bar{V} \quad M_x = \bar{M}_x \quad M_y = \bar{M}_y \quad \text{at} \quad \partial\mathcal{B}_t\,. \end{aligned} \quad (2.53)$$

2.4.2 Kirchhoff-Love Plates in Modified Strain Gradient Theory

With the displacement field given in (2.46) and kinematic relations given in (2.47) valid, an additional set of higher order out-of-plane curvatures are defined as

$$\varrho_{xxx} = \frac{\partial^3 w}{\partial x^3}, \quad \varrho_{xxy} = \frac{\partial^3 w}{\partial x^2 y}, \quad \varrho_{xyy} = \frac{\partial^3 w}{\partial x y^2}, \quad \text{and} \quad \varrho_{yyy} = \frac{\partial^3 w}{\partial x^3}\,. \tag{2.54}$$

The constitutive relations between the *moment & curvature* and *higher order forces & higher order curvatures* are, respectively

$$\boldsymbol{M} := \boldsymbol{E}_C\,\boldsymbol{\kappa}\ : \quad \begin{bmatrix} M_{xx} \\ M_{yy} \\ M_{xy} \end{bmatrix} = \begin{bmatrix} d_1 & d_2 & 0 \\ d_2 & d_1 & 0 \\ 0 & 0 & d_3 \end{bmatrix} \begin{bmatrix} \kappa_{xx} \\ \kappa_{yy} \\ \kappa_{xy} \end{bmatrix} \tag{2.55}$$

and

$$\boldsymbol{Q} := \boldsymbol{E}_H\,\boldsymbol{\varrho}\ : \quad \begin{bmatrix} Q_{xxx} \\ Q_{xxy} \\ Q_{xyy} \\ Q_{yyy} \end{bmatrix} = \begin{bmatrix} d_4 & 0 & d_5 & 0 \\ 0 & d_6 & 0 & d_5 \\ d_5 & 0 & d_6 & 0 \\ 0 & d_5 & 0 & d_4 \end{bmatrix} \begin{bmatrix} \varrho_{xxx} \\ \varrho_{xxy} \\ \varrho_{xyy} \\ \varrho_{yyy} \end{bmatrix} \tag{2.56}$$

where

$$\begin{aligned} d_1 &= D + \mu h\left(2l_0^2 + \frac{8}{15}l_1^2 + l_2^2\right), & d_4 &= \mu h^3\left(\frac{l_0^2}{6} + \frac{l_1^2}{15}\right), \\ d_2 &= D\nu + \mu h\left(2l_0^2 - \frac{2}{15}l_1^2 - l_2^2\right), & d_5 &= \mu h^3\left(\frac{l_0^2}{6} - \frac{l_1^2}{10}\right), \\ d_3 &= 2D(1-\nu) + \mu h\left(\frac{4}{3}l_1^2 + 4l_2^2\right), & d_6 &= \mu h^3\left(\frac{l_0^2}{6} + \frac{l_1^2}{5}\right). \end{aligned} \tag{2.57}$$

Derivation of the above equations along with the relevant stress and strain metrics are given in Appendix B.

For the MSGT based higher order Kirchhoff-Love plate, incorporation of (2.47,2.54) and (2.55) into (2.2) leads to the internal potential

$$\Pi^{int} = \frac{1}{2}\int_{\mathcal{B}} (\boldsymbol{M} : \boldsymbol{\kappa} + \boldsymbol{Q} \,\vdots\, \boldsymbol{\varrho})\, dA\,. \tag{2.58}$$

The external potential reads

$$\Pi^{ext} = \int_{\mathcal{B}} \bar{q}\bar{w}\; dA + \int_{\partial\mathcal{B}_t} \bar{V}\bar{w}\; ds + \int_{\partial\mathcal{B}_t} \bar{M}\bar{\theta}\; ds + \int_{\partial\mathcal{B}_t} \bar{Q}\bar{\kappa}\; ds \tag{2.59}$$

where

$$\bar{Q} = \begin{bmatrix} \bar{Q}_{xxx} \\ \bar{Q}_{yyy} \end{bmatrix} \quad \text{and} \quad \bar{\kappa} = \begin{bmatrix} \bar{\kappa}_{xx} \\ \bar{\kappa}_{yy} \end{bmatrix} . \tag{2.60}$$

Q is therefore the work conjugate of the curvature κ, similar to the work conjugate couples V - w and M - θ. The first variation of the internal potential leads to

$$\begin{aligned} \delta\Pi^{int} = \int_{\mathcal{B}} [&\delta\kappa_{xx}(d_1\kappa_{xx} + d_2\kappa_{yy}) + \delta\kappa_{yy}(d_2\kappa_{xx} + d_1\kappa_{yy}) + \delta\kappa_{xy}d_3\kappa_{xy} \\ &+ \delta\varrho_{xxx}(d_4\varrho_{xxx} - d_5\varrho_{xyy}) + \delta\varrho_{xxy}(d_6\varrho_{xxy} + d_5\varrho_{yyy}) \\ &+ \delta\varrho_{xyy}(d_5\varrho_{xxx} + d_6\varrho_{xyy}) + \delta\varrho_{yyy}(d_5\varrho_{xxy} + d_4\varrho_{yyy})]dA \, . \end{aligned} \tag{2.61}$$

Similarly, the first variation of the external work potential can be derived as

$$\delta\Pi^{ext} = \int_{\mathcal{B}} \bar{q}\delta\bar{w} \; dA + \int_{\partial\mathcal{B}_t} \bar{V}\delta\bar{w} \; ds + \int_{\partial\mathcal{B}_t} \bar{M}\delta\bar{\theta} \; ds + \int_{\partial\mathcal{B}_t} \bar{Q}\delta\bar{\kappa} \; ds \, . \tag{2.62}$$

Incorporation of above equations into (2.7) yields the Euler-Lagrange equation of the minimization principle as

$$d_1\left(\frac{\partial^4 w}{\partial x^4} + 2\frac{\partial^4 w}{\partial x^2 \partial y^2} + \frac{\partial^4 w}{\partial y^4}\right) - d_4\left(\frac{\partial^6 w}{\partial x^6} + 3\frac{\partial^6 w}{\partial x^4 \partial y^2} + 3\frac{\partial^6 w}{\partial x^2 \partial y^4} + \frac{\partial^6 w}{\partial y^6}\right) - q = 0 \, . \tag{2.63}$$

The Dirichlet and Neumann boundary conditions are respectively,

$$\begin{aligned} &1. \;\; w{=}\bar{w} \quad \theta_x{=}\bar{\theta}_x \quad \theta_y{=}\bar{\theta}_y \quad \kappa_x{=}\bar{\kappa}_x \quad \kappa_y{=}\bar{\kappa}_y \quad \text{at} \quad \partial\mathcal{B}_u \, , \\ &2. \;\; V{=}\bar{V} \quad M_x{=}\bar{M}_x \quad M_y{=}\bar{M}_y \quad Q_x{=}\bar{Q}_x \quad Q_y{=}\bar{Q}_y \quad \text{at} \quad \partial\mathcal{B}_t \, . \end{aligned} \tag{2.64}$$

2.4.3 Kirchhoff-Love Plates in Modified Couple Stress Theory

As discussed in Section 2.2.2 the number of the additional length scale parameter is one in MCST. That length scale parameters corresponds to l_2, with $l_0 = l_1 = 0$ in MSGT. The strain energy formulation, the starting point in all relevant theories, is independent of dilatation gradient vector $\nabla\,\varepsilon$ and deviatoric stretch gradient tensor $\boldsymbol{\eta}^{\mathbf{1}}$, but dependent on only conventional strain tensor ε and rotation gradient tensor $\boldsymbol{\chi}$

$$\Pi^{int} = \frac{1}{2}\int_{\mathcal{B}} (\boldsymbol{\sigma} : \boldsymbol{\varepsilon} + \boldsymbol{m} \cdot \boldsymbol{\chi}) \, dV. \tag{2.65}$$

With the workflow given in the section above, the Euler-Lagrange equation of the minimization principle can be written as:

$$\left(D + \mu h l_2^2\right)\left(\frac{\partial^4 w}{\partial x^4} + 2\frac{\partial^4 w}{\partial x^2 \partial y^2} + \frac{\partial^4 w}{\partial y^4}\right) - q = 0\,, \tag{2.66}$$

noting that it is equivalent to (2.63) when $l_0 = l_1 = 0$. It is also equivalent to (2.52) with D replaced by the term $D + \mu h l_2^2$.

CHAPTER 3

HIGHER ORDER FINITE ELEMENTS

Euler-Bernoulli beam and Kirchhoff-Love plate finite elements are discussed within the frameworks of MSGT and MCST in this chapter. The finite element implementation starts with the discussion of classical elements, then proceeds with implementation in MSGT and then MCST.

3.1 Euler-Bernoulli Beam Elements

3.1.1 Classical Euler-Bernoulli Beam Elements

Let us consider a classical Euler-Bernoulli beam element domain $\mathcal{B}_e$ as depicted in given in Figure 2.1(a). Therein, generalized nodal displacements at the element nodes can be prescribed as

$$\begin{aligned} &1. \quad w = w_1 \quad \text{and} \quad \theta = \theta_1 \quad @ \quad x = 0\,, \\ &2. \quad w = w_2 \quad \text{and} \quad \theta = \theta_2 \quad @ \quad x = L\,, \end{aligned} \tag{3.1}$$

see also Figure 3.1(a). Similarly, the generalized nodal force resultants are prescribed as

$$\begin{aligned} &1. \quad V = V_1 \quad \text{and} \quad M = M_1 \quad @ \quad x = 0\,, \\ &2. \quad V = V_2 \quad \text{and} \quad M = M_2 \quad @ \quad x = l\,, \end{aligned} \tag{3.2}$$

see also Figure 3.1(b). Hence, the element nodal displacement vector $\boldsymbol{d}$ and the element nodal force vector $\boldsymbol{f}$ read

$$\boldsymbol{d}^T = [\, w_1 \;\; \theta_1 \;\; w_4 \;\; \theta_2 \,]\,, \qquad \boldsymbol{f}^T = [\, V_1 \;\; M_1 \;\; V_2 \;\; M_2 \,]\,. \tag{3.3}$$

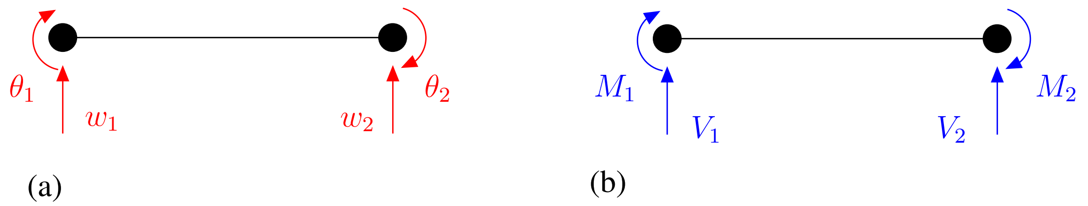

Figure 3.1: (a) Nodal degrees of freedom and (b) corresponding nodal forces for a classical Euler-Bernoulli beam formulation

For discretization of the beam element, the displacement field $w(x)$ within the element domain $\mathcal{B}_e$ is interpolated as

$$w(x) = \boldsymbol{N}\boldsymbol{d} = \sum_{i=1}^{n_{\text{DOF}}} \sum_{j=1}^{n_{\text{nodes}}} N_i^j d_i^j \quad \text{where} \quad \boldsymbol{N} = \left[\, N_1^1 \;\; N_2^1 \;\; N_1^2 \;\; N_2^2 \,\right], \tag{3.4}$$

is the row vector including the set of interpolation/shape functions. $n_{\text{DOF}} = 2$ is the number of degrees of freedom (DOFs) per node and $n_{\text{nodes}} = 2$ is the number of nodes per element, with N_i^j, i denoting the relevant DOF of the node and j denoting the relevant node. The number of DOFs per element is hence 4. This representation is adopted all throughout this study.

The homogenous solution of the ordinary differential equation (2.31) is

$$w(x) = a_1 + a_2 x + a_3 x^2 + a_4 x^3 \tag{3.5}$$

satisfying the C^1 continuity requirement. The interpolation functions are found as Hermite cubic functions as

$$\begin{aligned} N_1^1(x) &= 1 - 3\left(\frac{x}{L}\right)^2 + 2\left(\frac{x}{L}\right)^3, \quad & N_2^1(x) &= x\left(1 - \frac{x}{L}\right)^2, \\ N_1^1(x) &= 3\left(\frac{x}{L}\right)^2 - 2\left(\frac{x}{L}\right)^3, \quad & N_2^2(x) &= \frac{x^3}{L^2} - \frac{x^2}{L}. \end{aligned} \tag{3.6}$$

Then, the displacement w, rotation θ, and the curvature κ fields can be approximated as

$$w(x) = \boldsymbol{N}(x)\boldsymbol{d}, \quad \theta(x) = \frac{dw}{dx} = \frac{d\boldsymbol{N}(x)}{dx}\boldsymbol{d}, \quad \kappa(x) = \frac{d^2 w}{dx^2} = \frac{d^2\boldsymbol{N}(x)}{dx^2}\boldsymbol{d}. \tag{3.7}$$

Consequently, the variation of the displacement w, rotation θ, and the curvature κ fields can be written as

$$\delta w(x) = \boldsymbol{N}(x)\delta\boldsymbol{d}, \quad \delta\theta(x) = \delta\frac{dw}{dx} = \frac{d\boldsymbol{N}(x)}{dx}\delta\boldsymbol{d}, \quad \delta\kappa(x) = \delta\frac{d^2 w}{dx^2} = \frac{d^2\boldsymbol{N}(x)}{dx^2}\delta\boldsymbol{d}. \tag{3.8}$$

Incorporation of the discrete counterpart of the curvature in equation $(3.7)_3$ and its variation $(3.8)_3$ into (2.29)

$$\delta \Pi = \mathop{\mathsf{A}}_{e=1}^{n_{elem}} \delta \boldsymbol{d}_e^T \boldsymbol{k}_e\, \boldsymbol{d}_e - \mathop{\mathsf{A}}_{e=1}^{n_{elem}} \delta \boldsymbol{d}_e^T \boldsymbol{f}_e = 0\,, \tag{3.9}$$

where

$$\boldsymbol{k}_e = \int_0^L \left[\left(\frac{d^2 \boldsymbol{N}(x)}{dx^2} \right)^T EI \left(\frac{d^2 \boldsymbol{N}(x)}{dx^2} \right) \right] dx \quad \text{and} \quad \boldsymbol{f}_e = \int_0^L \boldsymbol{N}^T q(x) dx \tag{3.10}$$

are the element stiffness matrix and the element nodal force vector, respectively, for an element of having length L. Herein, A refers to the standard assembly of element contributions at the local element nodes where n_{elem} denotes the total number of elements.

The global stiffness matrix, generalized nodal displacement vector and the generalized force vector assembled from local force vectors read

$$\boldsymbol{K} = \mathop{\mathsf{A}}_{e=1}^{n_{elem}} \boldsymbol{k}_e\,, \qquad \boldsymbol{D} = \mathop{\mathsf{A}}_{e=1}^{n_{elem}} \boldsymbol{d}_e \qquad \text{and} \quad \boldsymbol{F} = \mathop{\mathsf{A}}_{e=1}^{n_{elem}} \boldsymbol{f}_e\,, \tag{3.11}$$

respectively. No variation exists $\delta \boldsymbol{d} = 0$ at essential boundary $\partial \mathcal{B}_u$ where the displacements are prescribed $\boldsymbol{d} = \bar{\boldsymbol{d}}$. The equilibrium is satisfied for arbitrary variation of the displacement $\delta \boldsymbol{d}$ leading to the set of linear algebraic equations

$$\boldsymbol{K}\boldsymbol{D} = \boldsymbol{F}\,. \tag{3.12}$$

Substituting the shape functions (3.6) into (3.10), the element stiffness matrix for the Euler-Bernoulli beam element is obtained as

$$\boldsymbol{k}_e = \frac{EI}{L^3} \begin{bmatrix} 12 & 6L & -12 & 6L \\ 6L & 4L^2 & -6L & 2L^2 \\ -12 & -6L & 12 & -6L \\ 6L & 2L^2 & -6L & 4L^2 \end{bmatrix}. \tag{3.13}$$

3.1.2 Higher Order Euler-Bernoulli Beam Elements

3.1.2.1 Higher Order Euler-Bernoulli Beam Elements for MSGT

For the Euler-Bernoulli beam based on MSGT, the prescribed nodal displacements are

$$\begin{aligned} &1. \quad w = w_1 \quad \text{and} \quad \theta = \theta_1 \quad \text{and} \quad \kappa = \kappa_1 \quad @ \quad x = 0\,, \\ &2. \quad w = w_2 \quad \text{and} \quad \theta = \theta_2 \quad \text{and} \quad \kappa = \kappa_2 \quad @ \quad x = L\,. \end{aligned} \tag{3.14}$$

and the nodal force resultants are

$$\begin{aligned} &1. \quad M \;=\; M_1 \quad \text{and} \quad V \;=\; V_1 \quad \text{and} \quad Q \;=\; Q_1 \quad @ \quad x = 0\,, \\ &2. \quad M \;=\; M_2 \quad \text{and} \quad V \;=\; V_2 \quad \text{and} \quad Q \;=\; Q_2 \quad @ \quad x = L\,. \end{aligned} \tag{3.15}$$

as given in Figure 2.1(a) and (b) respectively.

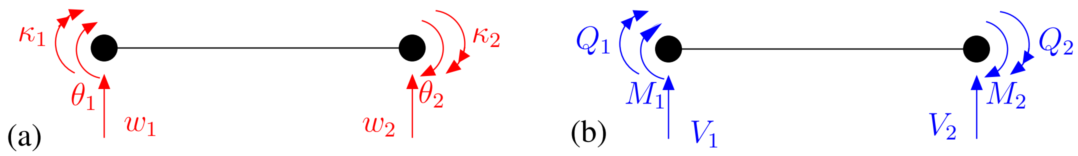

Figure 3.2: (a) Nodal degrees of freedom and (b) corresponding nodal forces for a higher order Euler-Bernoulli beam formulation based on MSGT.

The element nodal displacement vector $\boldsymbol{d}$ and the element nodal force vector f read

$$\boldsymbol{d}^T = [\, w_1 \;\; \theta_1 \;\; \kappa_1 \;\; w_2 \;\; \theta_2 \;\; \kappa_2 \,]\,, \qquad \boldsymbol{f}^T = [\, V_1 \;\; M_1 \;\; Q_1 \;\; V_2 \;\; M_2 \;\; Q_2 \,]\,. \tag{3.16}$$

For discretization of the beam element, displacement function within $\mathcal{B}_e$ is interpolated as

$$w(x) = \boldsymbol{N}\boldsymbol{d} = \sum_{i=1}^{n_{\text{DOF}}} \sum_{j=1}^{n_{\text{nodes}}} N_i^j d_i^j \quad \text{where} \quad \boldsymbol{N} = [\, N_1^1 \;\; N_2^1 \;\; N_1^2 \;\; N_2^2 \,]\,, \tag{3.17}$$

where $n_{\text{DOF}} = 3$ is the number of degrees of freedom (DOFs) per node, with the number of DOFs per element as 6.

The homogenous solution of the ordinary differential equation (2.22) is

$$w(x) = a_1 + a_2 x + a_3 x^2 + a_4 x^3 + a_5 \text{sinh}(\sqrt{\frac{c_1}{c_2}} x) + a_6 \text{cosh}(\sqrt{\frac{c_1}{c_2}} x) \tag{3.18}$$

The solution satisfies C^2 continuity. and are given in Appendix C. These shape functions are verified per those given in the study of Kahrobaiyan et al [92] and are drawn in Figure 3.3(a). The shape functions are symmetric with their nodal counterparts (i.e. N_1^1 with N_1^2, N_2^1 with N_2^2, N_3^1 with N_3^2) as in the classical case, therefore only the first three shape functions are shown in Figure 3.3(b)-(d). Different from those of the classical theory, the shape functions of MSGT exhibit dependency on the thickness of the beam as shown in Figure 3.3(b)-(c).

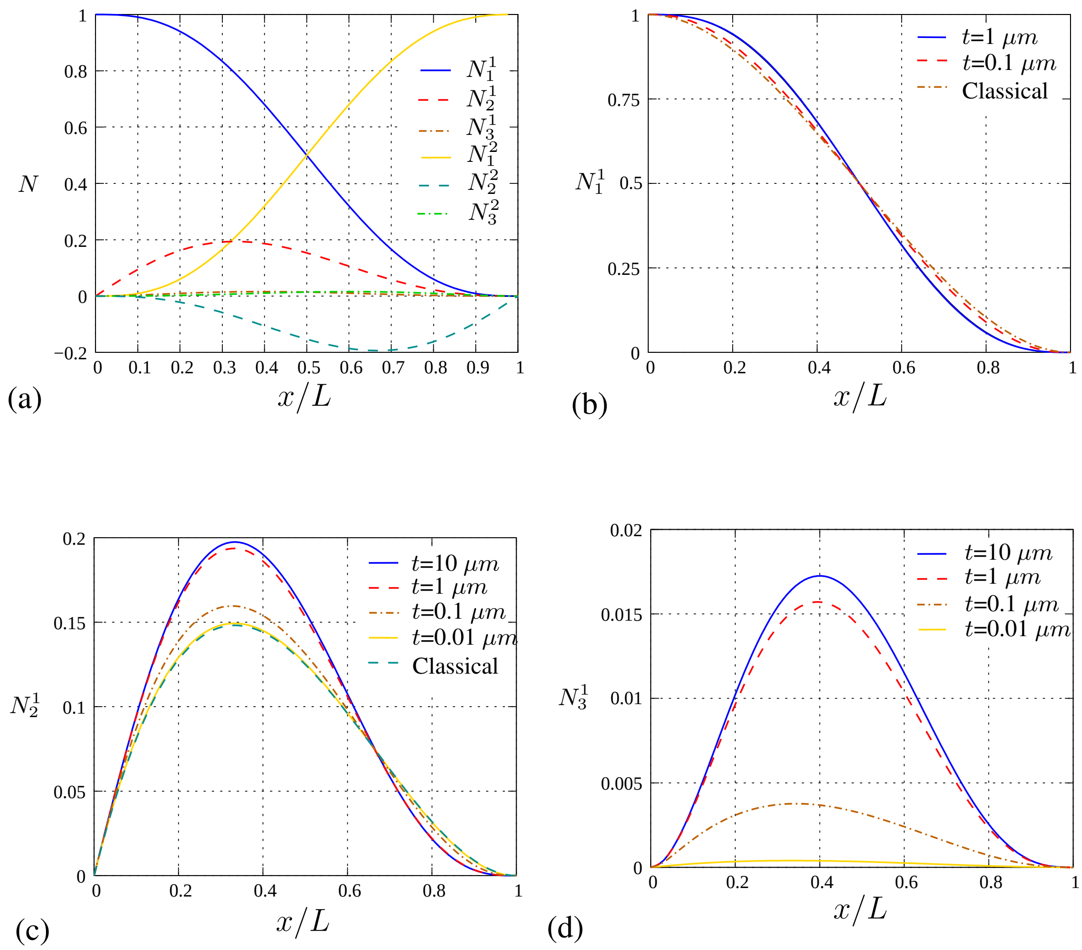

Figure 3.3: Shape functions for MSGT, (a) all elements of shape function matrix $\boldsymbol{N}$, (b) N_1^1, (c) N_2^1, and (d) N_3^1. For (b)-(d), the curves do not change significantly even if h is increased more than those given as the upper bound in the figures. They also approach to classical hermite cubic shape functions with decreasing values of h.

Incorporation of the discrete counterpart of the curvature in $(3.7)_3$ and its variation

$(3.8)_3$ into (2.29) one obtains the discrete counterpart for the equilibrium

$$\delta \Pi = \mathop{\mathbf{A}}_{e=1}^{n} \delta \boldsymbol{d}_e^T \boldsymbol{k}_e \, \boldsymbol{d}_e - \mathop{\mathbf{A}}_{e=1}^{n} \delta \boldsymbol{d}_e^T \boldsymbol{f}_e = 0 \,, \tag{3.19}$$

where

$$\boldsymbol{k}_e = \int_0^L \left[\left(\frac{d^2 \boldsymbol{N}}{dx^2} \right) c_1 \left(\frac{d^2 \boldsymbol{N}^T}{dx^2} \right) + \left(\frac{d^3 \boldsymbol{N}}{dx^3} \right) c_2 \left(\frac{d^3 \boldsymbol{N}^T}{dx^3} \right) \right] dx \,. \tag{3.20}$$

In implementation of this method, it is suggested to set higher order moments Q as zero.

3.1.2.2 Higher Order Euler-Bernoulli Beam Elements for MCST

With the prescribed nodal displacements and forces along with the solution to the homogeneous plate equation the same as in classical theory as given in Section 2.3.3, the shape functions are also equvalent to those in classical beam theory. With a similar derivation, the stiffness matrix can be found as

$$\boldsymbol{k}_e = \int_0^l \left[\left(\frac{d^2 \boldsymbol{N}(x)}{dx^2} \right)^T \left(EI + \mu b h l_2^2 \right) \left(\frac{d^2 \boldsymbol{N}(x)}{dx^2} \right) \right] dx \tag{3.21}$$

or

$$\boldsymbol{k}_e = \frac{EI + \mu b h l_2^2}{L^3} \begin{bmatrix} 12 & 6L & -12 & 6L \\ 6L & 4L^2 & -6L & 2L^2 \\ -12 & -6L & 12 & -6L \\ 6L & 2L^2 & -6L & 4L^2 \end{bmatrix} . \tag{3.22}$$

Again, the formulation yields the same results with MSGT when $l_0 = l_1 = 0$.

3.2 Kirchhoff-Love Plate Elements

3.2.1 Classical Kirchhoff-Love Plate Elements

A classical Kirchhoff-Love plate that is the direct extension of an Euler-Bernoulli beam including 4 nodes with 12 DOFs. The generalized nodal displacements and generalized nodal force resultants are

$$
\begin{aligned}
&1. \quad w = w_1, \quad \theta_x = \theta_{x1} \quad \text{and} \quad \theta_y = \theta_{y1} \quad \text{at} \quad x = 0,\ y = 0\,,\\
&2. \quad w = w_2, \quad \theta_x = \theta_{x2} \quad \text{and} \quad \theta_y = \theta_{y2} \quad \text{at} \quad x = L,\ y = 0\,,\\
&3. \quad w = w_3, \quad \theta_x = \theta_{x3} \quad \text{and} \quad \theta_y = \theta_{y3} \quad \text{at} \quad x = L,\ y = W\,,\\
&4. \quad w = w_4, \quad \theta_x = \theta_{x4} \quad \text{and} \quad \theta_y = \theta_{y4} \quad \text{at} \quad x = 0,\ y = W\,,
\end{aligned}
\tag{3.23}
$$

and

$$
\begin{aligned}
&1. \quad V = V_1, \quad M_x = M_{x1} \quad \text{and} \quad M_y = M_{y1} \quad \text{at} \quad x = 0,\ y = 0\,,\\
&2. \quad V = V_2, \quad M_x = M_{x2} \quad \text{and} \quad M_y = M_{y2} \quad \text{at} \quad x = l,\ y = 0\,,\\
&3. \quad V = V_3, \quad M_x = M_{x3} \quad \text{and} \quad M_y = M_{y3} \quad \text{at} \quad x = l,\ y = b\,,\\
&4. \quad V = V_4, \quad M_x = M_{x4} \quad \text{and} \quad M_y = M_{y4} \quad \text{at} \quad x = 0,\ y = b\,,
\end{aligned}
\tag{3.24}
$$

see Figure 3.4. Note that the subscripts for M terms are reduced, i.e. M_x=M_{xx} and

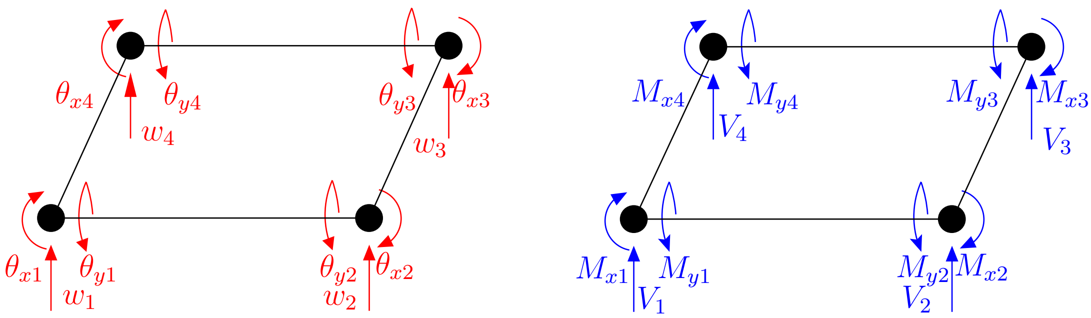

(a) (b)

Figure 3.4: (a) Nodal degrees of freedom and (b) corresponding nodal forces for a classical Kirchhoff-Love plate formulation

M_y=M_{yy} hereinafter in this study.

Accordingly, the element nodal displacement vector $\boldsymbol{d}$ and the element nodal force vector $\boldsymbol{f}$ read

$$
\boldsymbol{d}^T = [w_1 \;\; \theta_{x1} \;\; \theta_{y1} \; ... \; w_4 \;\; \theta_{x4} \;\; \theta_{y4}]\ , \quad \boldsymbol{f}^T = [V_1 \;\; M_{x1} \;\; M_{y1} \; ... \; V_4 \;\; M_{x4} \;\; M_{y4}]\ .
\tag{3.25}
$$

Then, the displacement field within $\mathcal{B}_e$ is interpolated as

$$
w(x,y) = \boldsymbol{N}\boldsymbol{d} = \sum_{i=1}^{n_{\mathrm{DOF}}} \sum_{j=1}^{n_{\mathrm{nodes}}} N_i^j d_i^j \quad \text{where} \quad \boldsymbol{N} = \left[N_1^1 \; N_2^1 \; N_3^1 ... N_1^4 \; N_2^4 \; N_3^4\right]\ ,
\tag{3.26}
$$

is the row vector including the set of interpolation/shape functions. Herein $n_{\text{DOF}} = 3$ and $n_{\text{nodes}} = 4$, indicating the number of degrees of freedom (DOFs) per node and the number of nodes per element similar to Section 3.1. Again for N_i^j, i denotes the relevant DOF of the node and j denotes the relevant node. The number of DOFs per element is hence 12.

The homogenous solution of the partial differential equation (2.52) is

$$\begin{aligned} w(x,y) = \quad & a_1 + a_2 x + a_3 y + a_4 x^2 + a_5 xy + a_6 y^2 \\ & + a_7 x^3 + a_8 x^2 y + a_9 xy^2 + a_{10} y^3 + a_{11} x^3 y + a_{12} xy^3 \,. \end{aligned} \tag{3.27}$$

This equation yields a 12-DOF plate element that is known as the ACM quadrilateral [149, 150]. It does not satisfy the C^1 continuity requirement, and therefore it is a non-conforming element. It is also an incomplete element and does not pass the patch test [156]. The first three of the twelve shape functions are as given in Figure 3.5, where the remaining nine are symmetric with respect to the two centroidal principal axes $\bar{x}$ and $\bar{y}$ around the geometric center of the element. Their analytical expressions are given in Appendix D [125]. The displacement w, rotation θ, and the curvature κ

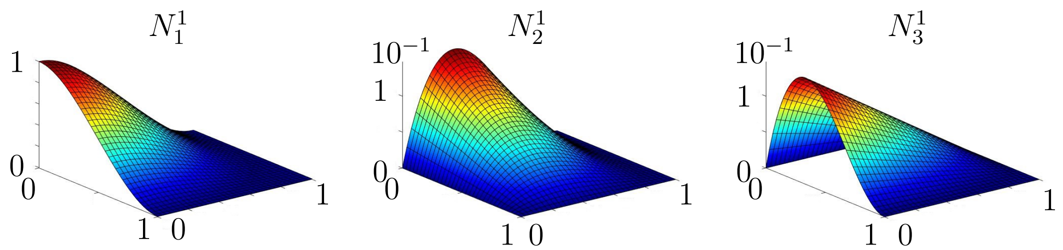

Figure 3.5: 12-DOF element shape functions from N_1 to N_3.

fields 2.47 can be approximated as

$$\begin{gathered} w(x,y) = \boldsymbol{N}(x,y)\boldsymbol{d}\,,\ \theta_x(x,y) = w_{,x}(x,y) = \frac{\partial \boldsymbol{N}(x,y)}{\partial x}\boldsymbol{d}\,, \\ \theta_y(x,y) = w_{,y}(x,y) = \frac{\partial \boldsymbol{N}(x,y)}{\partial y}\boldsymbol{d}\,,\ \kappa_{xx}(x,y) = w_{,xx}(x,y) = \frac{\partial^2 \boldsymbol{N}(x,y)}{\partial x^2}\boldsymbol{d}\,, \\ \kappa_{yy}(x,y) = w_{,yy}(x,y) = \frac{\partial^2 \boldsymbol{N}(x,y)}{\partial y^2}\boldsymbol{d}\,, \kappa_{xy}(x,y) = w_{,xy}(x,y) = \frac{\partial^2 \boldsymbol{N}(x,y)}{\partial x \partial y}\boldsymbol{d}\,. \end{gathered} \tag{3.28}$$

Consequently, the variation of these field variables in (2.51) are

$$\delta w(x,y) = \boldsymbol{N}(x,y)\delta\boldsymbol{d}\,,\ \delta\theta_x(x,y) = \delta w_{,x}(x,y) = \frac{\partial \boldsymbol{N}(x,y)}{\partial x}\delta\boldsymbol{d}\,,$$

$$\delta\theta_y(x,y) = \delta w_{,y}(x,y) = \frac{\partial \boldsymbol{N}(x,y)}{\partial y}\delta\boldsymbol{d}\,, \delta\kappa_{xx}(x,y) = \delta w_{,xx}(x,y) = \frac{\partial^2 \boldsymbol{N}(x,y)}{\partial x^2}\delta\boldsymbol{d}\,,$$

$$\delta\kappa_{yy}(x,y) = \delta w_{,yy}(x,y) = \frac{\partial^2 \boldsymbol{N}(x,y)}{\partial y^2}\delta\boldsymbol{d}\,,$$

$$\delta\kappa_{xy}(x,y) = \delta w_{,xy}(x,y) = \frac{\partial^2 \boldsymbol{N}(x,y)}{\partial x \partial y}\delta\boldsymbol{d}\,. \tag{3.29}$$

Incorporation of the discrete counterpart of the curvature in equation (3.28) and their variation (3.29) into (2.51)

$$\delta\mathit{\Pi} = \mathop{\mathsf{A}}_{e=1}^{n} \delta\boldsymbol{d}_e^T \boldsymbol{k}_e\, \boldsymbol{d}_e - \mathop{\mathsf{A}}_{e=1}^{n} \delta\boldsymbol{d}_e^T \boldsymbol{f}_e = 0\,, \tag{3.30}$$

where

$$\boldsymbol{k}_e = \int_{\partial\mathcal{B}} \left[(\nabla_C \boldsymbol{N})^T \boldsymbol{D}\, (\nabla_C \boldsymbol{N}) \right] d\mathcal{A} \quad \text{and} \quad \boldsymbol{f}_e = \int_{\partial\mathcal{B}} \boldsymbol{N}^T q(x) d\mathcal{A} \tag{3.31}$$

are the element stiffness matrix and the element nodal force vectors. Herein, the operator ∇_C is defined as

$$\nabla_C = \begin{bmatrix} \dfrac{\partial^2}{\partial x^2} & \dfrac{\partial^2}{\partial y^2} & 2\dfrac{\partial^2}{\partial x \partial y} \end{bmatrix}^T\,, \tag{3.32}$$

and A refers to the standard assembly of element contributions at the local element nodes where n denotes the total number of elements. In (3.31) the strain-displacement matrix is

$$\boldsymbol{B} = \nabla_C \boldsymbol{N}\,. \tag{3.33}$$

The global force vector assembled from local force vectors is $\boldsymbol{F} = \mathsf{A}_{e=1}^{n}\, \boldsymbol{f}_e$ and similarly, the global nodal displacement vector is $\boldsymbol{D} = \mathsf{A}_{e=1}^{n}\, \boldsymbol{d}_e$. The variation $\delta\boldsymbol{d} = 0$ at essential boundaries where the displacements are prescribed $\boldsymbol{d} = \bar{\boldsymbol{d}}$. The equilibrium should be satisfied for arbitrary variations $\delta\boldsymbol{d}$ yielding the set of linear algebraic equations as

$$\boldsymbol{K}\boldsymbol{D} = \boldsymbol{F}\,, \tag{3.34}$$

where $\boldsymbol{K} = \mathbf{A}_{e=1}^{n} \boldsymbol{k}_e$ is the global stiffness matrix. Substituting the shape functions into (3.31), the element stiffness matrix for the Kirchhoff-Love plate element is obtained.

3.2.2 Higher Order Kirchhoff-Love Plate Elements

Higher order Kirchhoff-Love microplate finite elements for MSGT have been developed as a novel aspect for the analysis of plate microstructures in Sections 3.2.2.1 and 3.2.2.2.

It is also noted that Kirchoff plate elements for MCST can be derived by:

- either by using the higher order formulation given in Sections 3.2.2.1 and 3.2.2.2 by inserting $l_0 = l_1 = 0$
- or using the classical formulation given in Section 3.2.1 by introducing $D + \mu h l_2^2$ instead of D terms.

based on the discussions in Section 2.

As in the higher order beam elements, in implementation of the methods discussed hereinafter, it is suggested to set higher order moments Q as zero.

3.2.2.1 Higher Order Rectangular Kirchhoff-Love Plate Elements for MSGT

3.2.2.1.1 20-DOF Elements

As a higher order extension of the ACM element, the generalized nodal displacements and the generalized nodal force resultants are proposed as

$$
\begin{aligned}
&1.\ w = w_1,\ \theta_x = \theta_{x1},\ \theta_y = \theta_{y1},\ \kappa_{xx} = \kappa_{xx1},\ \kappa_{yy} = \kappa_{yy1},\ \text{at } x = 0,\ y = 0\,,\\
&2.\ w = w_2,\ \theta_x = \theta_{x2},\ \theta_y = \theta_{y2},\ \kappa_{xx} = \kappa_{xx2},\ \kappa_{yy} = \kappa_{yy2},\ \text{at } x = L,\ y = 0\,,\\
&3.\ w = w_3,\ \theta_x = \theta_{x3},\ \theta_y = \theta_{y3},\ \kappa_{xx} = \kappa_{xx3},\ \kappa_{yy} = \kappa_{yy3},\ \text{at } x = L,\ y = W\,,\\
&4.\ w = w_4,\ \theta_x = \theta_{x4},\ \theta_y = \theta_{y4},\ \kappa_{xx} = \kappa_{xx4},\ \kappa_{yy} = \kappa_{yy4},\ \text{at } x = 0,\ y = W\,.
\end{aligned}
\tag{3.35}
$$

and

$$
\begin{aligned}
&1.\ V=V_1,\ M_x=M_{x1},\ M_y=M_{y1},\ Q_{xx}=Q_{xx1},\ Q_{yy}=Q_{yy1},\ \text{at } x=0,\ y=0\,,\\
&2.\ V=V_2,\ M_x=M_{x2},\ M_y=M_{y2},\ Q_{xx}=Q_{xx2},\ Q_{yy}=Q_{yy2},\ \text{at } x=L,\ y=0\,,\\
&3.\ V=V_3,\ M_x=M_{x3},\ M_y=M_{y3},\ Q_{xx}=Q_{xx3},\ Q_{yy}=Q_{yy3},\ \text{at } x=L,\ y=W\,,\\
&4.\ V=V_4,\ M_x=M_{x4},\ M_y=M_{y4},\ Q_{xx}=Q_{xx4},\ Q_{yy}=Q_{yy4},\ \text{at } x=0,\ y=W\,.
\end{aligned}
\tag{3.36}
$$

as given in Figure 3.6. Note that the subscripts for Q terms are reduced, i.e. Q_{xx}=Q_{xxx} and Q_{yy}=Q_{yyy} hereinafter in this study.

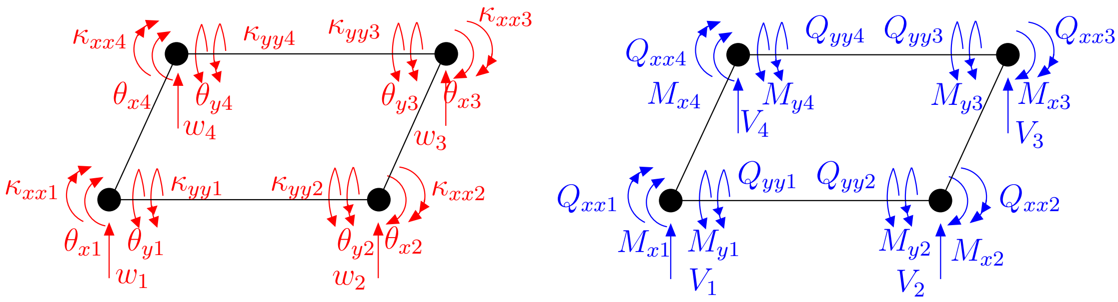

Figure 3.6: (a) Nodal degrees of freedom and (b) corresponding nodal forces for a 20-DOF higher order Kirchhoff-Love plate formulation based on MSGT.

Similarly, the element nodal displacement vector $\boldsymbol{d}$ and the element nodal force vector $\boldsymbol{f}$ read

$$
\begin{aligned}
\boldsymbol{d}^T &= [\, w_1\ \ \theta_{x1}\ \ \theta_{y1}\ \ \kappa_{xx1}\ \ \kappa_{yy1}\ \ \ldots\ \ w_4\ \ \theta_{x4}\ \ \theta_{y4}\ \ \kappa_{xx4}\ \ \kappa_{yy4}\,]\,,\\
\boldsymbol{f}^T &= [\, V_1\ \ M_{x1}\ \ M_{y1}\ \ Q_{xx1}\ \ Q_{yy1} \ldots\ \ V_4\ \ M_{x4}\ \ M_{y4}\ \ Q_{xx1}\ \ Q_{yy1}\,]\,.
\end{aligned}
\tag{3.37}
$$

Then, the displacement field within $\mathcal{B}_e$ is interpolated as

$$
\begin{aligned}
w(x,y) &= \boldsymbol{N}\boldsymbol{d} = \textstyle\sum_{i=1}^{n_{\text{DOF}}} \sum_{j=1}^{n_{\text{nodes}}} N_i^j d_i^j \qquad \text{where}\\
\boldsymbol{N} &= [N_1^1\ N_2^1\ N_3^1\ N_4^1\ N_5^1\ \ldots\ N_1^4\ N_2^4\ N_3^4\ N_4^4\ N_5^4]\,.
\end{aligned}
\tag{3.38}
$$

Herein $n_{\text{DOF}}=5$ and $n_{\text{nodes}}=4$. The number of DOFs per element is hence 20.

We propose the homogenous solution for the partial differential equation (2.63) in the form

$$
\begin{aligned}
w(x,y) = \quad & a_1 + a_2x + a_3y + a_4x^2 + a_5xy + a_6y^2 + \\
& a_7x^3 + a_8x^2y + a_9xy^2 + a_{10}y^3 + a_{11}x^3y + a_{12}xy^3 + \\
& a_{13}\sinh(Ax) + a_{14}\cosh(Ax) + a_{15}\sinh(By) + a_{16}\cosh(By) + \\
& a_{17}\sinh(Ax)y + a_{18}\cosh(Ax)y + a_{19}\sinh(By)x + a_{20}\cosh(By)x\,.
\end{aligned} \tag{3.39}
$$

with

$$
A = L\sqrt{\frac{d_1}{d_4}}, \quad B = W\sqrt{\frac{d_1}{d_4}} \tag{3.40}
$$

The use of hyperbolic sine and hyperbolic cosine terms are in fact motivated by the nature of the plate equation with fourth and sixth order terms (2.63). This solution naturally extends the MSGT based Euler-Bernoulli beam solution to Kirchhoff-Love plate solution, see reference [157]. We propose 20 shape functions that satisfy the homogeneous solution 3.39 that extends the ACM element to the higher order Kirchhoff-Love plate element. The first five of these shape functions (i.e. those for the first node) are shown in Figure 3.7. The remaining fifteen are symmetric with respect to two centroidal principal axes of the element. The analytic expressions for the shape functions N_i^j of the MSGT-based Kirchoff plate element are given in ?E. The shape functions N_1^j, N_2^j and N_3^j recover their classical counterparts in ACM element for j'th node whereas N_4^j and N_5^j vanish as length scale parameters tends to zero.

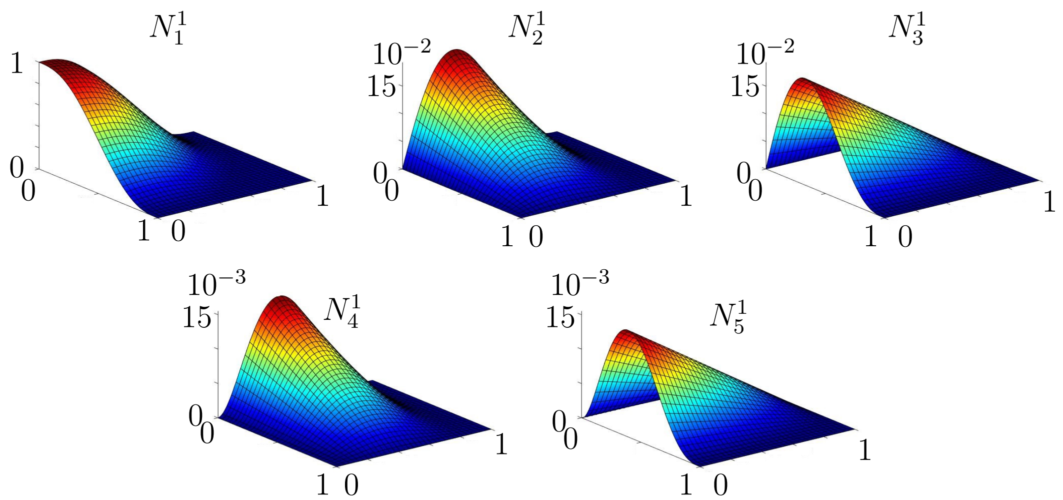

Figure 3.7: First five shape functions for the new Kirchhoff-Love plate element in MSGT (of the 1st node). $l_0 = l_1 = l_2 = 3.71\ \mu m$ as given in the forthcoming section.

The higher order out-of-plane curvatures (2.54) are

$$
\begin{aligned}
\varrho_{xxx}(x,y) &= w_{,xxx}(x,y) = \frac{\partial^3 \boldsymbol{N}(x,y)}{\partial x^3}\boldsymbol{d}\,,\\
\varrho_{xxy}(x,y) &= w_{,xxy}(x,y) = \frac{\partial^3 \boldsymbol{N}(x,y)}{\partial x^2 \partial y}\boldsymbol{d}\,,\\
\varrho_{xyy}(x,y) &= w_{,xyy}(x,y) = \frac{\partial^3 \boldsymbol{N}(x,y)}{\partial x \partial y^2}\boldsymbol{d}\,,\\
\varrho_{yyy}(x,y) &= w_{,yyy}(x,y) = \frac{\partial^3 \boldsymbol{N}(x,y)}{\partial y^3}\boldsymbol{d}\,.
\end{aligned}
\tag{3.41}
$$

Consequently, the variation fields for the relevant terms in (2.61) are then

$$
\begin{aligned}
\delta\varrho_{xxx}(x,y) &= \delta w_{,xxx}(x,y) = \frac{\partial^3 \boldsymbol{N}(x,y)}{\partial x^3}\delta\boldsymbol{d}\,,\\
\delta\varrho_{xxy}(x,y) &= \delta w_{,xxy}(x,y) = \frac{\partial^3 \boldsymbol{N}(x,y)}{\partial x^2 \partial y}\delta\boldsymbol{d}\,,\\
\delta\varrho_{xyy}(x,y) &= \delta w_{,xyy}(x,y) = \frac{\partial^3 \boldsymbol{N}(x,y)}{\partial x \partial y^2}\delta\boldsymbol{d}\,,\\
\delta\varrho_{yyy}(x,y) &= \delta w_{,yyy}(x,y) = \frac{\partial^3 \boldsymbol{N}(x,y)}{\partial y^3}\delta\boldsymbol{d}\,.
\end{aligned}
\tag{3.42}
$$

along with those in (3.29). These are also the variatonal derivatives of displacement field appearing in (B.50).

Incorporation of the discrete counterpart of the curvature in (3.28) and higher order curvature in (3.41), and consequently their variations in equations (3.29,3.42) along with (2.61,2.62) into (2.7) yields

$$
\delta\Pi = \mathop{\mathbf{A}}_{e=1}^{n} \delta\boldsymbol{d}_e^T \boldsymbol{k}_e\, \boldsymbol{d}_e - \mathop{\mathbf{A}}_{e=1}^{n} \delta\boldsymbol{d}_e^T \boldsymbol{f}_e = 0\,. \tag{3.43}
$$

where

$$
\begin{aligned}
\boldsymbol{k}_e &= \int_{\partial\mathcal{B}} \left[(\nabla_C \boldsymbol{N})^T \boldsymbol{E_C}\,(\nabla_C \boldsymbol{N}) + (\nabla_H \boldsymbol{N})^T \boldsymbol{E_H}\,(\nabla_H \boldsymbol{N})\right] d\mathcal{A} \quad \text{and}\\
\boldsymbol{f}_e &= \int_{\partial\mathcal{B}} \boldsymbol{N}^T q(x) d\mathcal{A}
\end{aligned}
\tag{3.44}
$$

are the element stiffness matrix and the element nodal force vector (Figure 3.6b) respectively. ∇_C is defined as before and ∇_H is defined as

$$
\nabla_H = \begin{bmatrix} \dfrac{\partial^3}{\partial x^3} & 3\dfrac{\partial^3}{\partial x^2 \partial y} & 3\dfrac{\partial^3}{\partial x \partial y^2} & \dfrac{\partial^3}{\partial y^3} \end{bmatrix}^T . \tag{3.45}
$$

There are two strain-displacement matrices in (3.44) that can be expressed as $\boldsymbol{B}$ and $\boldsymbol{B}'$ as

$$\boldsymbol{B} = \nabla_C \boldsymbol{N}\,, \quad \boldsymbol{B}' = \nabla_H \boldsymbol{N}\,. \tag{3.46}$$

The expressions for these are given in Appendix F.

By changing of variables (x, y) with (ξ_1, ξ_2), the stiffness matrix can be written as

$$\boldsymbol{k}_e = \int_{-1}^{1}\int_{-1}^{1} \left[(\nabla_C \boldsymbol{N})^T \boldsymbol{E}_C \,(\nabla_C \boldsymbol{N}) + (\nabla_H \boldsymbol{N})^T \,\mathbf{E}_H\, (\nabla_H \boldsymbol{N}) \right] \Big|_{x=g_1(\xi_1,\xi_2)} \Big|_{y=g_2(\xi_1,\xi_2)} \det(\boldsymbol{J}) d\xi_1 d\xi_2\,, \tag{3.47}$$

where the Jacobian of the transformation, i.e.

$$\boldsymbol{J} = \begin{bmatrix} \dfrac{\partial x}{\partial \xi_1} & \dfrac{\partial x}{\partial \xi_2} \\ \dfrac{\partial y}{\partial \xi_1} & \dfrac{\partial y}{\partial \xi_2} \end{bmatrix}, \tag{3.48}$$

see Figure 3.8.

Making use of two-point Gaussian quadrature, the element stiffness matrix is approximated as

$$\boldsymbol{k}_e = \sum_{i=1}^{2}\sum_{j=1}^{2} \left[(\nabla_C \boldsymbol{N})^T \,\mathbf{E}_C\, (\nabla_C \boldsymbol{N}) + (\nabla_H \boldsymbol{N})^T \,\mathbf{E}_H\, (\nabla_H \boldsymbol{N}) \right] \det(\boldsymbol{J})\; \Omega(\xi_1, \xi_2) \Big|_{\xi_1=\xi_1(i)} \Big|_{\xi_2=\xi_2(j)} \tag{3.49}$$

where $\xi_1(i)$, $\xi_2(j)$ and $\Omega(\xi_1(i), \xi_2(j))$ are the Gaussian quadrature points and the weight factors, respectively.

Since the energy equation (B.50) involves terms with third derivatives of displacement field $w(x, y)$, C^2 continuity is required for conformity. For an element boundary AB as given in Figure 3.9, this conformity would require w, $\delta w/\delta y$, and $\delta^2 w/\delta y^2$ to be uniquely defined in terms of the nodal degrees of freedoms, i.e. w, $\delta w/\delta x$, $\delta w/\delta y$, $\delta^2 w/\delta x^2$ and $\delta^2 w/\delta y^2$ at points A and B respectively (ten nodal variables). Similarly for an element boundary BC given in the same figure, w, $\delta w/\delta x$, and $\delta^2 w/\delta x^2$ need to be defined by the same nodal variables at B and C. For boundary AB, i.e. with x

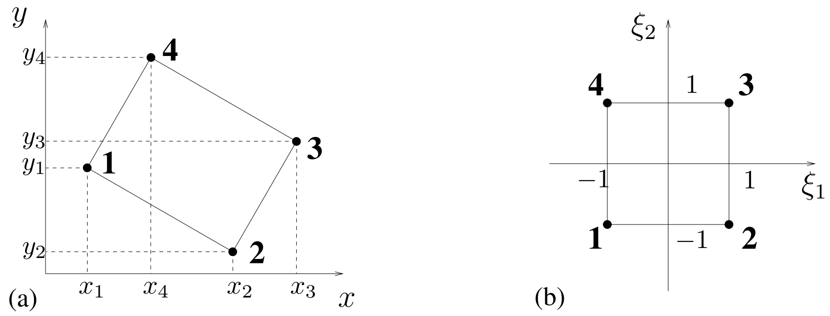

Figure 3.8: Coordinate transformation from (a) original coordinates to (b) mapped coordinates. Node numbers are indicated in bold.

constant:

$$w = C_0 + C_1 y + C_2 y^2 + C_3 y^3 + C_4 \sinh(By) + C_5 \cosh(By) \tag{3.50}$$

$$\frac{\delta w}{\delta y} = D_0 + D_1 y + D_2 y^2 + D_3 \cosh(By) + D_4 \sinh(By) \tag{3.51}$$

$$\frac{\delta^2 w}{\delta y^2} = E_0 + E_1 y + E_2 \sinh(By) + E_3 \cosh(By) \tag{3.52}$$

where C_n, D_n, E_n indicate fifteen unknown constants. However, for AB boundary, the nodal variables are prescribed are w, $\delta w/\delta x$, and $\delta^2 w/\delta x^2$, $\delta w/\delta y$, and $\delta^2 w/\delta y^2$ at nodes A and B, i.e. ten values. Hence, just like its conventional counterpart [156], it is not possible to specify a polynomial set for the shape functions that ensure compatibility. The applicability of the finite element is therefore validated by several tests as given in Section 4.1. Even if the element can be used for rectangular shapes, i.e. does not pass the patch test, an a posteriori error estimation could be made as given in the said section, along with convergence and numerical performance of the element.

3.2.2.1.2 24-DOF Elements

Another variant of the 20-DOF element is proposed in this study, i.e the 24-DOF plate element. Herein an additional generalized nodal displacement and generalized nodal force resultant to those of the 20-DOF version, i.e. those in Equations 3.35 and 3.36

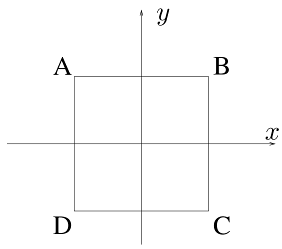

Figure 3.9: Element interfaces AB, BC, CD, and DA, at which either x or y is constant.

respectively are:

$$
\begin{aligned}
&1. \quad \kappa_{xy} = \kappa_{xy1} \quad \text{at} \quad x = 0,\ y = 0\,,\\
&2. \quad \kappa_{xy} = \kappa_{xy2} \quad \text{at} \quad x = L,\ y = 0\,,\\
&3. \quad \kappa_{xy} = \kappa_{xy3} \quad \text{at} \quad x = L,\ y = W\,,\\
&4. \quad \kappa_{xy} = \kappa_{xy4} \quad \text{at} \quad x = 0,\ y = W\,,
\end{aligned}
\tag{3.53}
$$

and

$$
\begin{aligned}
&1. \quad Q_{xy} = Q_{xy1} \quad \text{at} \quad x = 0,\ y = 0\,,\\
&2. \quad Q_{xy} = Q_{xy2} \quad \text{at} \quad x = L,\ y = 0\,,\\
&3. \quad Q_{xy} = Q_{xy3} \quad \text{at} \quad x = L,\ y = W\,,\\
&4. \quad Q_{xy} = Q_{xy4} \quad \text{at} \quad x = 0,\ y = W\,,
\end{aligned}
\tag{3.54}
$$

see Figure 3.10.

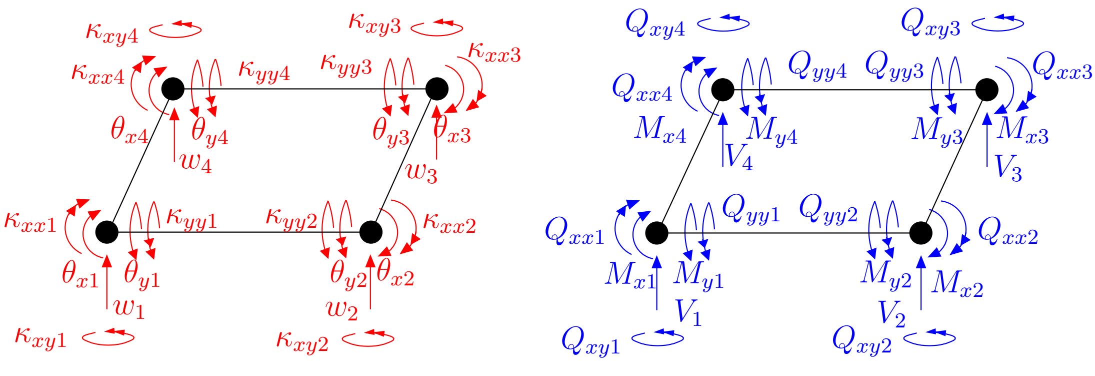

(a) (b)

Figure 3.10: (a) Nodal degrees of freedom and (b) corresponding nodal forces for a 24-DOF higher order Kirchhoff-Love plate formulation based on MSGT.

In this manner, it could be considered as the higher order extension of the BFS element [151]. Since the basics of the ACM element is given in Section 3.2.1, the same formulation is not given for BFS element in this study.

The element nodal displacement vector and the element nodal force vector are

$$
\begin{aligned}
\boldsymbol{d}^T = & \ [\, w_1 \ \ \theta_{x1} \ \ \theta_{y1} \ \ \kappa_{xx1} \ \ \kappa_{yy1} \ \ \kappa_{xy1} \ \ \ldots \ \ w_4 \ \ \theta_{x4} \ \ \theta_{y4} \ \ \kappa_{xx4} \ \ \kappa_{yy4} \ \ \kappa_{xy4} \,] \ , \\
\boldsymbol{f}^T = & \ [\, V_1 \ \ M_{x1} \ \ M_{y1} \ \ Q_{xx1} \ \ Q_{yy1} \ \ Q_{xy1} \ \ \ldots \ \ V_4 \ \ M_{x4} \ \ M_{y4} \ \ Q_{xx4} \ \ Q_{yy4} \ \ Q_{xy4} \,] \ .
\end{aligned}
\tag{3.55}
$$

Then, the displacement field within $\mathcal{B}_e$ is interpolated as

$$
\begin{aligned}
& w(x,y) = \boldsymbol{N}\boldsymbol{d} = \textstyle\sum_{i=1}^{n_{\text{DOF}}} \sum_{j=1}^{n_{\text{nodes}}} N_i^j d_i^j \qquad \text{where} \\
& \boldsymbol{N} = [N_1^1 \ N_2^1 \ N_3^1 \ N_4^1 \ N_5^1 \ N_6^1 \ldots \ N_1^4 \ N_2^4 \ N_3^4 \ N_4^4 \ N_5^4 \ N_6^4] \ .
\end{aligned}
\tag{3.56}
$$

Herein $n_{\text{DOF}} = 6$ and $n_{\text{nodes}} = 4$, yielding the number of DOFs per element as 24.

The homogenous solution for the partial differential equation (2.63) is proposed as

$$
\begin{aligned}
w(x,y) = \ & a_1 + a_2 x + a_3 y + a_4 x^2 + a_5 xy + a_6 y^2 + \\
& a_7 x^3 + a_8 x^2 y + a_9 x y^2 + a_{10} y^3 + a_{11} x^3 y + a_{12} x^2 y^2 + \\
& a_{13} x y^3 + a_{14} x^2 y^3 + a_{15} x^3 y^2 + a_{16} x^3 y^3 + \\
& a_{17} \sinh(Ax) + a_{18} \cosh(Ax) + a_{19} \sinh(By) + a_{20} \cosh(By) + \\
& a_{21} \sinh(Ax) y + a_{22} \cosh(Ax) y + a_{23} \sinh(By) x + a_{24} \cosh(By) x \ .
\end{aligned}
\tag{3.57}
$$

The five shape functions corresponding to common DOFs are similar to those of 20-DOF element, with the additional twist shape functions given as N_6^j. N_6^1 is depicted in Figure 3.11. The other N_6^j functions are geometrically symmetrical to N_6^1.

3.2.2.1.3 28- and 32-DOF Elements

Another set of 28- and 32-DOF elements are proposed, as variants of 20- and 24-DOF elements respectively, with the addition of the following generalized nodal displacements and generalized nodal force resultants:

$$
\begin{aligned}
&1. \quad \kappa_{xxy} = \kappa_{xxy1} \quad \text{and} \quad \kappa_{xyy} = \kappa_{xyy1}, \quad \text{at} \quad x = 0, \ y = 0 \, , \\
&2. \quad \kappa_{xxy} = \kappa_{xxy2} \quad \text{and} \quad \kappa_{xyy} = \kappa_{xyy2}, \quad \text{at} \quad x = L, \ y = 0 \, , \\
&3. \quad \kappa_{xxy} = \kappa_{xxy3} \quad \text{and} \quad \kappa_{xyy} = \kappa_{xyy3}, \quad \text{at} \quad x = L, \ y = W \, , \\
&4. \quad \kappa_{xxy} = \kappa_{xxy4} \quad \text{and} \quad \kappa_{xyy} = \kappa_{xyy4}, \quad \text{at} \quad x = 0, \ y = W \, ,
\end{aligned}
\tag{3.58}
$$

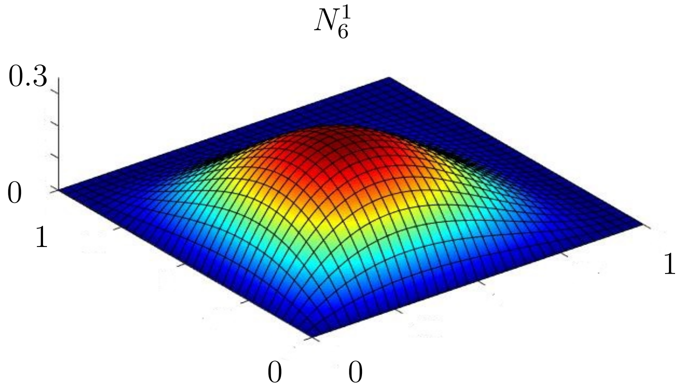

Figure 3.11: Additional twist DOF shape functions N_6^1. Other N_6^j terms are symmetric with respect to

and

$$\begin{aligned}
&1. \quad Q_{xxy} = Q_{xxy1} \quad \text{and} \quad Q_{xyy} = Q_{xyy1}, \quad \text{at} \quad x = 0,\ y = 0\,, \\
&2. \quad Q_{xxy} = Q_{xxy2} \quad \text{and} \quad Q_{xyy} = Q_{xyy2}, \quad \text{at} \quad x = L,\ y = 0\,, \\
&3. \quad Q_{xxy} = Q_{xxy3} \quad \text{and} \quad Q_{xyy} = Q_{xyy3}, \quad \text{at} \quad x = L,\ y = W\,, \\
&4. \quad Q_{xxy} = Q_{xxy4} \quad \text{and} \quad Q_{xyy} = Q_{xyy4}, \quad \text{at} \quad x = 0,\ y = W\,,
\end{aligned} \tag{3.59}$$

see Figures 3.12 and 3.13 respectively.

For the 28-DOF version, the element nodal displacement vector and the element nodal force vector are

$$\begin{aligned}
\boldsymbol{d}^T &= [w_1\ \theta_{x1}\ \theta_{y1}\ \kappa_{xx1}\ \kappa_{yy1}\ \kappa_{xxy1}\ \kappa_{xyy1} \ldots w_4\ \theta_{x4}\ \theta_{y4}\ \kappa_{xx4}\ \kappa_{yy4}\ \kappa_{xxy4}\ \kappa_{xyy4}]\,, \\
\boldsymbol{f} &= [V_1\ M_{x1}\ M_{y1}\ Q_{xx1}\ Q_{yy1}\ Q_{xxy1}\ Q_{xxy1} \ldots V_4\ \ M_{x4}\ M_{y4}\ Q_{xx4}\ Q_{yy4}\ Q_{xxy4}\ Q_{xyy4}]\,.
\end{aligned} \tag{3.60}$$

The displacement field within $\mathcal{B}_e$ is interpolated as

$$\begin{aligned}
&w(x,y) = \boldsymbol{N}\boldsymbol{d} = \textstyle\sum_{i=1}^{n_{\text{DOF}}} \sum_{j=1}^{n_{\text{nodes}}} N_i^j d_i^j \qquad \text{where} \\
&\boldsymbol{N} = [N_1^1\ N_2^1\ N_3^1\ N_4^1\ N_5^1\ N_6^1\ N_7^1 \ldots\ N_1^4\ N_2^4\ N_3^4\ N_4^4\ N_5^4\ N_6^4\ N_7^4]\,.
\end{aligned} \tag{3.61}$$

Herein $n_{\text{DOF}} = 7$ and $n_{\text{nodes}} = 4$, yielding the number of DOFs per element as 28.

The following homogenous solution for the partial differential equation 2.63 is pro-

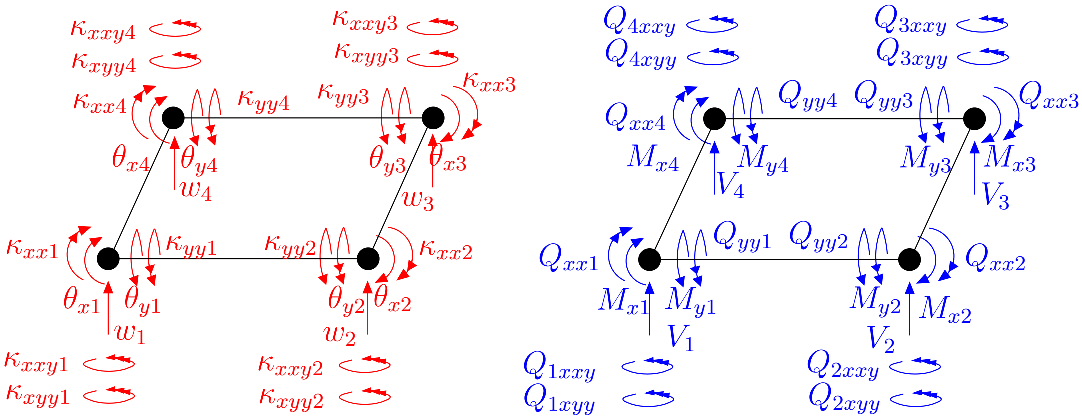

(a) (b)

Figure 3.12: (a) Nodal degrees of freedom and (b) corresponding nodal forces for a 28-DOF higher order Kirchhoff-Love plate formulation based on MSGT.

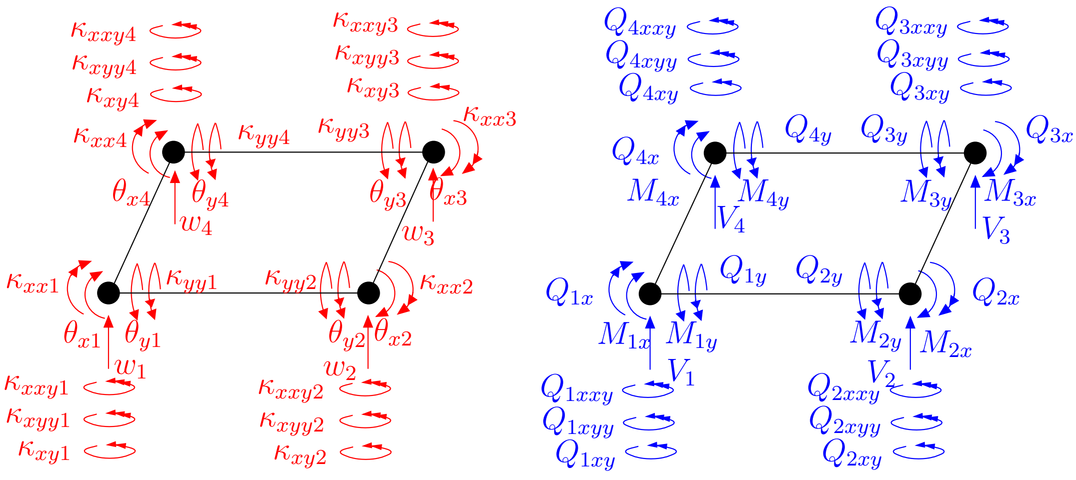

(a) (b)

Figure 3.13: (a) Nodal degrees of freedom and (b) corresponding nodal forces for a 32-DOF higher order Kirchhoff-Love plate formulation based on MSGT.

posed as

$$
\begin{aligned}
w(x,y) = {} & a_1 + a_2x + a_3y + a_4x^2 + a_5xy + a_6y^2 \\
& + a_7x^3 + a_8x^2y + a_9xy^2 + a_{10}y^3 + a_{11}x^3y + a_{12}xy^3 \\
& + a_{13}\sinh(Ax) + a_{14}\cosh(Ax) + a_{15}\sinh(By) + a_{16}\cosh(By) \\
& + a_{17}\sinh(Ax)y + a_{18}\cosh(Ax)y + a_{19}\sinh(By)x + a_{20}\cosh(By)x \\
& + a_{21}\sinh(Ax)y^2 + a_{22}\cosh(Ax)y^2 + a_{23}\sinh(By)x^2 + a_{24}\cosh(By)x^2 \\
& + a_{25}\sinh(Ax)y^3 + a_{26}\cosh(Ax)y^3 + a_{27}\sinh(By)x^3 + a_{28}\cosh(By)x^3\,.
\end{aligned} \tag{3.62}
$$

The element nodal displacement vector and the element nodal force vector for the 32-DOF element are

$$
\begin{aligned}
\boldsymbol{d}^T = & [w_1\ \theta_{x1}\ \theta_{y1}\ \kappa_{xx1}\ \kappa_{yy1}\ \kappa_{xy1}\ \kappa_{xxy1}\ \kappa_{xyy1} \\
& ...w_4\ \theta_{x4}\ \theta_{y4}\ \kappa_{xx4}\ \kappa_{yy4}\ \kappa_{xy4}\ \kappa_{xxy4}\ \kappa_{xyy4}]\,, \\
\boldsymbol{f} = & [V_1\ M_{x1}\ M_{y1}\ Q_{xx1}\ Q_{yy1}\ Q_{xy1}\ Q_{xxy1}\ Q_{xxy1} \\
& ...V_4\ \ M_{x4}\ M_{y4}\ Q_{xx4}\ Q_{yy4}\ Q_{xy4}\ Q_{xxy4}\ Q_{xyy4}]\,.
\end{aligned} \tag{3.63}
$$

The displacement field within $\mathcal{B}_e$ is interpolated as

$$
\begin{aligned}
& w(x,y) = \boldsymbol{N}\boldsymbol{d} = \textstyle\sum_{i=1}^{n_{\text{DOF}}} \sum_{j=1}^{n_{\text{nodes}}} N_i^j d_i^j \text{ where} \\
& \boldsymbol{N} = [N_1^1\ N_2^1\ N_3^1\ N_4^1\ N_5^1\ N_6^1\ N_7^1\ N_8^1 ... N_1^4\ N_2^4\ N_3^4\ N_4^4\ N_5^4\ N_6^4\ N_7^4\ N_8^4]\,.
\end{aligned} \tag{3.64}
$$

Herein $n_{\text{DOF}} = 8$ and $n_{\text{nodes}} = 4$, yielding the number of DOFs per element as 32.

The homogenous solution for the partial differential equation (2.63) is proposed as

$$
\begin{aligned}
w(x,y) = {} & a_1 + a_2x + a_3y + a_4x^2 + a_5xy + a_6y^2 \\
& + a_7x^3 + a_8x^2y + a_9xy^2 + a_{10}y^3 + a_{11}x^3y + a_{12}x^2y^2 \\
& + a_{13}xy^3 + a_{14}x^2y^3 + a_{15}x^3y^2 + a_{16}x^3y^3 \\
& + a_{17}\sinh(Ax) + a_{18}\cosh(Ax) + a_{19}\sinh(By) + a_{20}\cosh(By) \\
& + a_{21}\sinh(Ax)y + a_{22}\cosh(Ax)y + a_{23}\sinh(By)x + a_{24}\cosh(By)x \\
& + a_{25}\sinh(Ax)y^2 + a_{26}\cosh(Ax)y^2 + a_{27}\sinh(By)x^2 + a_{28}\cosh(By)x^2 \\
& + a_{29}\sinh(Ax)y^3 + a_{30}\cosh(Ax)y^3 + a_{31}\sinh(By)x^3 + a_{32}\cosh(By)x^3\,.
\end{aligned} \tag{3.65}
$$

For 28-DOF and 32-DOF elements to be derived from 20-DOF and 24-DOF elements respectively, 8 additional DOFs are required. These come from κ_{xxy} and κ_{xyy} terms, see (3.58) and (3.59). The shape functions for the first node associated with these DOFs are depicted in Figure 3.14, noting that the rest are symmetric to them with respect to the two principal centroidal axes. They are defined as

- N_6^j and N_7^j for the 28-DOF element, and

- N_7^j and N_8^j for the 32-DOF element (N_6^j are allocated for the twist shape function introduced in the 24-DOF element in Section 3.2.2.1.2).

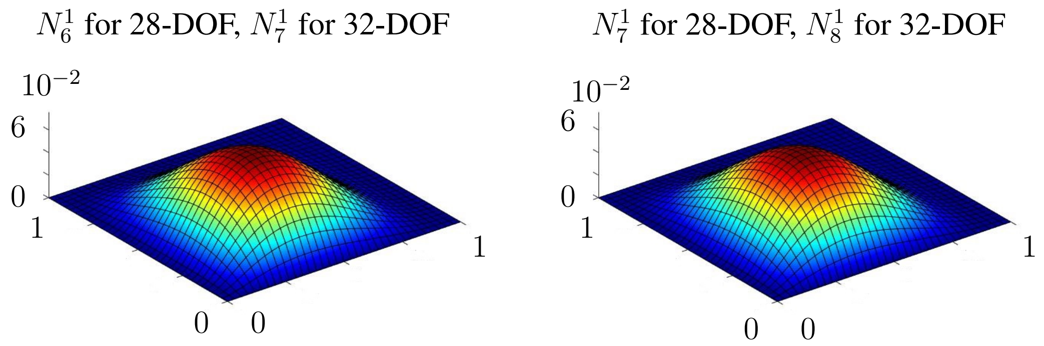

Figure 3.14: Two of the additional higher order twist DOF shape functions for 28-DOF and 32-DOF elements.

3.2.2.2 Higher Order Triangular Kirchhoff-Love Plate Elements for MSGT

A 18-DOF higher order triangular element based on MSGT is introduced in order to be used in combination with the 24-DOF rectangular elements. This enables one to analyze complex polygonal domains using both rectangular and triangular elements.

It has the following generalized nodal displacements as

$$
\begin{aligned}
&1. \quad w = w_1, \qquad \theta_x = \theta_{x1}, \qquad \theta_y = \theta_{y1}, \\
&\quad\ \kappa_{xx} = \kappa_{xx1}, \quad \kappa_{yy} = \kappa_{yy1}, \quad \kappa_{xy} = \kappa_{xy1} \quad \text{at } x = 0,\ y = 0\,, \\
&2. \quad w = w_2, \qquad \theta_x = \theta_{x2}, \qquad \theta_y = \theta_{y2}, \\
&\quad\ \kappa_{xx} = \kappa_{xx2}, \quad \kappa_{yy} = \kappa_{yy2}, \quad \kappa_{xy} = \kappa_{xy2} \quad \text{at } x = L,\ y = 0\,, \\
&3. \quad w = w_3, \qquad \theta_x = \theta_{x3}, \qquad \theta_y = \theta_{y3}, \\
&\quad\ \kappa_{xx} = \kappa_{xx3}, \quad \kappa_{yy} = \kappa_{yy3}, \quad \kappa_{xy} = \kappa_{xy3} \quad \text{at } x = 0,\ y = W\,.
\end{aligned}
\tag{3.66}
$$

These generalized nodal displacements are the same as those in Bell element [135], see Figure 3.15(a). The generalized nodal force resultants are

$$
\begin{aligned}
&1. \quad V = V_1, \qquad M_x = M_{x1}, \quad M_y = M_{y1}, \\
&\quad\ Q_{xx} = Q_{xx1}, \quad Q_{yy} = Q_{yy1}, \quad Q_{xy} = Q_{xy1} \quad \text{at } x = 0,\ y = 0\,. \\
&2. \quad V = V_2, \qquad M_x = M_{x2}, \quad M_y = M_{y2}, \\
&\quad\ Q_{xx} = Q_{xx2}, \quad Q_{yy} = Q_{yy2}, \quad Q_{xy} = Q_{xy2} \quad \text{at } x = L,\ y = 0\,. \\
&3. \quad V = V_3, \qquad M_x = M_{x3}, \quad M_y = M_{y3}, \\
&\quad\ Q_{xx} = Q_{xx3}, \quad Q_{yy} = Q_{yy3}, \quad Q_{xy} = Q_{xy3} \quad \text{at } x = 0,\ y = W\,,
\end{aligned}
\tag{3.67}
$$

see Figure 3.15(b).

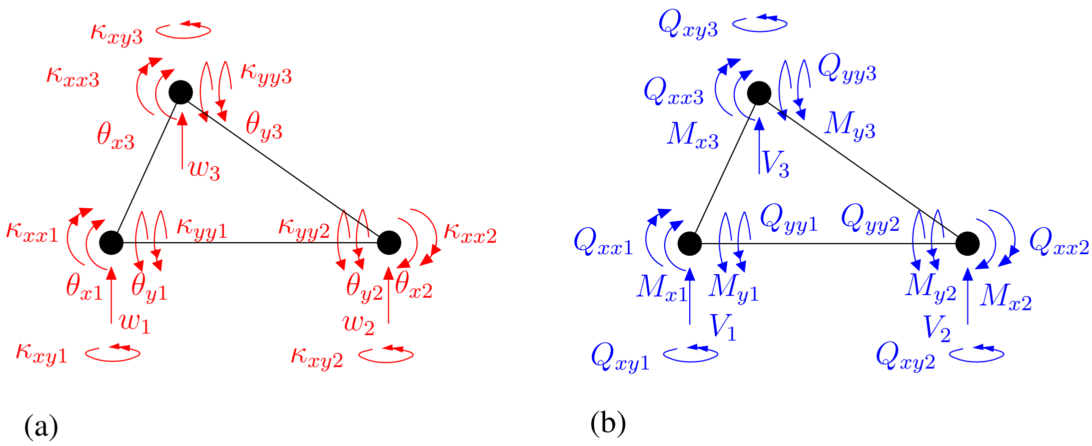

Figure 3.15: (a) Nodal degrees of freedom and (b) corresponding nodal forces for a 18-DOF higher order triangular Kirchhoff-Love plate formulation based on MSGT.

The element nodal displacement vector and the element nodal force vector are

$$\begin{aligned} \boldsymbol{d}^T = & \ [\, w_1 \ \ \theta_{x1} \ \ \theta_{y1} \ \ \kappa_{xx1} \ \ \kappa_{yy1} \ \ \kappa_{xy1} \ \ \ldots \ \ w_3 \ \ \theta_{x3} \ \ \theta_{y3} \ \ \kappa_{xx3} \ \ \kappa_{yy3} \ \ \kappa_{xy3} \,] \ , \\ \boldsymbol{f}^T = & \ [\, V_1 \ \ M_{x1} \ \ M_{y1} \ \ Q_{xx1} \ \ Q_{yy1} \ \ Q_{xy1} \ \ \ldots \ \ V_3 \ \ M_{x3} \ \ M_{y3} \ \ Q_{xx3} \ \ Q_{yy3} \ \ Q_{xy3} \,] \ . \end{aligned} \tag{3.68}$$

The displacement field within $\mathcal{B}_e$ is interpolated as

$$\begin{aligned} & w(x, y) = \boldsymbol{N}\boldsymbol{d} = \textstyle\sum_{i=1}^{n_{\text{DOF}}} \sum_{j=1}^{n_{\text{nodes}}} N_i^j d_i^j \text{ where} \\ & \boldsymbol{N} = [N_1^1 \ \ N_2^1 \ \ N_3^1 \ \ N_4^1 \ \ N_5^1 \ \ N_6^1 \ \ \ldots \ \ N_1^3 \ \ N_2^3 \ \ N_3^3 \ \ N_4^3 \ \ N_5^3 \ \ N_6^3 \,] \ . \end{aligned} \tag{3.69}$$

Similar to the 24-DOF rectangular element, $n_{\text{DOF}} = 6$. With $n_{\text{nodes}} = 3$, the number of DOFs is 18.

A homogenous solution for the partial differential equation (2.63) is proposed in the form of hyperbolic sine and cosine terms added to the hermite cubic polynomials, such that

$$\begin{aligned} w(x, y) = {} & a_1 + a_2 x + a_3 y + a_4 x^2 + a_5 xy + a_6 y^2 + a_7 x^3 + a_8 x^2 y + a_9 xy^2 + a_{10} y^3 + \\ & a_{11} \sinh(Ax) + a_{12} \cosh(Ax) + a_{13} \sinh(By) + a_{14} \cosh(By) + \\ & a_{15} \sinh(Ax) y + a_{16} \cosh(Ax) y + a_{17} \sinh(By) x + a_{18} \cosh(By) x \, . \end{aligned} \tag{3.70}$$

The shape functions for the corresponding 6 DOFs at the first node N_i^1 are depicted in Figure 3.16. The comparison of the corresponding shape functions for the relevant DOFs with those of the rectangular 24-DOF element are also given in Figure 3.17 and Figure 3.18 with multiple views from top and bottom.

Having the exactly same DOFs as in Bell element [135], the interpolation functions and inclusion of the length scale parameter differ significantly. Despite this, the shape function of the element seems to be in good alignment with those of Argyris element [3] as discussed further (see Figure 3.19).

As seen from the Figures 3.17(a)-(e) and 3.18, all the shape functions from N_1^1 to N_1^5 of the triangular element are in complete alignment with those of the 24-DOF rectangular element. This is also verified by the relatively lower order of magnitude of the differences. Moreover, the maximum difference occurs at the triangular diagonal, i.e. the boundary where the triangular shape functions should vanish, whereas rectangular

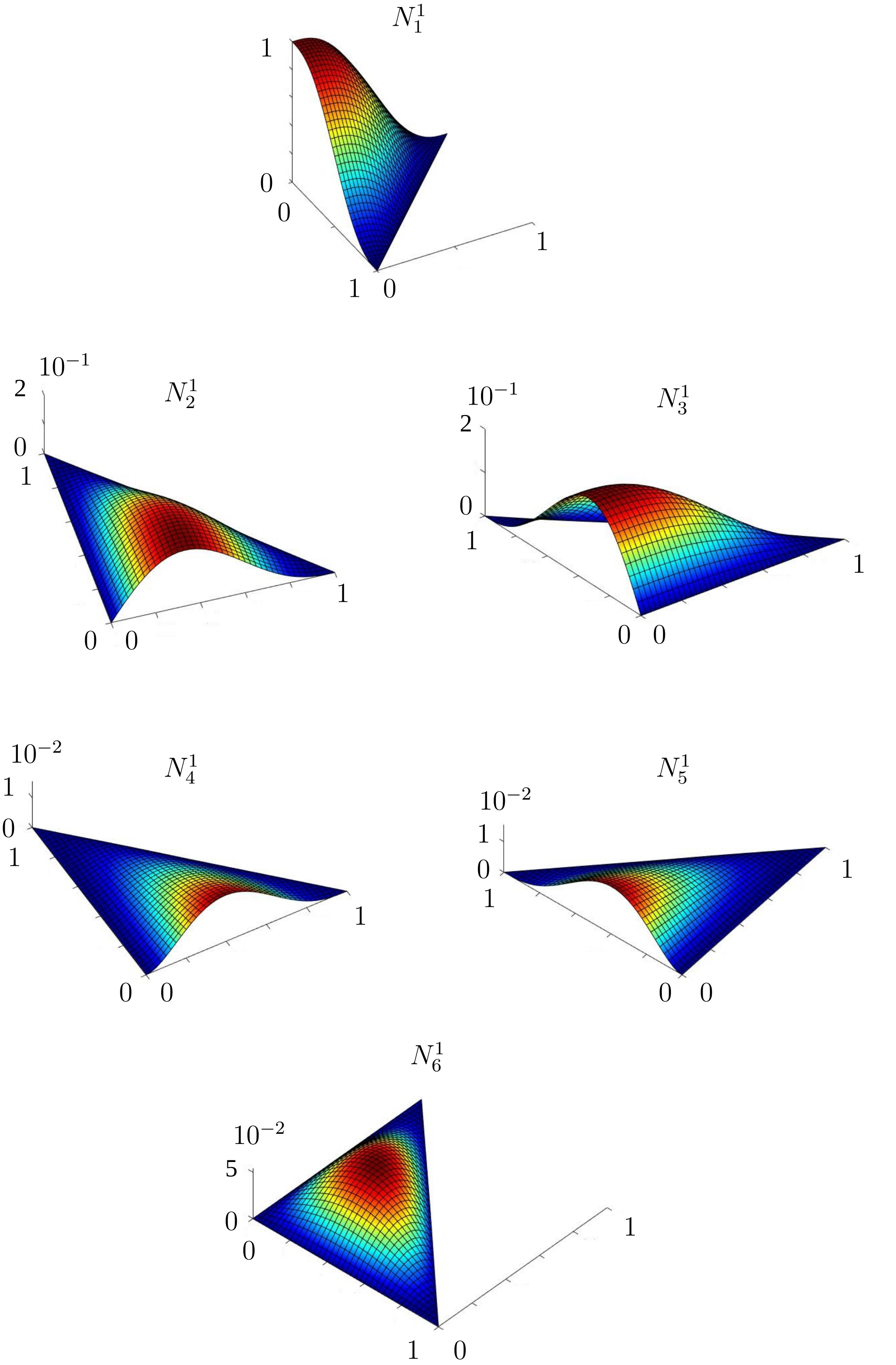

Figure 3.16: Shape functions for the first node for the newly developed 18-DOF triangular element.

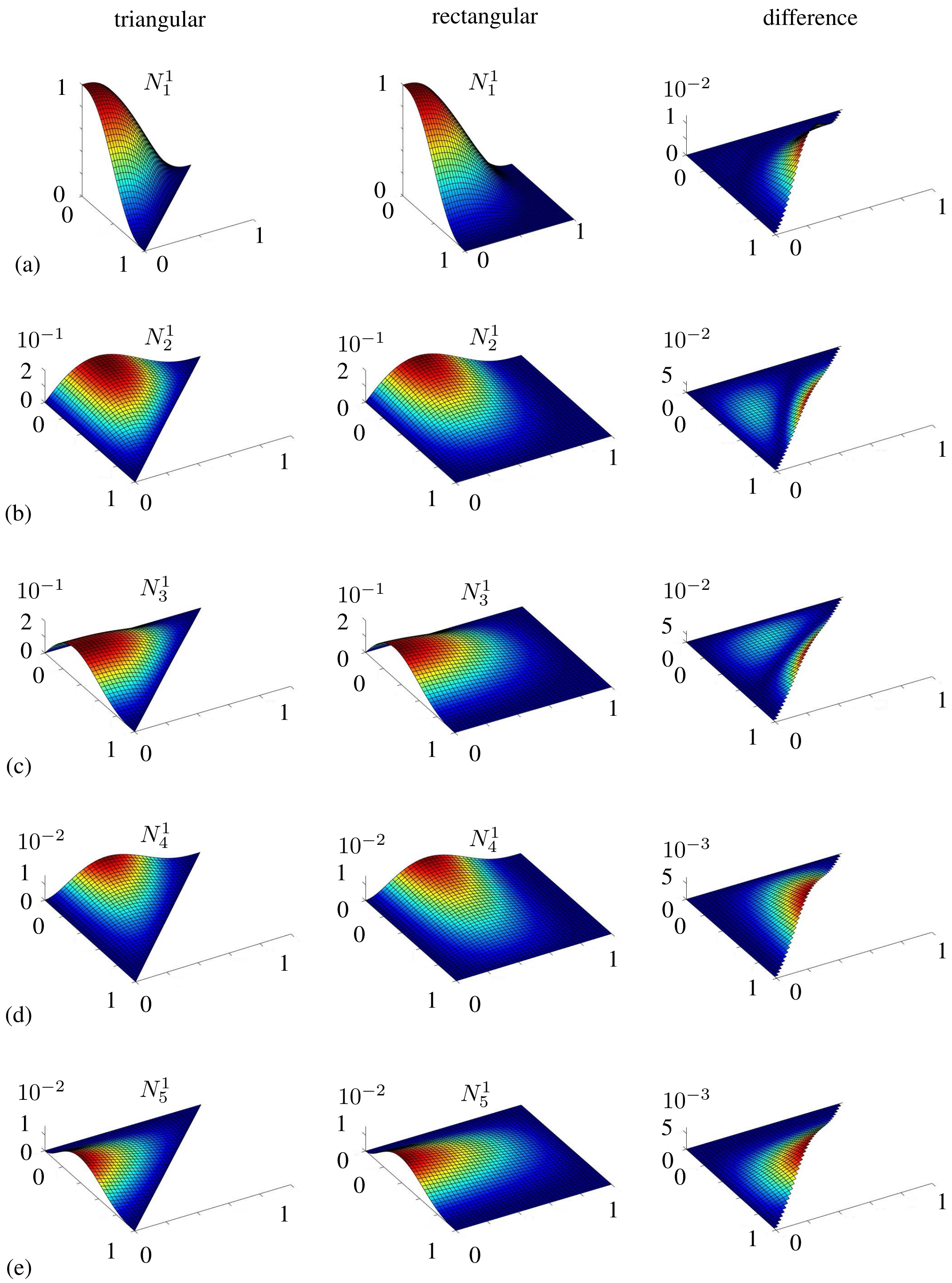

Figure 3.17: The first five shape functions for the first node (a)-(e) for the newly developed 18-DOF triangular element (left column) and for the newly developed 24-DOF rectangular element (middle column), along with the difference of two (right column).

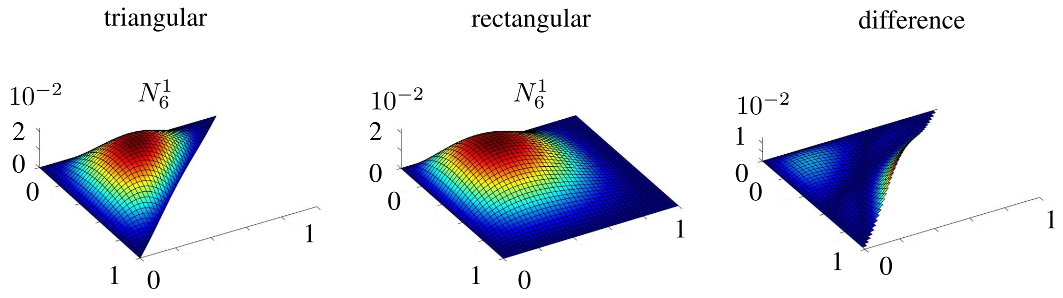

Figure 3.18: The sixth shape function for the first node for the newly developed 18-DOF triangular element (left column) and for the newly developed 24-DOF rectangular element (middle column), along with the difference of two (right column).

shape functions should not, as expected. The N_6^j associated with the in-plane twist DOF for the triangular element need to be divided by a factor, particularly 2.47, to be aligned as given in Figure 3.18. In the finite element formulation, the reduction by 2.47 is utilized for the triangular element to match the elastic behavior introduced by the 24-DOF rectangular element.

The new triangular element is also compared with the classical elements in literature, namely 10-DOF cubic Hermite triangular elements [4] and 21-DOF Argyris elements [3], in terms of corresponding shape functions for the available ones, i.e. N_1^1 and N_2^1 in Figure 3.19.

The newly developed 18-DOF element is in alignment with the Argyris element for as in Figure 3.19(a) and (b). It does not seem to be in good compliance with the cubic Hermite element (Figure 3.19(c) and (d) given the higher order of magnitude. However, since both cubic Hermite and Argyris elements are extensively used in finite element analysis, the 18-DOF triangular element also seems fit particularly when the shape functions are analyzed. The shape functions also seem to be in good alignment with studies in literature [158], especially with that of Ferreira and Bittencourt's classical fifth order hermite Kirchhoff-Love element [159].

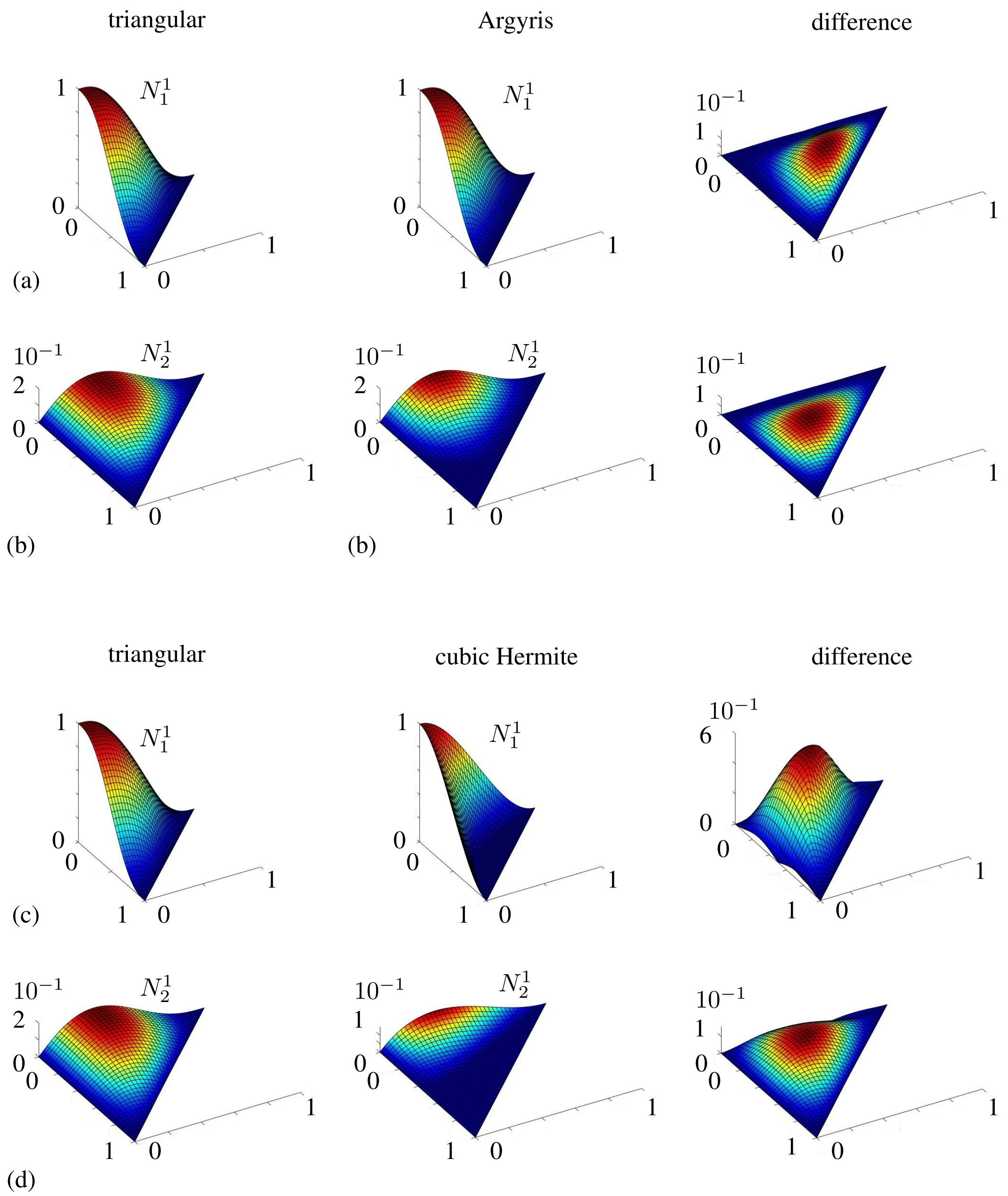

Figure 3.19: Comparison of the shape functions: (a) N_1^1 for Argyris and 18-DOF elements, (b) N_2^1 for Argyris and 18-DOF elements, (c) N_1^1 for cubic Hermite and 18-DOF elements, (d) N_2^1 for cubic Hermite and 18-DOF elements [3, 4].

CHAPTER 4

NUMERICAL STUDIES

In order to assess the performances of the finite elements proposed and discussed in Chapter 3 and furthermore propose length scale parameters for gold, several hypothetical cases and examples from literature are solved numerically. To this end, the finite element method developed previously is implemented into the finite element program developed within the scope of this study.

Throughout this section material parameters specific to gold are used unless otherwise specified [157]. Herein, different length scale parameters are specified for rectangular and triangular elements as justified in the examples. Benchmarks are performed based on studies conducted with epoxy. All material properties are outlined in Table 4.1.

Table 4.1: Material parameters used for gold and epoxy.

gold			epoxy		
parameter	value	unit	parameter	value	unit
E	80	[GPa]	E	1.44	[GPa]
ν	0.42	[–]	ν	0.38	[–]
$l_0 = l_1 = l_2$	3.71	[μm] (rectangular)	$l = l_0 = l_1 = l_2$	17.6	[μm]
$l_0 = l_1 = l_2$	4.77	[μm] (triangular)	N/A		

4.1 Assessment of Element Performance

In this section, the performance of the proposed MSGT-based Kirchhoff-Love plate element formulations are assessed under bending dominated loading conditions. There are two major parts in this assessment, namely rectangular and triangular plate elements respectively.

The first part is about the rectangular elelements and is initiated with a comparative analysis between the 20-, 24-, 28-, and 32-DOF elements. For both rectangular and triangular elements, two examples are concerned with the assessment of the performance of the proposed element formulation with respect to mesh irregularity. The mesh convergence of the elements are also studied for a square microplate subjected to various boundary and loading conditions. Several representative boundary value problems are investigated as a benchmark and the results are compared with those obtained from the classical theory. The convergence of the new MSGT elements are also discussed.

4.1.1 Rectangular Elements

4.1.1.1 Comparison

The newly developed 20-, 24-, 28-, and 32-DOF elements are compared with a case study in this section. For this purpose, a fixed-fixed plate with dimensions 20 $\mu m \times$ 5 $\mu m \times 1$ μm [157] is selected. A concentrated midpoint load of F_z=1 mN is applied as shown in Figure 4.1. Therein, square elements are used with a mesh of 32x8 elements, i.e. with a mesh density of 1.6 elements/μm at the edges.

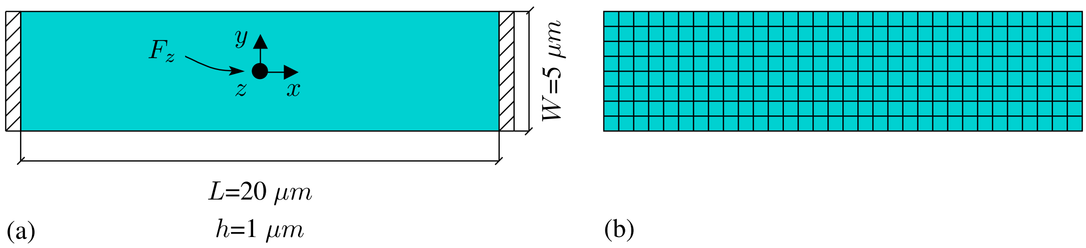

Figure 4.1: (a) Geometry and boundary conditions for the plate with dimensions L=20 μm, W=5 μm, h=1 μm under a load of F_z = 1 mN applied towards +z direction at the midpoint with the material properties given as in Table 4.1, (b) relevant mesh for the comparative analysis.

The resulting deflection field is shown in Figure 4.2. The deflection profiles of the principal centroidal axes of the plates are depicted in Figure 4.3(a) and (b) respectively. The difference between the models constructed with 20-, 24-, 28-, and 32-DOF elements are so insignificant -i.e. in the order of magnitude of 10^{-5} μm and smaller than 1% of the total tip deflection-, that the deflection profile looks almost the same in Figure 4.3(a). In Figure 4.3(b) the difference can be seen, along with a slight saddle effect that is expected due to Poisson effect [122].

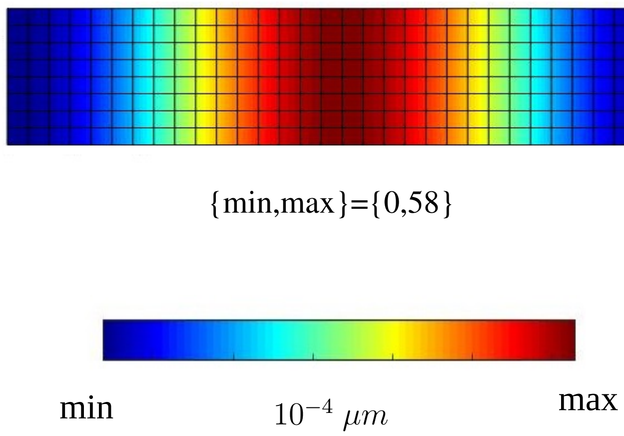

Figure 4.2: Deflection field for the $20 \times 5 \times 1$ μm plate under a midpoint load F = 1 mN and boundary conditions given in Figure 4.1 with the material properties given as in Table 4.1.

Since the results turn out to be almost equivalent with different types of elements, 20-DOF element is selected to be used hereinafter in this study for rectangular elements unless otherwise stated, for the sake of convenience and brevity.

4.1.1.2 Irregular Mesh and Refinement Tests

The proposed MSGT-based Kirchhoff-Love microplate element can be used for rectangular elements similar to its classical counterpart, the ACM plate element. The developed higher order microplate recovers the ACM element for vanishing length scale parameters. Although some respectable sources indicate that the ACM element

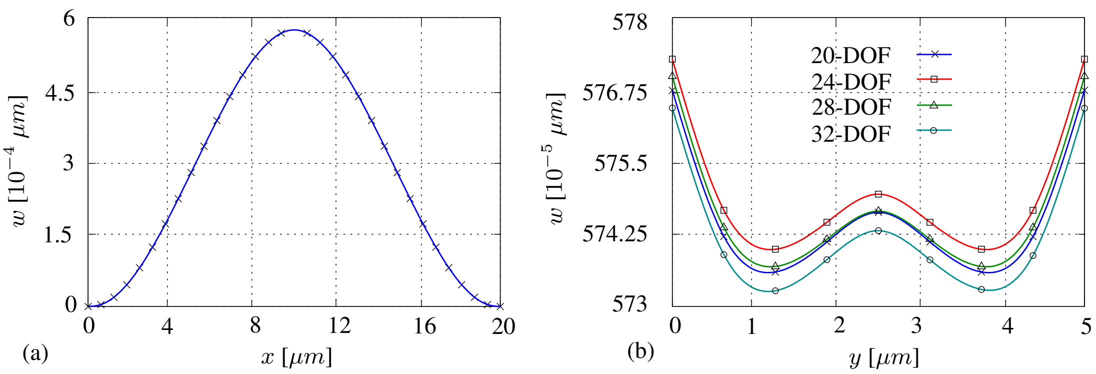

Figure 4.3: Deflection profiles of the two principal centroidal axes for the models constructed with 20-, 24-, 28-, 32-DOF elements, (a) for the principal axis along x-direction, and (b) for the principal axis along y-direction.

passes the patch test, they also conclude that the usage area should be confined to rectangular meshes [156]. The proposed formulation shows similar performance to ACM element under distorted element geometries. For this purpose the investigation of the convergence behavior upon mesh refinement and the element performance is confined to irregular rectangular meshes. To this end, the convergence of the displacement field for a square plate subjected to a point load is investigated for various boundary conditions, Additionally, the sensitivity of the displacement field to mesh irregularity under prescribed displacement/rotation field is investigated.

4.1.1.2.1 Microplate Response to Point Load

A fixed fixed $6\ \mu m \times 6\ \mu m \times 1\ \mu m$ microplate is subjected to a concentrated load of 1 mN applied at the centroid, as depicted in Figure 4.4(a). The problem is investigated with several meshes as shown in Figure 4.4 in order to assess its sensitivity to mesh irregularity. The corresponding deflection profiles are depicted in Figure 4.5(a), (b), (c), and (d).

The difference between centroidal deflections is smaller than 1% as seen in Figure 4.5, with the displacement fields aligned to a reasonably acceptable extent. In order to assess the largest difference in displacement fields, the midline deflections for the relevant nodes at $x = 0$ and $y = 0$ for the regular mesh and the irregular mesh

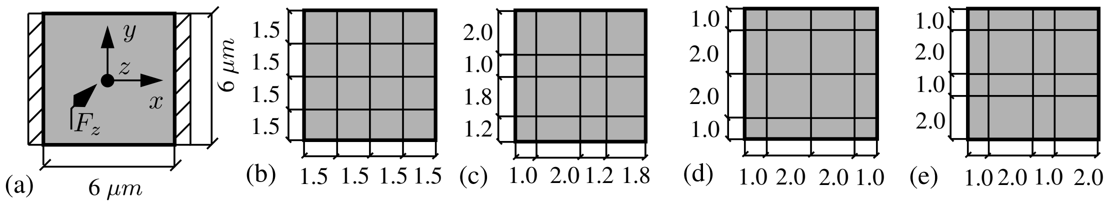

Figure 4.4: (a) Geometry and boundary conditions for square microplate. Thickness is taken as 1 μm and F_z = 1 mN.The problem is solved for (b) regular and (c), (d), (e) irregular mesh discretizations.

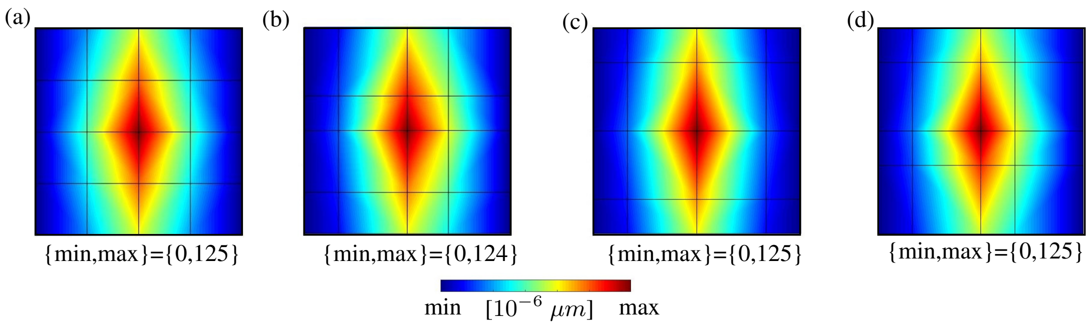

Figure 4.5: Contour plots depicting vertical displacement for the aspect ratio test given in Figure 4.4 for (a) regular mesh and (b, c, d) irregular meshes.

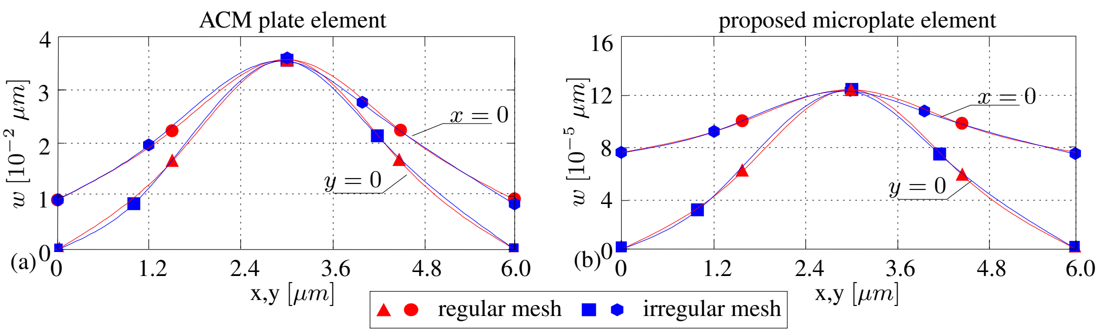

Figure 4.6: Midline deflections along $x-$ and $y-$axes obtained from the regular and irregular meshes depicted in Figure 4.5 for (a) classical theory ($l_i = 0$) and (b) proposed element formulation.

given in Figure 4.5(b) are given in Figure 4.6(a). The points correspond to the nodal displacement values along $x = 0$ and $y = 0$. The problem is also solved with ACM element and similar midline deflections are indicated in Figure 4.6(b). Therein, curves inbetween nodal values are interpolated with the element shape functions. It is seen that the deflections of the nodes for the regular and irregular meshes complement each other, to a degree slightly better than ACM element does for midline deflections in both directions. Although it is suggested that the element size variation such as aspect ratio change to be minimum as a best practice, varying aspect ratios does not yield erroneous results at least upto some extent, regarding displacement results.

4.1.1.2.2 Microplate response to displacement and rotation

In order to check the integrity of the formulation and consistency of the numerical implementation in x- and y-directions, the 6 $\mu m \times 6$ $\mu m \times 1$ μm microplate is subjected to a unit displacement and rotation at two perpendicular edges, respectively, see Figure 4.7 (first column).

Therein, the left edge is fixed along y-axis and the right edge is displaced $1 \mu m$ in z-direction, see Figure 4.7(a). Then, the same plate is subjected to a unit rotation (1 rad) about y-axis, see Figure 4.7(b). The same procedure is repeated for the perpendicular direction in 4.7(c) and 4.7(d), respectively. The simulation is first carried out with 4×4 regular mesh (second column) and for an irregular mesh (third column). Although the proposed element is shown to be nonconforming in Section 3.2.2.1.1, the displacement fields obtained from the regular and irregular meshes are nearly identical. The maximum difference in the displacement fields obtained from two different meshes less than 1%.

4.1.1.2.3 Mesh-refinement and convergence

The 6 $\mu m \times 6$ $\mu m \times 1$ μm is subjected to a concentrated midpoint load of 1 mN with both classical ACM elements and the proposed higher order microplate element. The the boundary conditions are specified as (i) fixed-fixed (two opposite edges clamped, two opposite edges free) and (ii) all sides fixed (all four edges clamped), see Fig-

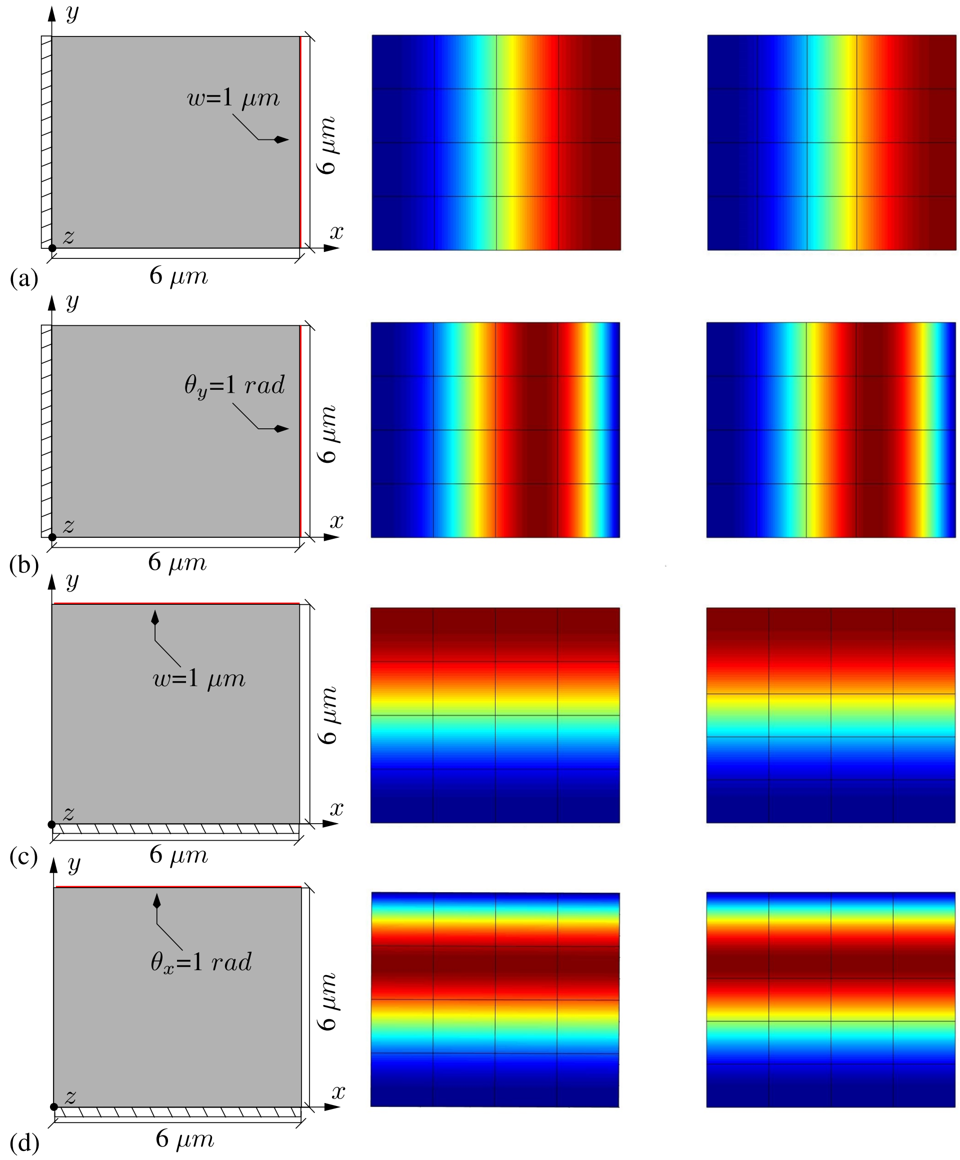

Figure 4.7: Geometry and boundary conditions (left) and corresponding displacement fields for the aspect ratio test considering response to prescribed displacements, for regular mesh (middle) and irregular mesh (right). The thickness of the plates is 1 μm for (a, b, c, d).

ure 4.8 (first column). The displacement profile for these boundary conditions on a 4x4 mesh are given in Figure 4.8 (second column). The midpoint deflections versus element per edge results are depicted in Figure 4.9(a)-(d), for the proposed element formulation and the ACM element, respectively. The proposed element formulation is converging slightly faster than the classical counterpart. The convergence behavior of the proposed element upon mesh-refinement, similar to the classical ACM element, is quite satisfactory for rectangular meshes.

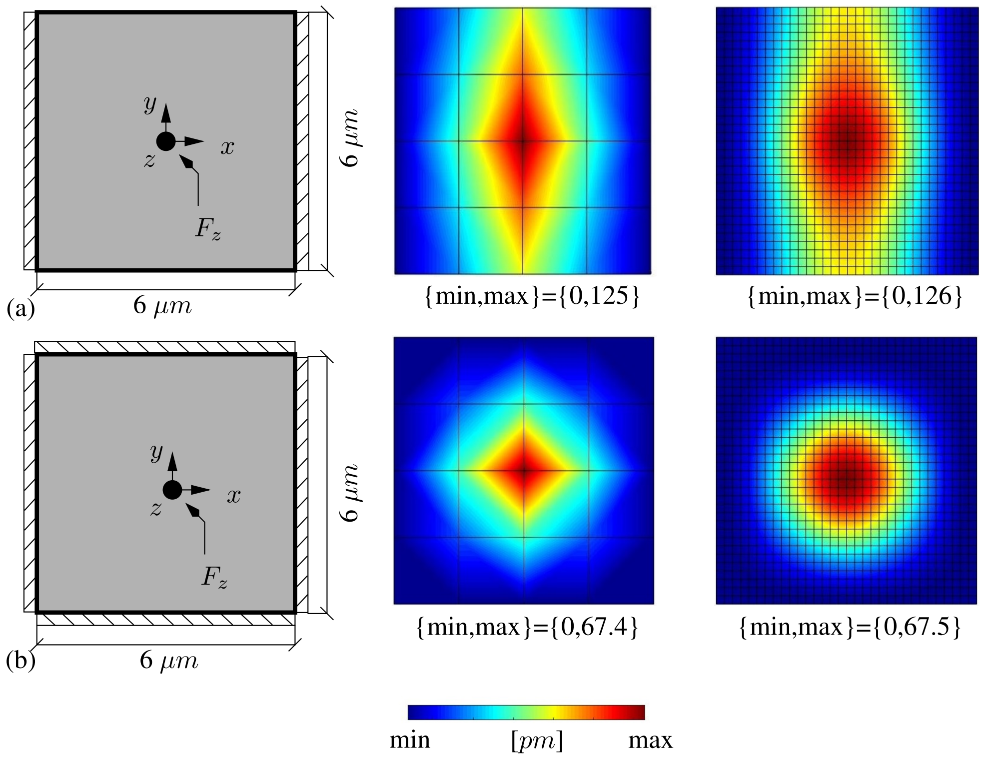

Figure 4.8: Geometry and boundary conditions (left) together with displacement profiles for deflected shapes for mesh refinement tests on a 4x4 and a 32x32 mesh, (a) fixed-fixed, and (b) all sides fixed. F_z=1 mN. Thickness is 1 μm.

4.1.1.3 Applicability to General Quadrilateral Elements

Although not satisfying patch test requirements, it is be advantageous to analyze errors resulting from using general quadrilateral shapes. For this purpose a microstructure with dimensions $20\ \mu m \times 5\ \mu m \times 1\ \mu m$ [157] is selected and an external force of F = 1 mN is applied at midpoint of the plate as in Figure 4.1(a). The problem is

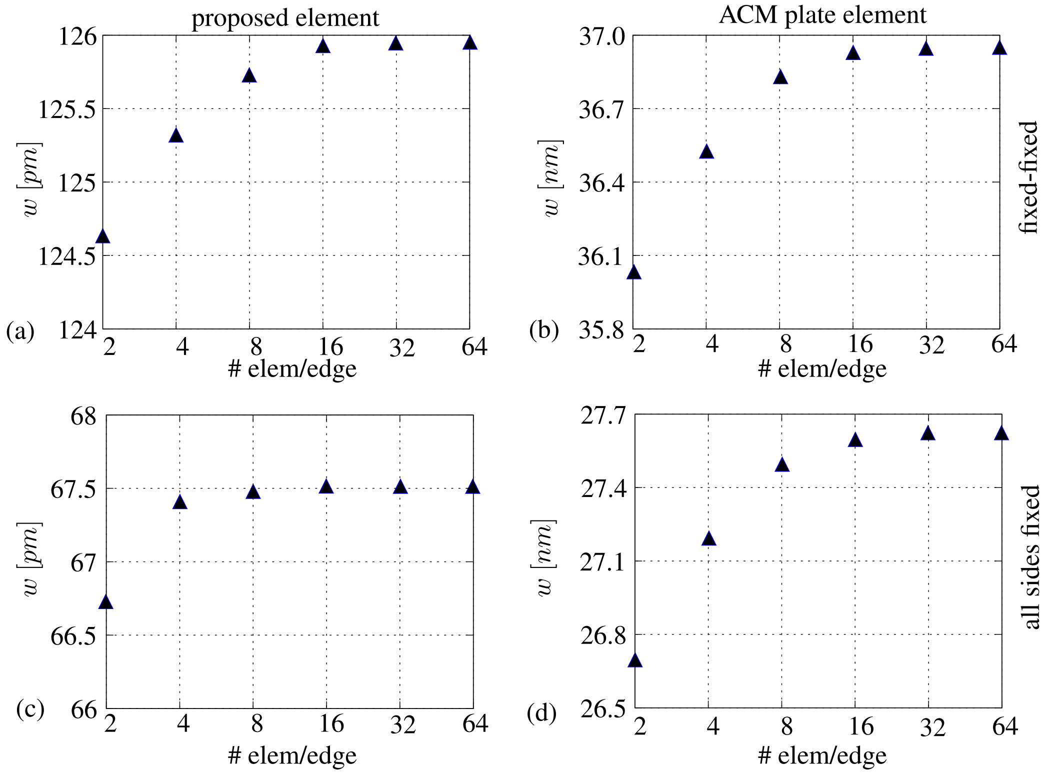

Figure 4.9: Mesh convergence of the microplate element: Loading point deflection versus element per edge for (a) MSGT-based KL solution for the fixed-fixed plate, (b) classical KL solution for the fixed-fixed plate, (c) MSGT-based KL solution for the plate with all sides fixed, (d) classical KL solution for the plate with all sides fixed.

solved for various meshes as given in Figure 4.10. Although the displacement fields look similar for rectangular and quadrilateral meshes as given in Figure 4.10, the displacement results yield a discrepancy of 10.3 $\%$ between those in (a) and (b), 7.1 $\%$ between (b) and (c), 3.4 $\%$ between (a) and (c). Hence, even though it may be possible to confine the errors in a bound with usage of several element types, the general quadrilateral version of the element is not recommended to be used.

4.1.1.4 Square microplate subjected to different boundary conditions

The 20 $\mu m \times 20\ \mu m \times 1\ \mu m$ microplate that is used in previous sections is subjected to a point load is analyzed under various boundary conditions with the classical ACM plate and the proposed higher order microplate element formulations, respectively. Four different boundary conditions are considered, see Figure 4.11: (a) CFCF, (b)

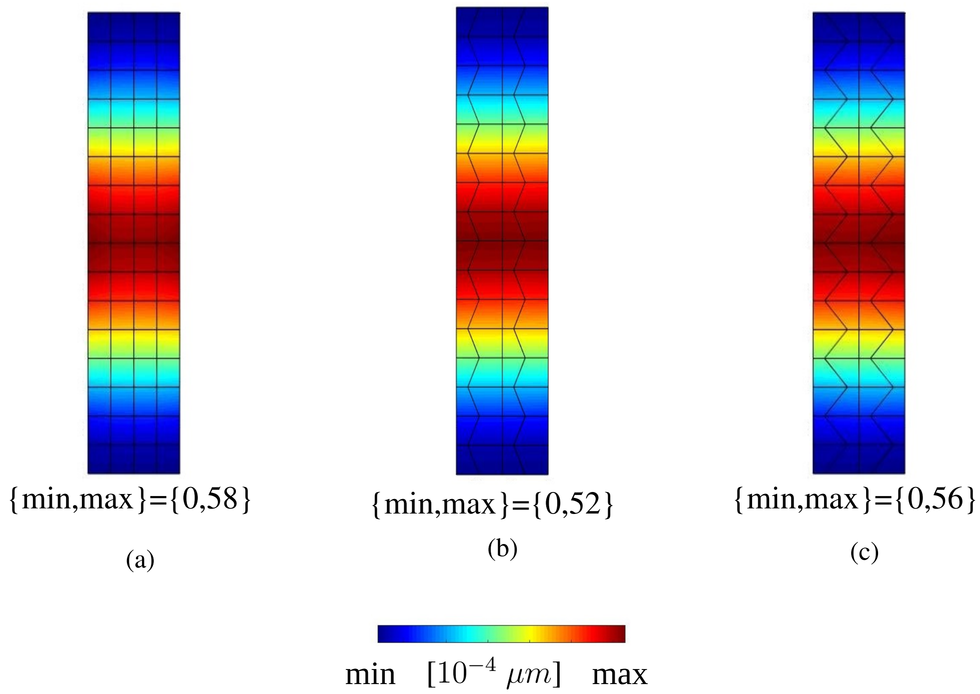

Figure 4.10: Displacement fields for (a) distorted patch (b) regular patch for a mid-point load of 1 N applied upwards. Values are in μm.

CFFF, (c) CCFC and (d) CCFC. The boundary conditions are abbreviated by "C" for clamped ends and by "F" for free ends. In example (a) a centrodial, (b) midpoint of the free edge, (c) centroidal and (d) midpoint of the free edge, respectively. The domain is discretized with 20×20 higher order microplate elements proposed in this contribution. The results obtained from the classical ACM plate element and the higher order microplate element formulations are also visualized in Figure 4.11. From the results obtained, one observes that not only the maximum deflections but also the deformation patterns change significantly by considering the size effect in terms of the modified strain gradient theory.

The higher order stresses in MSGT formulation for CFCF case discussed above are evaluated via substituting displacement field equations of a Kirchhoff plate into equations given in Chapter 2.

Stresses are normally evaluated within elements, and they should be extrapolated to nodes. To this end, relevant strain-displacement matrices are evaluated in Gaussian

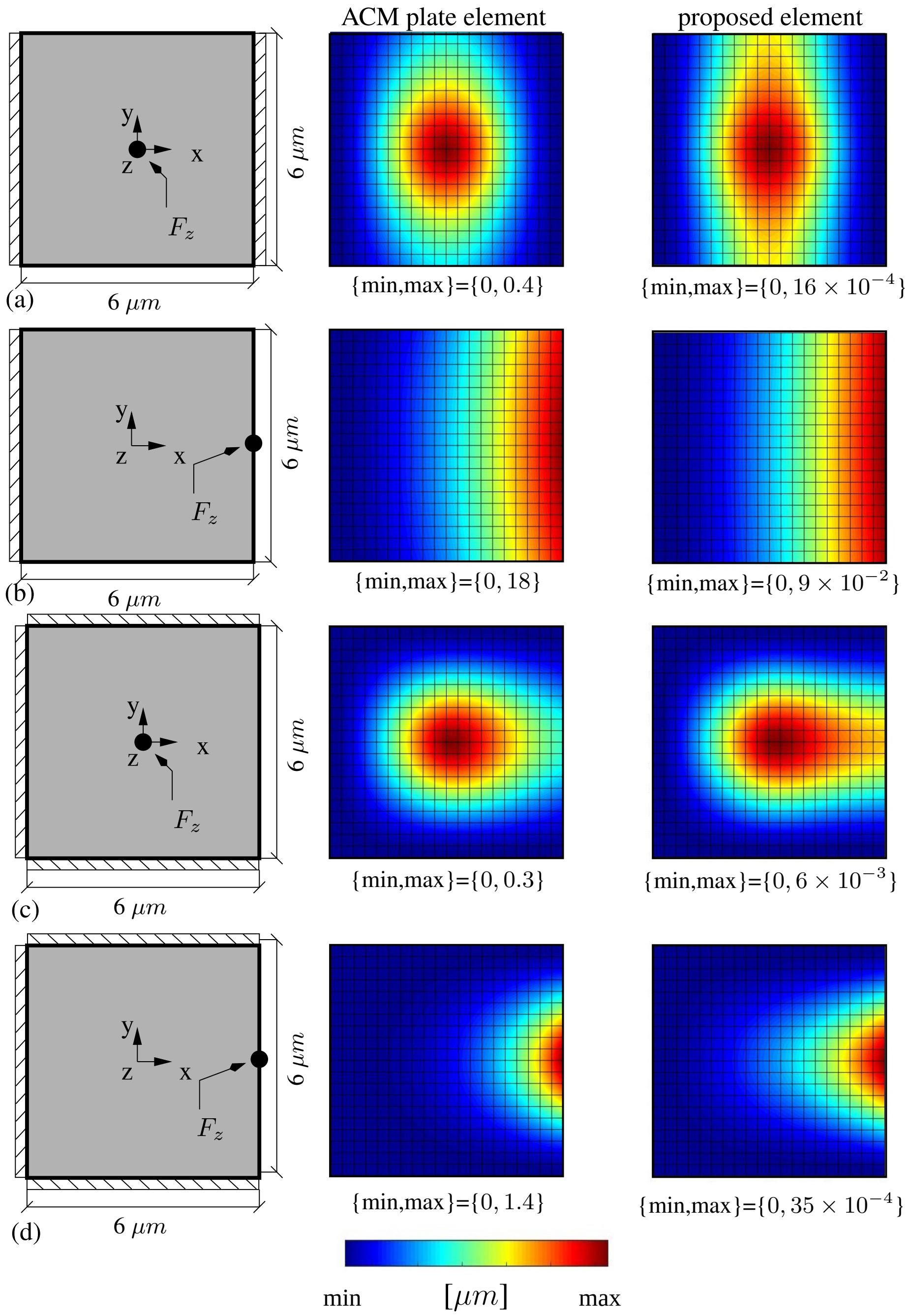

Figure 4.11: Deflected shapes for a microplate with classical theory (second column) and MSGT (third column). Boundary conditions are (a) CFCF, point load applied at midpoint, (b) CFFF, point load applied at endpoint, (c) CCCF, point load applied at midpoint of the plate, (d) CCCF, point load applied at midpoint of the free end. F_z=1 mN. Thickness is 1 μm.

points of each element as, followed by acquiring stress values at these points i.e. A-D given in Figure 4.12. Then, using nodal extrapolation transformation

$$\begin{bmatrix} \sigma'_1 \\ \sigma'_2 \\ \sigma'_3 \\ \sigma'_4 \end{bmatrix} = \begin{bmatrix} 1+\dfrac{\sqrt{3}}{2} & -\dfrac{1}{2} & 1-\dfrac{\sqrt{3}}{2} & -\dfrac{1}{2} \\ -\dfrac{1}{2} & 1+\dfrac{\sqrt{3}}{2} & -\dfrac{1}{2} & 1-\dfrac{\sqrt{3}}{2} \\ 1-\dfrac{\sqrt{3}}{2} & -\dfrac{1}{2} & 1+\dfrac{\sqrt{3}}{2} & -\dfrac{1}{2} \\ -\dfrac{1}{2} & 1-\dfrac{\sqrt{3}}{2} & -\dfrac{1}{2} & 1+\dfrac{\sqrt{3}}{2} \end{bmatrix} \begin{bmatrix} \sigma'_A \\ \sigma'_B \\ \sigma'_C \\ \sigma'_D \end{bmatrix} \tag{4.1}$$

where σ' indicates any stress metric given in Equation (2.23), corresponding stresses at nodes 1-4 of each element are found.

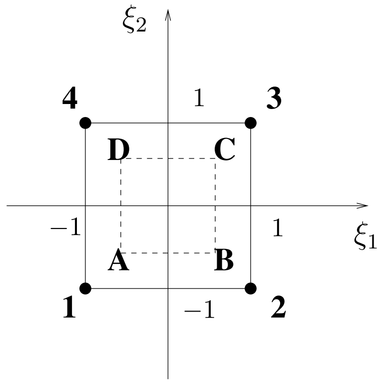

Figure 4.12: Coordinate transformation from (a) original coordinates to (b) mapped coordinates. Node numbers are indicated in bold.

The distribution of them along with classical stress resultants are given in Figures 4.13 and 4.14.

When inserted into Equations B.51-B.57 in B, respective moment resultants (M_{ij}) and higher order moment resultants (Q_{ijk}) can be found. Stress resultants (σ_{ij}) shown in Figure 4.13 should be multiplied with the first power of z and to be integrated over dz per Equations B.51-B.53 in B. Similarly higher order stress resultants (m_{ij}, p_i, and τ_{ijk}) should be integrated over dz (after multiplied with with the zeroth power of z, i.e. 1) per the same equations.

To find the higher order moment resultants in Equations B.54-B.57 per B, higher order stress resultants should be multiplied with the first power in z to be integrated over dz.

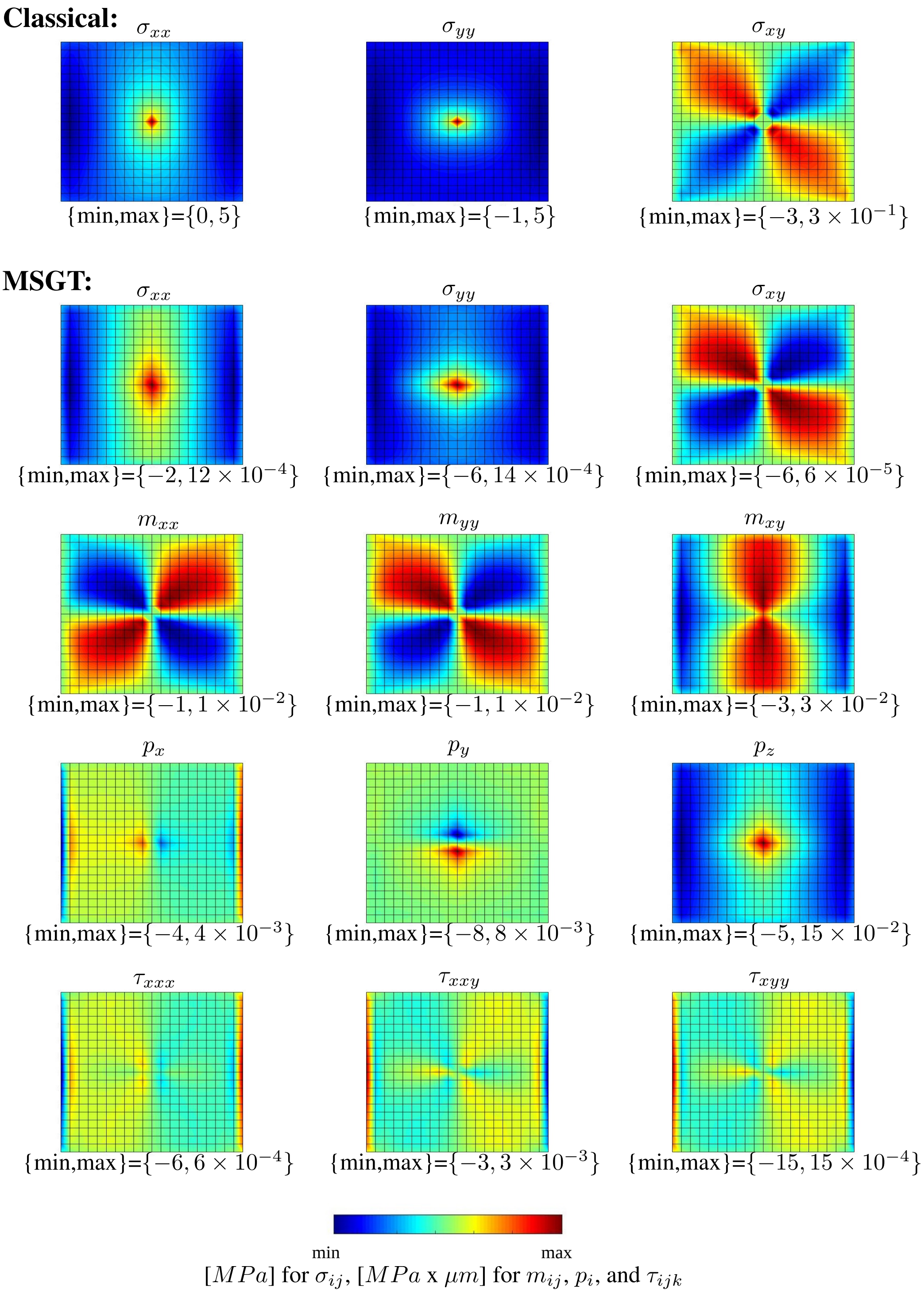

Figure 4.13: Classical and higher order stress metrics per Equations B.51-B.57. It must be noted that m_{zz}=m_{zx}=m_{xz}=m_{yz}=m_{zy}=0, τ_{xxy}=τ_{xyx}=τ_{yxx}, τ_{xyy}=τ_{yyx}=τ_{yxy}.

MSGT (continued):

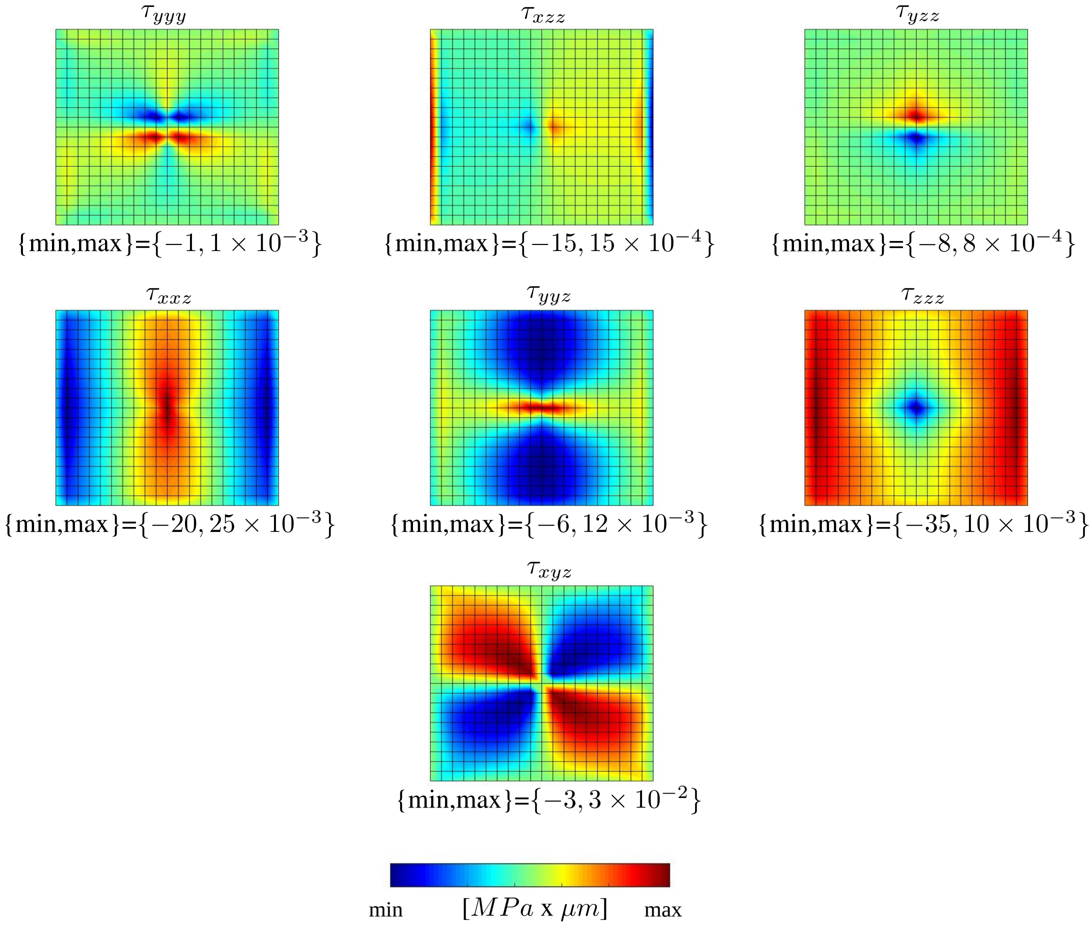

Figure 4.14: Higher order stress metrics (continued) per Equations B.51-B.57. It must be noted that τ_{xzz}=τ_{zxz}=τ_{zzx}, τ_{yzz}=τ_{zyz}=τ_{zzy}, τ_{xxz}=τ_{zxx}=τ_{xzx}, τ_{yyz}=τ_{zyy}=τ_{yzy}, τ_{xyz}=τ_{yxz}=τ_{yzx}=τ_{zxy}=τ_{zyx}.

Therefore M_{ij} terms are given in terms of moment per unit length of the relevant edge of the plate and have units of [force] x [length]/[length], whereas Q_{ijk} are given in terms of moment in units of [force]x[length] in Equations B.51-B.57. Stress resultants given in Figure 4.13, after multiplied by z, and higher order stress resultants, given in Figures 4.13 and 4.14 have units of [force]/[length]. More elaboration on the resultant concepts in plates can be found in references ([160, 161]).

From Figures 4.13 and 4.14 it is seen that, like deflections, higher order stress metrics also have different orders of magnitudes with classical counterparts. Pressure gradient p_z has the biggest magnitude in this case with a distribution profile as the superposition of σ_{xx} and σ_{yy}, and it can be treated as the prevailing axial stress metric. Couple stresses m_{xx} and m_{yy} are the prevailing shear stress metrics in this case. The distributions and magninutes change with microstructure geometry and boundary conditions, and treatment of these are left outside the scope of this study.

4.1.1.5 Benchmark Example: Rectangular Microplates Subjected to Evenly Distributed Load

Three cases solved in Movassagh and Mahmoodi's study using extended Kantarovich method (EKM) [5] are replicated numerically with the proposed higher order microplate elements, see Figure 4.15(a)-(c). The dimensions are in terms of the length scale parameters $l = l_0 = l_1 = l_2$. A distributed load of 1 kN/m^2 is applied similarly for all cases as in the said study. Therein, the material parameters specific to epoxy are used [6], see Table 4.1.

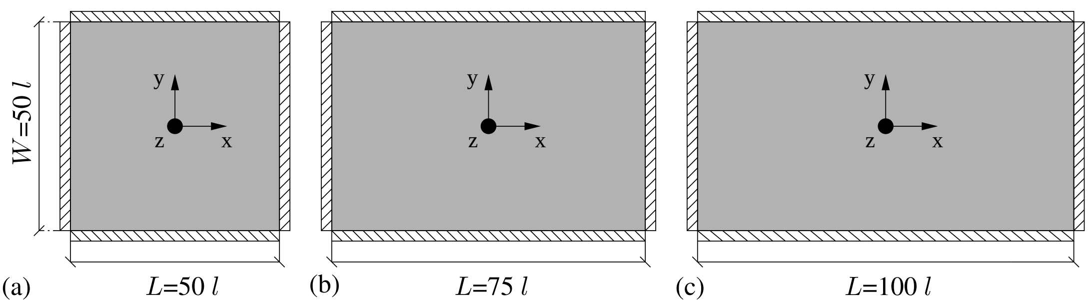

Figure 4.15: Geometry and boundary conditions for the there cases (a)-(c) in [5] replicated numerically with the proposed higher order microplate elements. The dimensions are in terms of the length scale parameters $l = l_0 = l_1 = l_2$, with thickness $h = l$ in all cases. A distributed load of 1 kN/m^2 is applied for all cases as in the said study. Therein, the material parameters specific to epoxy are used [6], see Table 4.1.

The normalized midpoint deflections (w/l) versus number of elements per length results are depicted in Figure 4.16(a)-(c). Both the convergence behavior and the compatibility of the results when compared to the referred cases demonstrate that the proposed higher order microplate elements perform acceptably.

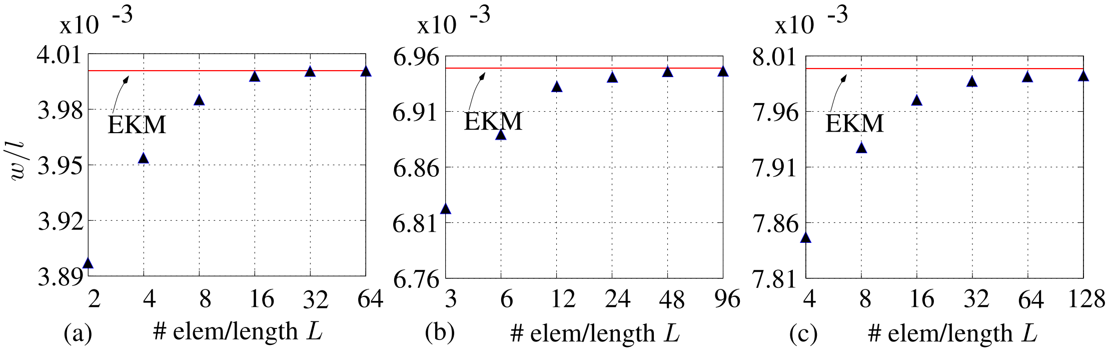

Figure 4.16: Midpoint deflections of the cases in Figure 4.15 versus number of rectangular elements per element length versus results obtained with EKM in [5].

4.1.2 Triangular element (18 DOF)

4.1.2.1 Assessment of element performance

The triangular element is subjected to the same tests and numerical studies as the rectangular elements. The material parameters given in Table 4.1 for triangular elements are used.

4.1.2.1.1 Microplate response to point load

The same test as in Section 4.1.1.2.1 is conducted with triangular elements. The nodal force is applied to the midpoint of the fixed-fixed plate, see Figure 4.17(a). Basically the meshes given in Figure 4.4(b)-(e) is constructed with triangular elements as given in Figure 4.17(b)-(e).

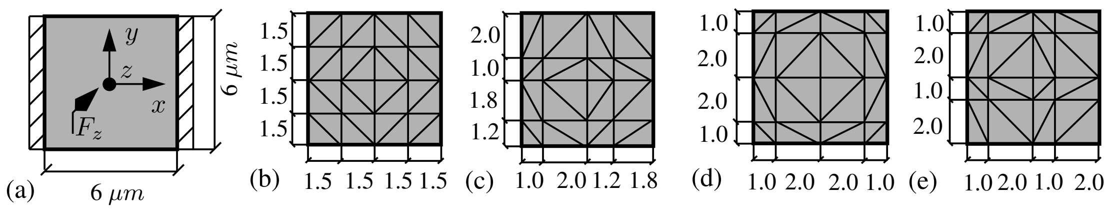

Figure 4.17: (a) Geometry and boundary conditions for square microplate. Thickness is taken as 1 μm and F_z = 1 mN.The problem is solved for (b) regular and (c), (d), (e) irregular mesh discretizations.

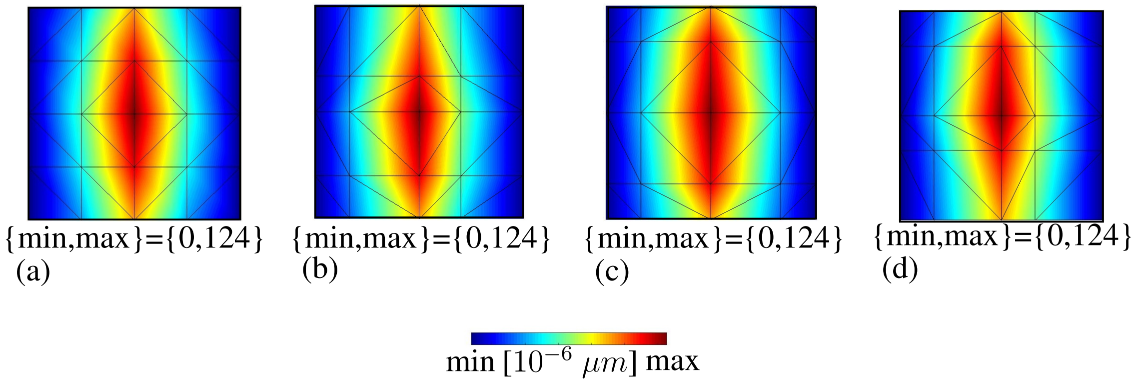

Figure 4.18: Contour plots depicting vertical displacement for the aspect ratio test given in Figure 4.4 for (a) regular mesh and (b, c, d) irregular meshes.

The comparison of deflection profiles with triangular elements (see Figure 4.18(a) and rectangular elements (see Figure 4.8(a)) is given in Figure 4.19.

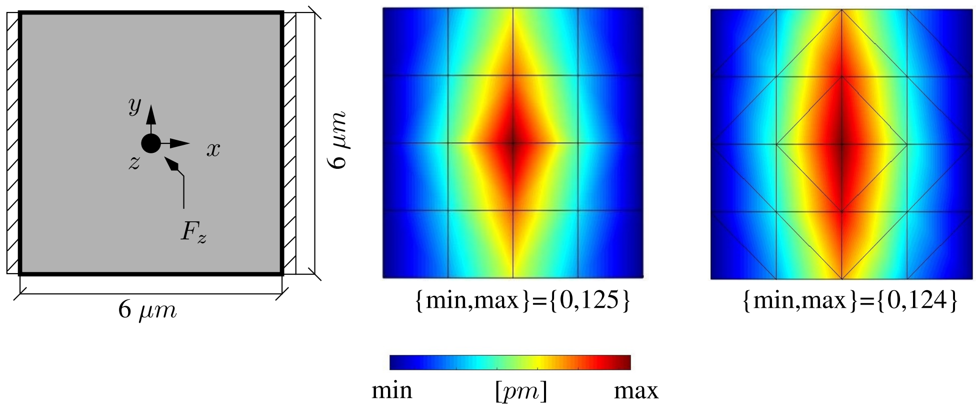

Figure 4.19: Geometry and boundary conditions (left) together with displacement profiles for rectangular elements and triangular elements. F_z=1 mN. Thickness is 1 μm.

4.1.2.1.2 Microplate response to displacement and rotation

The same unit displacements and rotations are applied to the same plate as in Section 4.1.1.2.2 to check the integrity and consistency of the numerics with triangular elements. The meshes and the corresponding displacement fields are given in Figure 4.20. It is seen that the results are in perfect alignment not only when both regular-distorted meshes are analyzed, but also when rectangular-triangular elements are considered, when compared to the results in Figure 4.7.

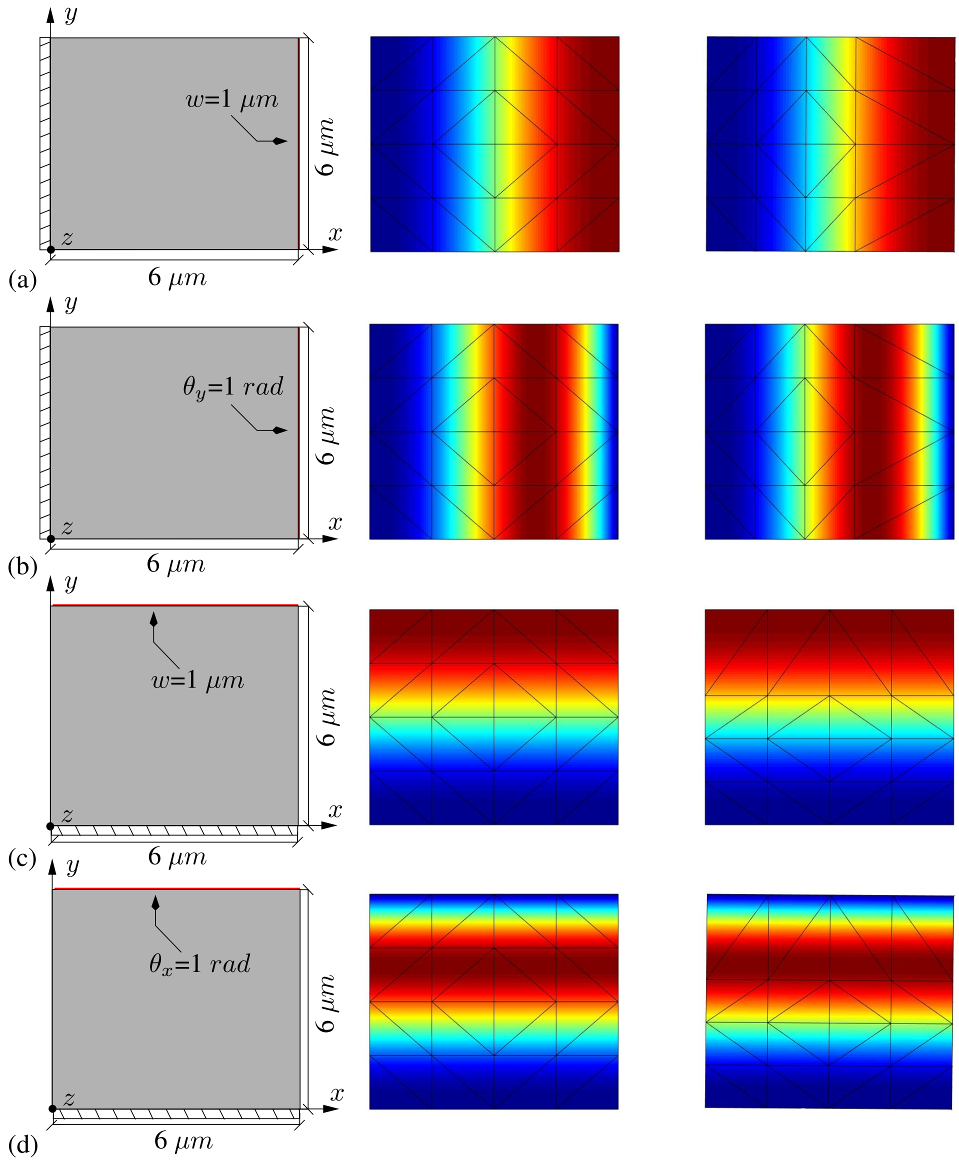

Figure 4.20: Geometry and boundary conditions (left) and corresponding displacement fields for the aspect ratio test considering response to prescribed displacements, for regular mesh (middle) and irregular mesh (right). The thickness of the plates is 1 μm for (a, b, c, d).

4.1.2.1.3 Mesh Refinement and Convergence

The same boundary conditions as in Section 4.1.1.2.3 is applied. That is, 6 $\mu m \times$ 6 $\mu m \times 1$ μm is subjected to a concentrated midpoint load of 1 mN with the boundary conditions are specified as (i) fixed-fixed (two opposite edges clamped, two opposite edges free) and (ii) all sides fixed (all four edges clamped). The midpoint deflections versus element per edge results are depicted in Figure 4.21(a)-(b). The convergence behavior of the proposed element upon mesh-refinement, similar to the proposed rectangular element.

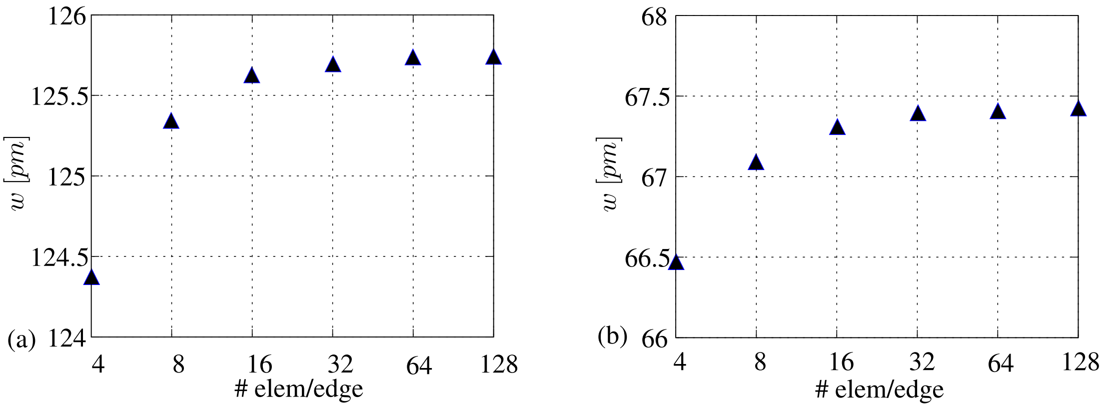

Figure 4.21: Refinement results with triangular elements, i.e. midpoint deflections per number of elements for (a) MSGT, fixed-fixed, (b) MSGT, all sides fixed.

4.1.2.2 Symmetry and Orientation Considerations

Triangular elements can be used in several orientations for modelling orthogonal shapes. In these cases, the node numbering should be counter-clockwise, and preferably in a counter-compatible fashion as given in Figure 4.22.

The regular mesh in Section 4.1.2.1 is changed to be in different orientations and almost the same results and field displacement profiles are obtained as given in Figure 4.23.

4.1.2.3 Applicability to General Triangles

Similar to the analysis performed in Section 4.1.1.3, errors resulting from using general triangular shapes are assessed. The same microstructure in Section 4.1.1.3 with dimensions 20 $\mu m \times 5$ $\mu m \times 1$ μm [157] is selected and an external force of F = 1 mN is applied at midpoint of the plate as in Figure 4.1(a).

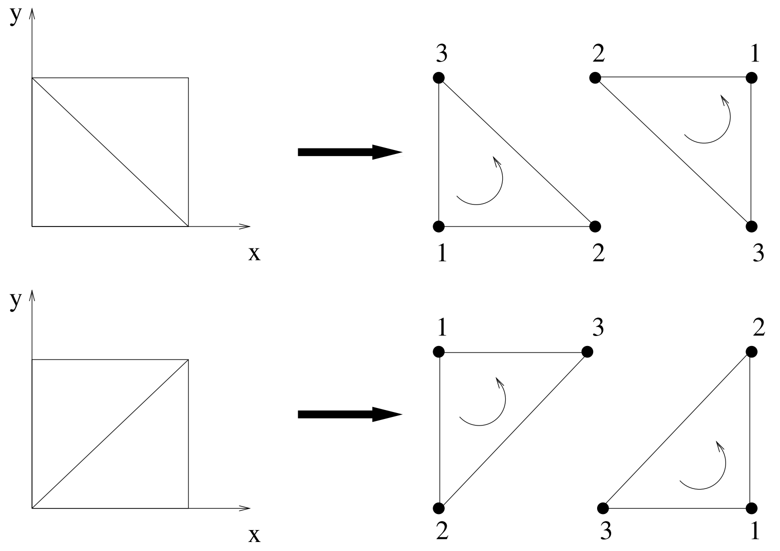

Figure 4.22: Node numbering convention for triangular elements in different orientations.

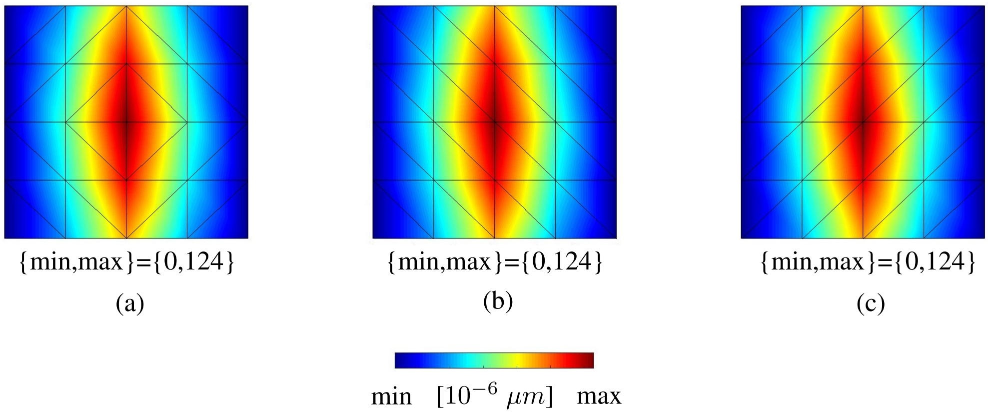

Figure 4.23: Displacement fields for different mesh orientations for triangular elements.

The problem is again solved for various meshes as given in Figure 4.24. Herein, the quadrilateral meshes in Figure 4.10 are divided into two to obtain quadrilateral shapes. The displacement fields look similar for triangular meshes as given in Figure 4.24, but the displacement results yield a discrepancy of 17.2 % between those in (a) and (b), 4.0 % between (b) and (c), 13.8 % between (a) and (c). Since the discrepancies are found to be even larger than the discrepancies found with general quadrilateral elements in Section 4.1.1.3, the general triangular version of the element can not to be used.

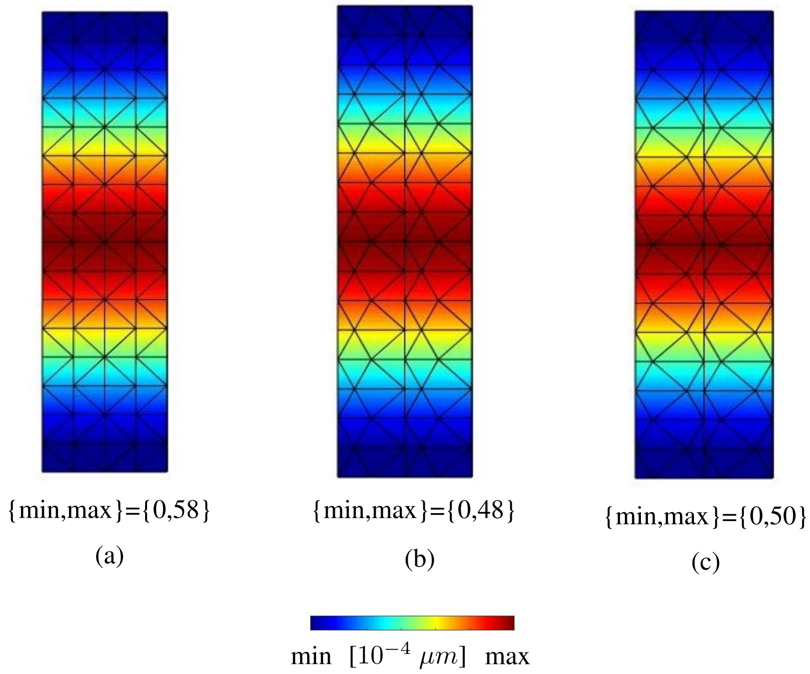

Figure 4.24: Displacement fields for (a) distorted patch (b) regular patch for a mid-point load of 1 N applied upwards. Values are in μm.

4.1.2.4 Benchmark Example: Rectangular Microplates Subjected to Evenly Distributed Load

The same benchmark that is performed in Section 4.1.1.5 [5] is performed with triangular elements constructed in a symmetric fashion as given in Figure 4.23(a). The results are given in Figure 4.25.

Accordingly, the results are similar to those found in Figure 4.16. Similarly, the more the aspect ratio diverges from 1, the gap between EKM and FEA analyses increase.

4.2 Length Scale Parameters for Gold

Various numerical studies are performed in this section to propose length scale parameters for gold. These length scale parameters are used to reveal and predict how gold microstructures behave under load and deformation in comparison with those

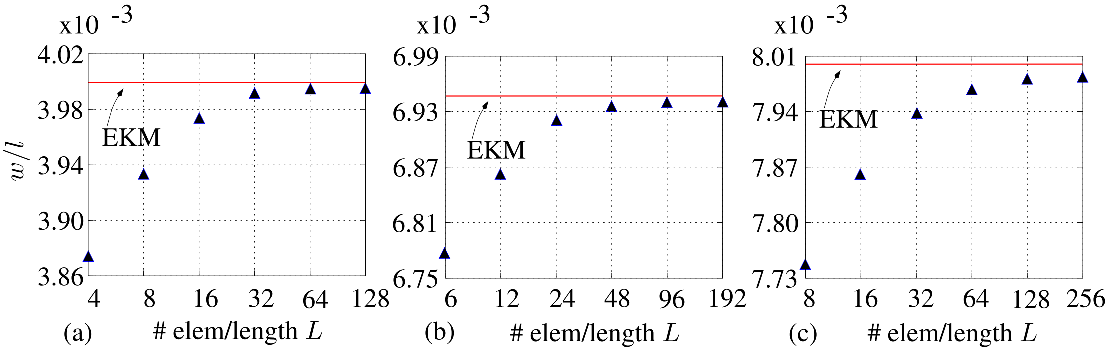

Figure 4.25: Midpoint deflections of the cases in Figure 4.15 versus number of triangular elements per element length versus results obtained with EKM in [5].

predicted by classical theories.

4.2.1 Experiments in the Literature

The codes developed in association with the newly developed plate elements and the beam elements are used to model a number of bending experiments conducted with gold specimens, results of which are published as load-displacement curves [1, 162, 163, 78].

However, all beam bending experiments except for Espinosa's study [1], utilize only one specimen. Each of these may have different material parameters due to different grain sizes, grain orientation, dislocation densities and so on, as a result of different manufacturing techniques and raw materials. Modeling them separately in order to analyze elastic material characteristics may result in misleading results, and hence these are disregarded. Five experiments on each of the two specimens in Espinosa's study [1] are selected to be simulated with the codes.

4.2.1.1 Beam Geometry Assumption with Plate Elements

The specimens in the study of Espinosa et al. [1] are geometrically reduced to be modelled as a beam by ignoring the differences in the cross sections and the middle surface on which the load is applied, for the sake of convenience. The as-is specimens are as given in Figure 4.26(a) whereas the reduced model are given in Figure 4.26(b)-

(c) and Table 4.2.[1].

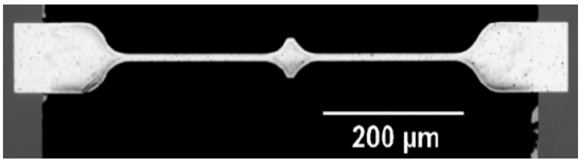

(a)

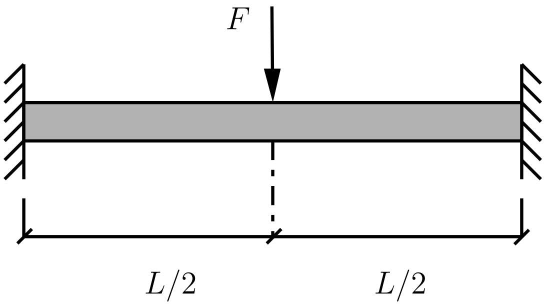

(b)

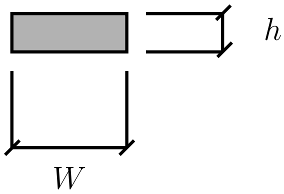

(c)

Figure 4.26: (a) Specimens from Espinosa et al. [1], top view. (b) Idealization for beam geometry, front view. (c) Idealization for beam geometry, side view.

Despite a slight non-linearity it is assumed that initial force-displacement behavior is linear elastic, see Table 4.2. Herein the force-displacement values are graphically acquired from Espinosa's study for the linear elastic regime. Elastic parameters E and ν for Specimens 1 and 2 are assumed to be the same. The length scale parameters l_0, l_1, l_2 are taken as the same, i.e. l.

Table 4.2: Model reduction of specimens per Figure 4.26 [1]. Both are fixed-fixed as given in the relevant figure.

Specimen	W $[\mu m]$	h $[\mu m]$	L $[\mu m]$	F $[\mu m]$	w $[\mu m]$
1	10	0.5	400	0.3	15
2	10	1.0	400	0.3	9

For quantification of elastic modulus E and length scale parameter l, an error parameter Err is defined as the L_2-norm of the residual vector, for the quantification of the best fit at which Err is minimum.

$$Err = (w_1^{sim} - w_1^{\exp})^2 + (w_2^{sim} - w_2^{\exp})^2\,. \tag{4.2}$$

Here w_1^{sim} and w_2^{sim} are the midpoint deflections predicted by higher order theories, $w_1^{\exp}$ and $w_2^{\exp}$ are the actual midpoint deflections from experiments for specimens 1 and 2 respectively. Err is evaluated for different values of E and l, E varying from 20 GPa to 140 GPa as given in Figure 4.27. The minimum and maximum values of E are chosen according to the upper and lower limits reported in literature, while values lower than E=20 GPa are not found realistic.

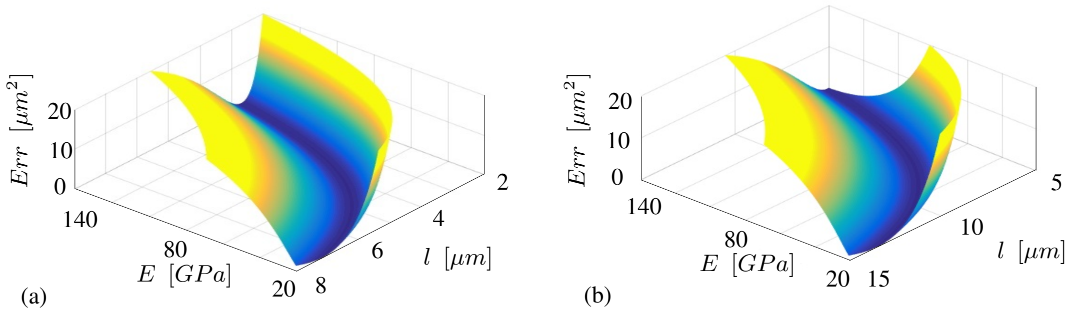

Figure 4.27: Corresponding Err, E, and l values for (a) MSGT and (b) MCST with rectangular plate elements.

It is seen that the error function is minimum along a curve as given in Figure 4.27). It is also found that the error values are monotonically decreasing as E decreases. Hence a realistic evaluation for E and l_0=l_1=l_2 at the minimum error point could not be made. Instead, sets of values for E and l_0=l_1=l_2 are come up with based on minimum error. However, for all reported values, considerable size effect is present.

It is found that for the minimum error for bulk elastic modulus of gold i.e. E=80 GPa, l_0=l_1=l_2=3.71 μm for rectangular elements, see Table 4.1. It is l_0=l_1=l_2=4.77 μm for triangular elements, again see Table 4.1.

4.2.1.2 Beam Geometry Assumption with Beam Elements

The specimens are assumed to be beams as in Section 4.2.1.1 and Table 4.2. The same Err function is defined with the same assumptions. For MSGT, the length scale parameters are found to be l_0=l_1=l_2=3.60 μm, and for MCST, the length scale parameter is found as l_2=6.73 μm, see [157].

4.2.1.3 As-Is Geometry with Plate Elements

The specimens are then modelled as they are with the original dimensions (i.e. as-is plate models) without the beam reduction, as given in the study of Espinosa et al. [1], see Figure 4.26(a).

First, an ANSYS Mechanical model is run in static-structural mode based on the force values in Table 4.2. The deflection values yielded by ANSYS simulations with both models are given in table 4.3. The ANSYS Mechanical model is given in Figure 4.28.

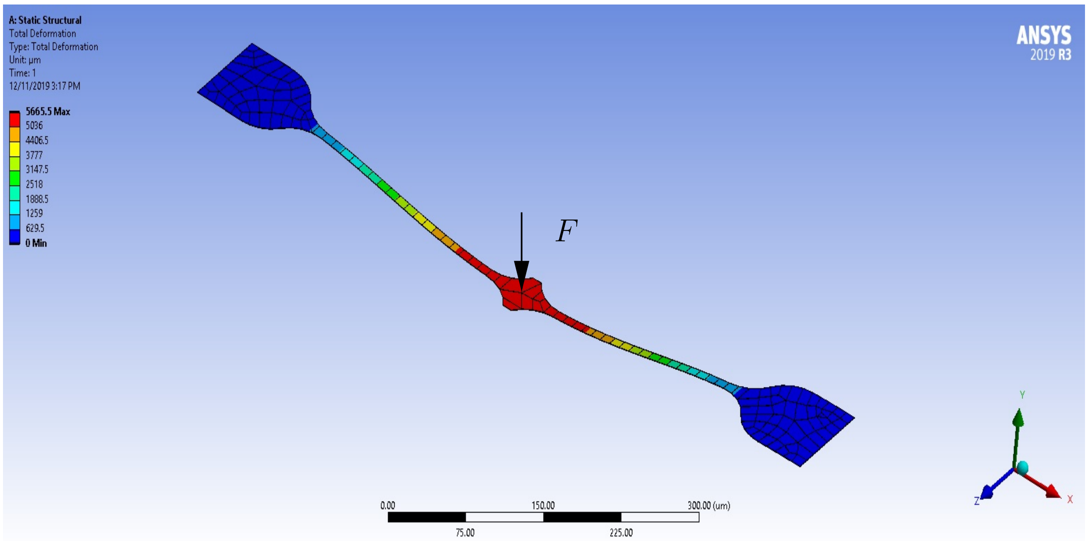

Figure 4.28: ANSYS Mechanical model of the experiments in Espinosa et al. [1]. The force applied is 0.3 mN per Table 4.2. This figure is given for specimen 2, the thickness of which is 1.0 μm.

The as-is plate model that is given in Figure 4.26(a) is then modelled with the code developed with the novel MSGT rectangular and triangular plate elements as given in

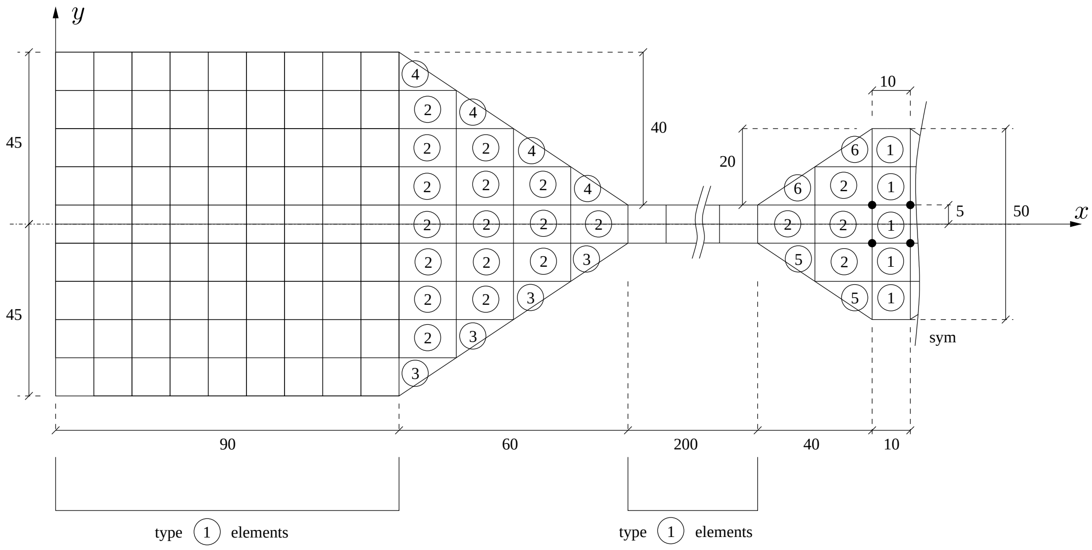

Figure 4.29: Mesh for modelling the specimens in Espinosa et al. [1] with plate elements developed in this study. The circled numbers indicate the type of elements. Type 1 and 2 refer to square and rectangular elements and 3-6 refer to triangular elements with different orientation. The mesh is symmetric with respect to the indicated vertical cut "sym", and hence only the left side is shown. The cumulative force of 0.3 mN is equally applied to the four nodes of the central element indicated by bold dots (0.075 mN to each node).

Table 4.3: Comparison of ANSYS Mechanical models with the plate models with length scale parameters set to zero - i.e. converging to classical models.

Model	Specimen tag no	Max. deflection w $[mm]$ for l_0=l_1=l_2=0	Accuracy $[\%]$ for l_0=l_1=l_2=0
ANSYS	1	5.665	Reference
20 DOF rectangular	1	5.519	97.4%
24 DOF rectangular + 18 DOF triangular	1	5.703	99.3%
18 DOF triangular	1	5.564	98.2%
ANSYS	2	0.708	Reference
20 DOF rectangular	2	0.696	98.3%
24 DOF rectangular + 18 DOF triangular	2	0.711	99.5%
18 DOF triangular	2	0.700	98.9%

Figure 4.29(a). Therein, the mesh involves six types of elements, type 1 and 2 being square and rectangular respectively and 3-6 being triangular with different orientation. The following approaches are taken each with their advantages and drawbacks.

1. Modelling with 20-DOF rectangular elements for types 1-6. The number of elements is 271 and the number of nodes is 331.

2. Modelling with 24-DOF rectangular elements for types 1 and 2, 18-DOF alternative triangular elements for types 3-6. Again, the number of elements is 271 and the number of nodes is 331.

3. Modelling with 18-DOF triangular elements for types 1-6. Therein each rectangular and square element is divided into two triangular elements.

The models discussed above are run with l=0, in order to analyze the convergence to classical model, ultimately to compare with the ANSYS Mechanical model. The deflections found with these are indicated in Table 4.3 along with the accuracy compared with the ANSYS models which are taken as reference, in the rightmost column. Although having several drawbacks as discussed below, all models seem to be sufficiently close to ANSYS Mechanical models when length scale parameters are taken as zero. Hence, all are deemed to be acceptable, especially 24-18 DOF (triangular+rectangular) models.

The comparison of the models in terms of nominal midline displacements are given in Figure 4.30. It is seen that MSGT reveals a stiffer behavior in regions closer to the clamped edges, however converges faster towards the node(s) on which the loads are applied, see also [157].

The 20 DOF rectangular model incorporates a few triangular elements, i.e. types 3-6. Using quadrilateral, yet alone rectangular elements for triangular shapes is almost always undesirable, when mesh skewness is considered. Also when combined with mesh smoothness, which is slightly disrupted with the use of 1.5:1.0 plate elements, these may create inaccuracies. However, since these elements bear no load or are subjected to any boundary condition, and moreover their placement in the global stiffness matrix is not dominant (i.e. they are connecting few elements being in a non-central position), the deviation is confined such that the accuracy is ca. 97-98 %. However, the use of this element for triangular shapes should be made carefully,

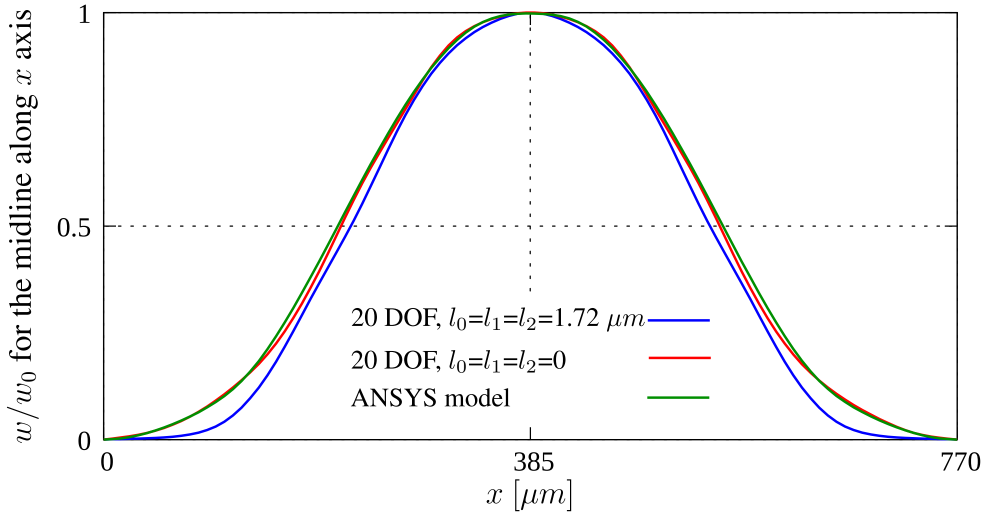

Figure 4.30: Displacement profiles for different models, normalized by dividing to the maximum displacement (of the midnode).

depending on the number of them, location, and boundary conditions imposed on these.

The most accurate model according to Table 4.3 is 24 DOF rectangular + 18 DOF triangular model. This introduces 8 DOF's per node, i.e. highest among all the models, which in turn results in a considerably higher computation time. So these are proposed in fidelity benchmarks, rather than in speed benchmarks.

18 DOF triangular model is also more accurate than 20 DOF model, yet computationally more expensive with 6 DOF's per node and the number of elements of almost twice.

The choise of pure triangular or rectangular+triangular elements in such as case hence depends on several constraints, majorly speed vs fidelity. Also, full rectangular elements can be used as discussed above, if circumstances permit these to some extent.

Based on the approach adopted previously with an error function Err, the length scale parameters are also found with each model, see Table 4.4. All reveal a length scale parameter of around 1.7 μm which is quite different from those found by model reduction, i.e. 3.71 μm for rectangular elements and 4.77 μm for triangular elements. This shows the necessity of using plate elements in an as-is geometry. In fact, as-

Table 4.4: Comparison of ANSYS Mechanical models with the plate models with length scale parameters set to zero - i.e. converging to classical models.

Model	Length scale parameters l_0=l_1=l_2 [μm] for minimum Err
ANSYS	N/A (classical)
20 DOF rectangular	1.72
24 DOF rectangular + 18 DOF triangular	1.73
18 DOF triangular	2.55

suming a non-quadrilateral shape for rectangular elements is even more accurate then model reduction from as-is geometries.

4.2.2 Analysis of Realistic MEMS Switches

Three real MEMS switch structures from Patel and Rebeiz [8] and Stefanini et al. [7] are considered. The geometry and the boundary conditions are depicted in Figure 4.31.

Stefanini et al. [7] discusses an actuation electrode and the corresponding MEMS structure (see Figure 4.31(a)) to transfer the majority of the electrostatic force to the contact force, i.e.

$$F_c = 0.64\ F_e - F_r \tag{4.3}$$

where F_c is the contact force, F_r is the release force, and F_e is the electrostatic force. Therein, F_c = 34.7 μN, F_r = 15.5 μN, and hence the electrostatic force is found as F_e = 77.2 μN. This force is equally distributed to the nodes that are electrostatically actuated, see Figure 4.31(a). The deflection of the plate should be equal to the clearance of 0.3 μm for contact condition. The electrostatic loads are applied to the structures and the deflected shapes, which are obtained from classical and the MSGT-based KL plate theory, are shown in Figure 4.32.

The analyses reveal, as expected, considerably softer response with the classical theory, see Figure 4.32(a) and Figure 4.33(a). The normalized deflection curves

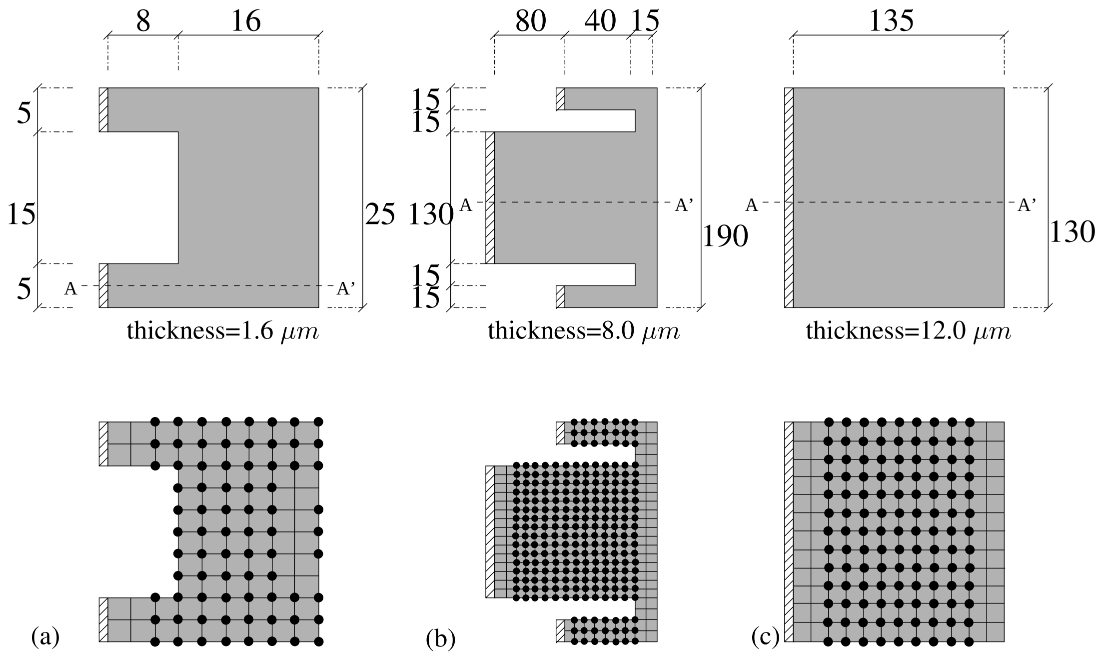

Figure 4.31: Real MEMS structures that are modelled with new plate elements from Stefanini et al. [7] (a) and from Patel and Rebeiz [8] (b and c). The total loads of F_z = 77.2 μN (a) and F_z = 3 mN (b and c) are distributed to the bold circled nodes as given in corresponding meshes. Note that the structure in (c) is the untethered part of the one in (b). All dimensions in μm.

that demonstrates the difference between the deflection profiles are given in Figure 4.34(a). With rectangular elements in MSGT and with the length scale parameters l_0=l_1=l_2=0.69 μm, the contact condition can be achieved, as seen from the same figures. For triangular elements in MSGT, the length scale parameters for the contact condition is l_0=l_1=l_2=1.04 μm.

The study of Patel and Rebeiz [8] focuses on two MEMS switches (see Figure 4.31(b)-(c)) for which the electrostatic force for contact condition is given between 2.5-3.5 mN. It is hence assumed that an average electrostatic force of 3.0 mN is applied. This force is again equally distributed to the relevant nodes, see Figure 4.31(b)-(c). The clearance in the design of these MEMS switches is 0.55 μm. As in the example above, a considerably larger tip deflection deflection is found with the classical theory. The analyses with MSGT-based KL plate yield the required deflection, see Figure 4.32(b)-(c) and Figure 4.33(b)-(c). Similarly, Figure 4.34(b)-(c) indicate the

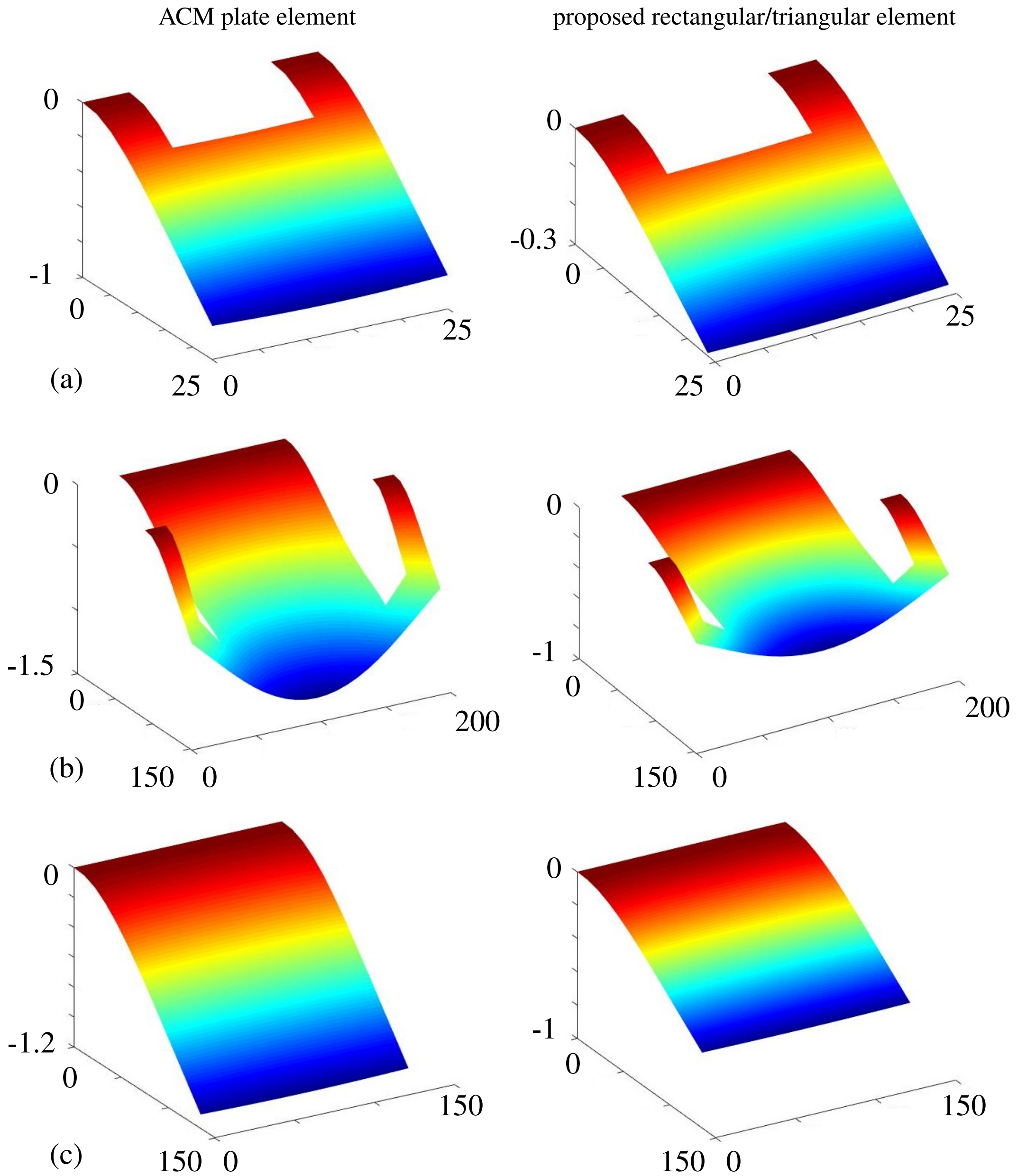

Figure 4.32: The corresponding deflected shapes of the microplates given in Figure 4.31, using classical theory (left column) and MSGT (right column). Structures are from Stefanini et al. [7] (a) and from Patel and Rebeiz [8] (b and c).

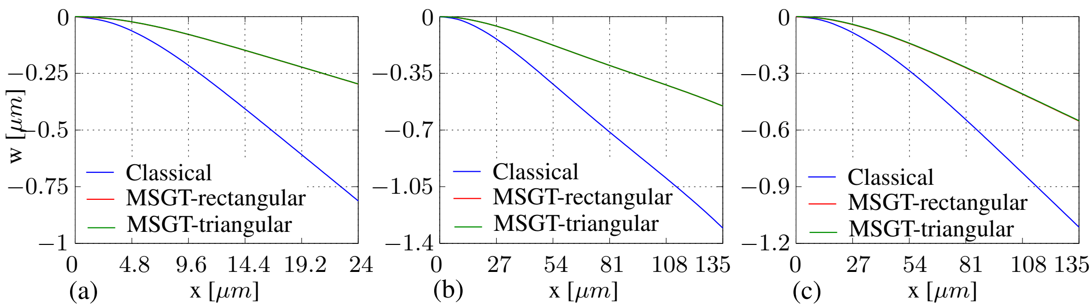

Figure 4.33: Deflection profiles from AA' sections as given in Figure 4.31. Structures are (a) from Stefanini et al. [7] and (b-c) from Patel and Rebeiz [8].

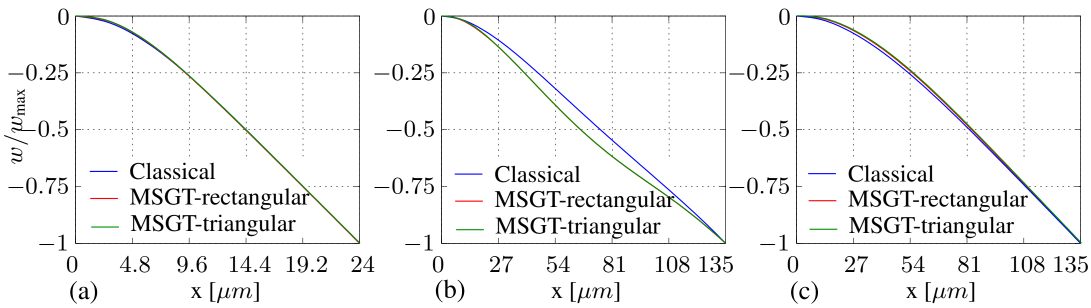

Figure 4.34: Deflection profiles from AA' sections as given in Figure 4.31. Structures are (a) from Stefanini et al. [7], and (b-c) from Patel and Rebeiz [8].

normalized deflection curves that demonstrates the difference between the deflection profiles. The corresponding length scale parameters that are adopted for these MEMS switches are, for rectangular elements, l_0=l_1=l_2=2.87 μm and l_0=l_1=l_2=3.16 μm respectively (see parts (b) and (c) of Figure 4.32, Figure 4.33, and Figure 4.34. They are l_0=l_1=l_2=4.14 μm and l_0=l_1=l_2=4.58 μm respectively for triangular elements.

In these three examples one can observe that higher order theories significantly improve the analysis results. It is also revealed that complex planar structures that couldn't be reduced to beam structures and couldn't be modelled with MSGT previously, examples of which are given in Figure 4.31(a)-(b), can now be designed and analyzed more effectively making use of the new MSGT plate elements.

The MEMS community traditionally use higher elasticity parameters such as Young's modulus μ and shear modulus μ. This choice, for uniform thickness and under pure bending deformations leads to satisfactory results in line with the modified couple stress theory (MCST). This is mainly due to the fact that, MCST, when applied to KL plate theory, leads to the same differential equation as the classical counterpart, where the nonlocal effects are merely reflected to the material parameters. In order to assess the difference between two theories, we depict the normalized tip deflections corresponding to each switch structure in Figure 4.34. The normalized tip deflections of the classical and the MCST-based KL theory will lead to equivalent result. The idea here is to show, how the deflection pattern changes as we switch to the MSGT-based Kirchhoff plate theory from the classical counterpart or the MCST-based KL plate theory. As seen from, Figure 4.34, where pure bending governs the deformation, normalized results overlap. However, for the second geometry, where highly complex local and nonlocal deformations exist due to the relatively complex geometry and boundary conditions, the normalized deflection patterns are quite dissimilar, revealing the necessity for the MSGT-based KL plate theory.

For the case of Stefanini et al. [7] the force and deflection values are assumed to be slightly lower than the contact force at 1.5 times the pull-in voltage and the gap respectively, based on the given data in the reference. For the case of Patel and Rebeiz [8] the force and deflection values are taken from voltage vs. deflected shape indicated in the study. In order to achieve these deflections, the length scale parameters for the MSGT rectangular plate elements are found to be different than found above using the study of Espinosa et al [1], which can be attributed to different manufacturing techniquies, and hence different grain sizes which drastically affect material properties. However the length scale parameters are still in the same order of magnitude of μm level. It is found that l=0.85 μm for the structure in Figure 4.31(a), l=1.25 μm for the structure in Figure 4.31(b), and l=1.50 μm for the structure in Figure 4.31(c). The deflected shapes and the deflection profiles from sections of these are given in Figure 4.32 and 4.33. It is seen that plate elements improve modelling deflections for complex shapes that can not be simulated with beam theories in MSGT.

CHAPTER 5

EXPERIMENTAL STUDIES

Several experimental studies are performed with gold specimens to acquire the length scale parameters in bending. For this purpose, fixed-fixed gold specimens are manufactured in METU MEMS Center with the dimensions as given in Table 5.1. They are subjected to a midpoint load by an atomic force microscope (AFM) as given in Figure 5.1. The (AFM) used is the hpAFM model of Nanomagnetics Instruments® [164]. The AFM tool is AFM Workshop™ ACLA-10 [165].

The application of the bending force is repeated four times for each specimen, then one of them is disregarded and the most consistent three are taken as given in Figure 5.2.

Table 5.1: Specimens on which bending experiments are conducted.

Specimen tag no	Width, b [μm]	Thickness, h [μm]	Length, l [μm]
1	8	0.3	50
2	8	0.3	33
3	8	0.6	50
4	8	0.6	33

As seen from Figure 5.2, nearly all specimens are loaded initially in a linear elastic region. Hence, also considering the orders of magnitudes of the gaps in modern MEMS-NEMS devices, 0-0.3 μm is taken to be the displacement interval for analysis. The following procedure is developed for the interpretation of the experiments. The values and the results mentioned at each step are summarized in Table 5.2.

1. For each specimen, the force-displacement data from the closest three repeti-

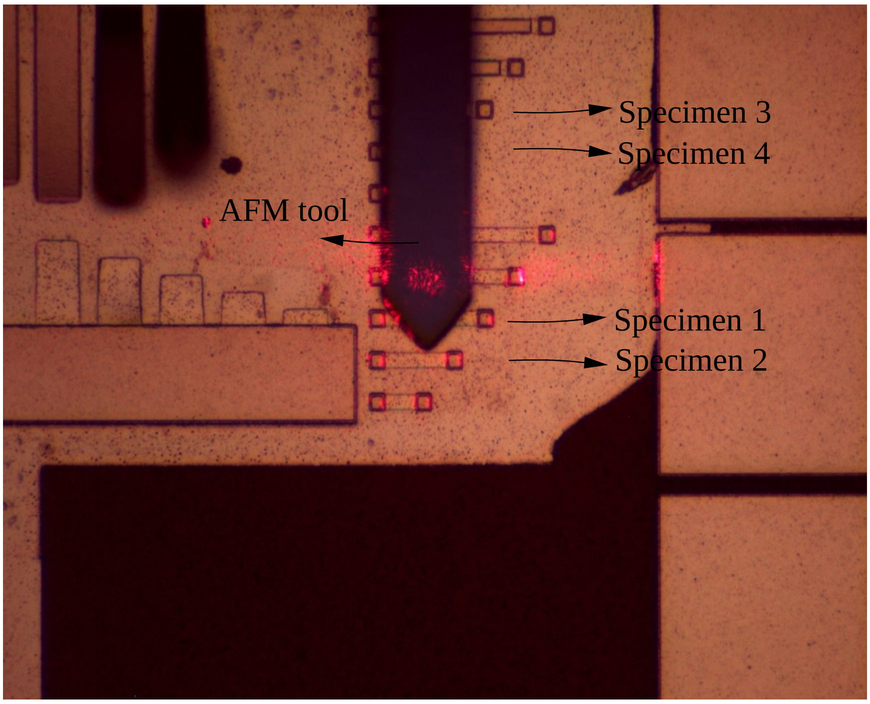

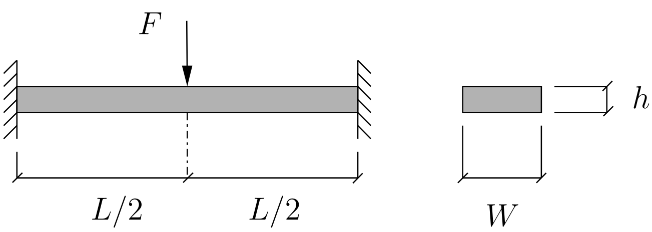

Figure 5.1: Photo of the specimens and the AFM tool from the top and relevant idealizations.

tions are drawn as given in Figure 5.2. Each of these correspond to 25 force-displacement values starting from the onset of the contact of the AFM tool and the specimen. The data from the curves are then trimmed to represent an elastic region with a displacement set to be d_{AFM}=0.3 μm and a corresponding force F different for each repetition and specimen. The F values among repetitions are averaged.

2. In order to assess the assumption that the AFM tool is stiff enough so that the whole displacements measured are for the specimen but does not account for the AFM tool's displacements, the experiments are modelled using a commercial finite element code, ANSYS Mechanical - using transient structural mode.

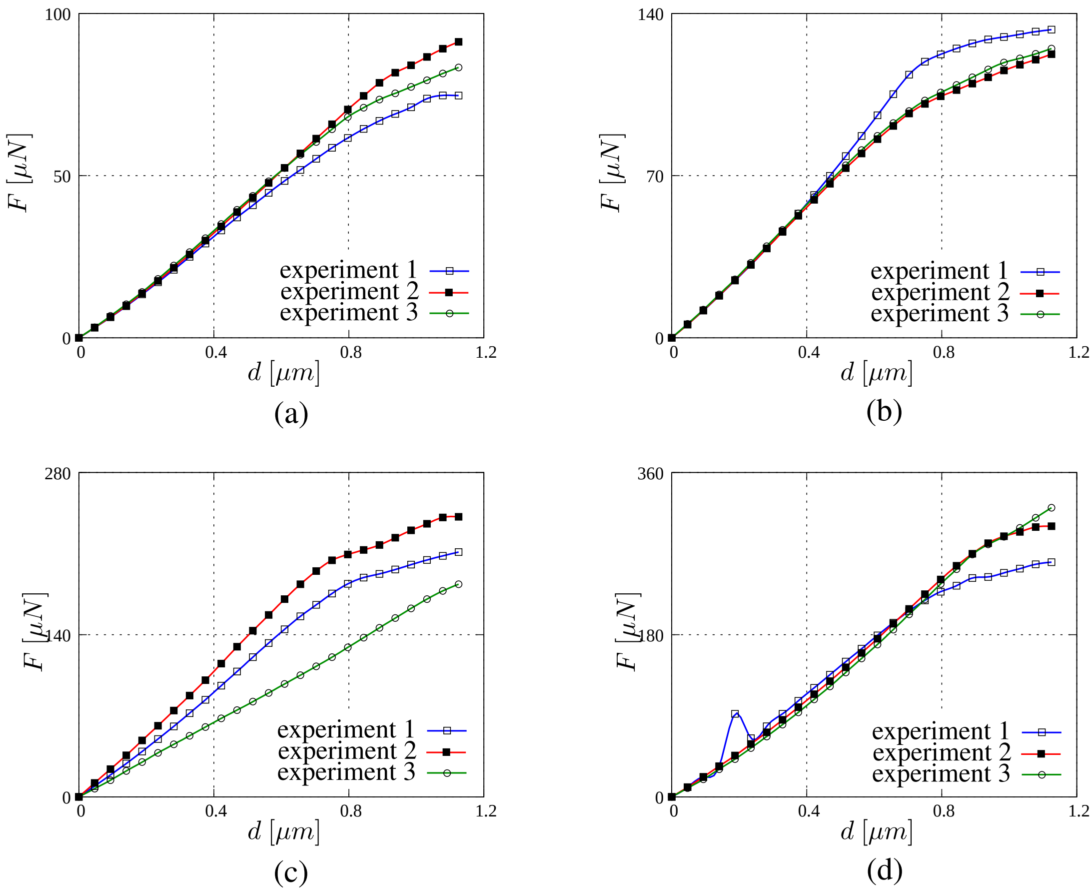

Figure 5.2: Force-displacement data from conducted experiments for (a) specimen 1, (b) specimen 2, (c) specimen 3, (d) specimen 4, per Table 5.1

Therein a constant displacement of d_{AFM}=0.3 μm is applied to the AFM. The end of the AFM tool is in constrained rotation with a downward velocity of 0.1 $\mu m/s$ for each step. The analysis is therefore conducted in 3 steps, with autotime stepping on and a minimum time step of 0.01 seconds and a maximum time step of 0.1 seconds. As expected, these efforts yielded different force results for the specimens, to be designated as $F_{classical}$. Naturally, $F_{classical} < F$ for the same displacement field, since classical theory results in less stiffer beams than higher order theories. The displacement of the midpoint of the specimens are also designated as d_{mid}. The difference between d_{AFM} and d_{mid} indicates the deformation in the AFM tool. Hence, the smaller this difference is, the closer is the experiment to the ideal bending case. See Figure 5.4.

3. F and d_{AFM} values found from the experiments are used to simulate the ex-

periments using a fixed-fixed plate model with the developed higher Kirchoff plate elements as discussed in Section 3.2.2.1.1 and the corresponding code, yielding a distinct length scale parameter for each experiment, represented as l_{ideal}. Therein d_{AFM} is assumed to be equal to d_{mid}, hence an ideal experiment without the deformation of the AFM tool is assumed.

4. F from the experiments and d_{mid} values found from the ANSYS simulations are similarly used to simulate the experiments using a fixed-fixed plate model with the developed higher Kirchoff plate elements as discussed in Section 3.2.2.1.1 and the corresponding code, yielding another distinct length scale parameter, respresented as l_{real}. Therein deformation of the AFM tool according to ANSYS simulations are taken into account.

Table 5.2: Results of the experiments and length scale parameters found for each of the samples with 20-DOF plate element in MSGT.

Specimen tag no	Force - measured, F $[mN]$	AFM displacement d_{AFM} $[\mu m]$	Force - classical, $F_{classical}$ $[mN]$	Midpoint displacement, d_{mid} $[\mu m]$	Length scale parameter - ideal case l_{ideal} $[\mu m]$	Length scale parameter - real case l_{real} $[\mu m]$
1	24.84	3	1.12	0.29	0.72	0.73
2	36.88	3	3.53	0.28	0.48	0.50
3	50.28	3	5.13	0.27	0.69	0.72
4	93.72	3	11.54	0.23	0.49	0.57

With ANSYS simulations, the specimens 1-3 reveal displacements close enough to the ideal case (0.3 μm) with a maximum error of 8%. The assumption of a much stiffer AFM tool can be considered valid there, also given the nominal stiffness value in the datasheet as 58 N/m [165]. For specimen 4 however, the deformation in the AFM tool can be considered to affect this specimen's validity. Yet the length scale parameter revealed turns out to be very close to that of specimen 2, at around l_0=l_1=l_2=0.5 μm. Modelling the experiments with specimens 1 and 3 also reveal a length scale parameter of ca. l_0=l_1=l_2=0.7 μm. Slightly different lengh scale parameters for long specimens (1 and 3) and short specimens (2 and 4) yield that although not captured in the original MSGT, length may have a nonlinear effect on elastic behav-

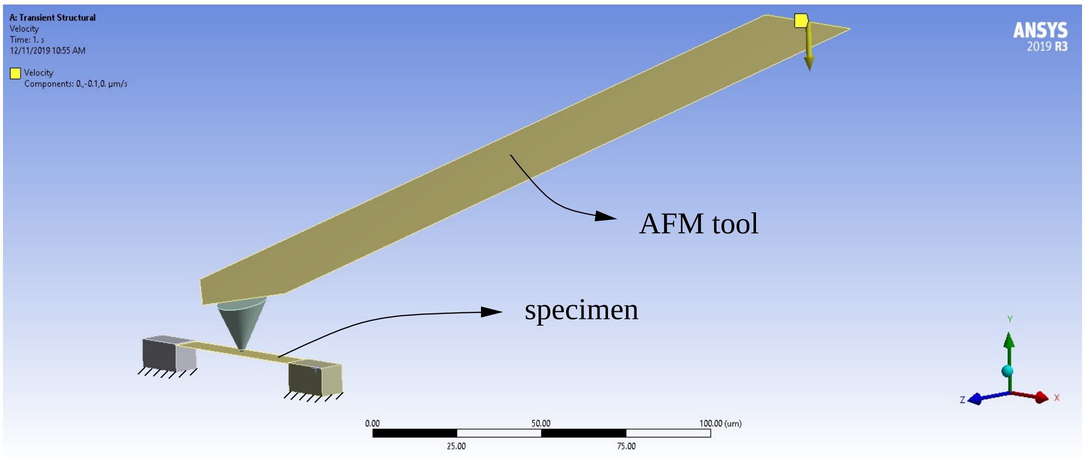

(a)

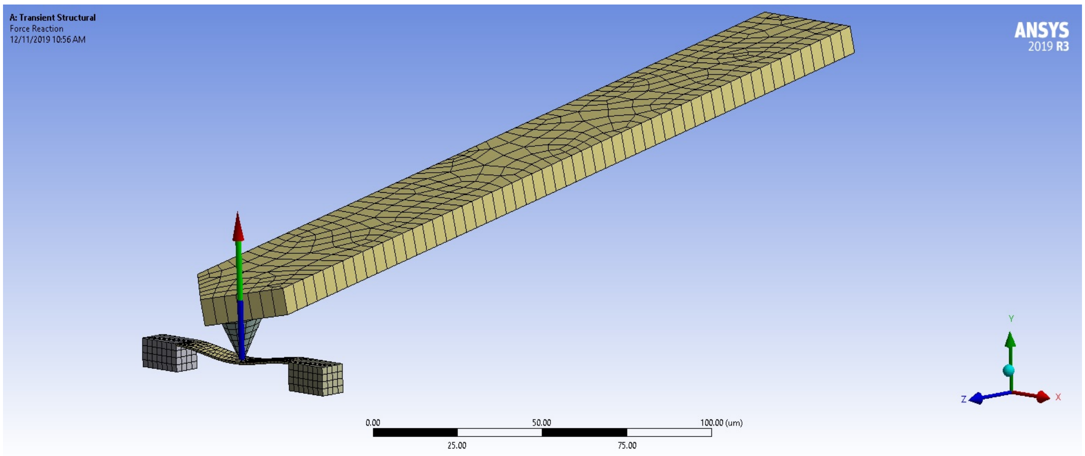

(b)

Figure 5.3: ANSYS simulations of the experiments - boundary conditions and velocity-rotation constraints on the edge shown with a yellow arrow (a), respective mesh and force reaction at the contact point (b).

ior (in some other way than direct proportionality with L^3 as taken in both classical theory and MSGT), like thickness in MSGT.

It can also be said that there is a size effect that can be characterized by a length scale parameter not as high as found previously (around 1.72 μm by modelling the original structure for Espinosa et al. study [1], and around 1-1.5 μm for real MEMS structures [8, 7] with 20-DOF elements), but in such a way that it still needs to be considered. The difference may also result from the manufacturing methods of gold in all these

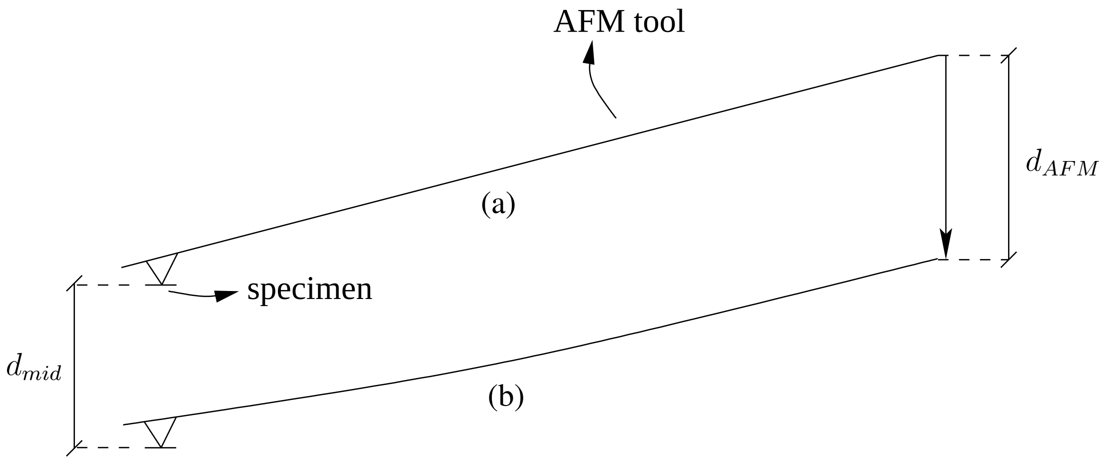

Figure 5.4: Deflections of the AFM tool d_{AFM} and the relevant specimen d_{mid}, at the beginning of the experiments (a) and after the experiments (b).

studies and examples.

The experiments are also modelled using the codes developed with the finite elements discussed in Section 3. Therein, different values found for short and long specimens and the difference between l_{ideal} and l_{real} for Specimen 4 are neutralized by again finding and Err value based on L_2-norm of the residual vector as in Equation 4.2. The final length scale parameters for each type of model is given as in Table 5.3 based on the experiments conducted as a part of this study.

Table 5.3: Length scale parameters found for bending experiments with gold specimens for each type of model.

Model	Theory	Length scale parameter l
6 DOF beam element	MSGT	0.66
20 DOF plate element, rectangular	MSGT	0.67
24 and 18 DOF plate elements, rectangular and triangular	MSGT	0.69
18 DOF plate elements, triangular	MSGT	0.68
4 DOF beam element	MCST	1.24
12 DOF plate element, rectangular	MCST	1.37

CHAPTER 6

CONCLUSIONS

In this Thesis, novel higher order plate bending finite elements are developed for the modified strain gradient theory (MSGT). The formulations for the theoretical background is developed with a variational approach, leading to the development of higher order finite elements. Length scale parameters for gold are also identified.

The said finite elements are developed to analyze micro- and nano-electro-mechanical system (MEMS and NEMS) structures with finite element analysis. This presents a huge leverage in designing and modelling microstructures that can not be geometrically reduced to beam elements. Several numerical problems are addressed and further complementary numerical tests are conducted. It is concluded that the newly developed finite elements can be used with sufficient accuracy, being in compliance with various examples. They also performs better than or at least the same as their classical counterparts in several tests.

It is demonstrated to the MEMS and NEMS community that using the classical plate theory in predicting microplate behavior results in significant errors. These errors further increase with decreasing plate thickness. Due to the lack of accessible experimental data in literature, bending experiments are also conducted that verify and back this argument as a part of this study. A commercial software is used to verify the mechanics of the adopted experimentation technique.

Length scale parameters for gold, a very important material for MEMS structures, are identified via new experiments, existing experiments in the literature, and real structures. This is done for several models using both MSGT and MCST. Therein, existing beam elements and newly developed plate finite elements are made use of.

It is seen in timing benchmarks that analysis with MSGT with the newly developed elements takes upto 14 times longer than classical analyses, ceteris paribus. This is in fact why the Gaussian quadrature method is adopted, which decreases the computational duration ratio upto 6, when compared to the classical theory, again ceteris paribus. It is noted however, most MEMS-NEMS structures can be modelled with very small number of nodes and elements than macrostructures, hence the increase in the computational time can be tolerated with the state of the art CPUs and parallelization techniques. All simulations are carried out on a standard Laptop with Intel I7 processor having 8$\times$ 2.4GHz cores and 8GB Ram, without any parallelization, requiring several minutes computation time for the most demanding simulation. Future work will be devoted to the development of higher DOF rectangular and triangular elements satisfying C^2-continuity requirement.

Discrete techniques and static condensation may also be utilized to come up with conforming higher order plate finite elements applicable to general quadrilaterals. However, it is also worth mentioning that many, if not most, of the MEMS and NEMS microplates can be modelled with only rectangular elements, similar to the real examples modelled and analyzed in this study. Focusing on finding the length scale parameters and divergence from the classical behavior is, to the author's opinion, is a major challenge that should be heavily investigated in the future.

REFERENCES

[1] H. Espinosa, B. Prorok, and M. Fischer, "A methodology for determining mechanical properties of freestanding thin films and MEMS materials," *Journal of the Mechanics and Physics of Solids*, vol. 51, pp. 47–67, jan 2003.

[2] B. Carlsten, P. Anisimov, C. Barnes, Q. Marksteiner, R. Robles, and N. Yampolsky, "High-brightness beam technology development for a future dynamic mesoscale materials science capability," *MPDI Instruments*, vol. 3, 52, 2019.

[3] J. H. Argyris, I. Fried, and D. W. Scharpf, "The tuba family of plate elements for the matrix displacement method," *Aeronautical Journal*, vol. 72, pp. 701–709, 1968.

[4] P. G. Ciarlet and P. A. Raviart, "General lagrange and hermite interpolation in $\mathbb{R}^n$ with applications to finite element methods," *Archive for Rational Mechanics and Analysis*, vol. 46, pp. 177–199, 1972.

[5] A. A. Movassagh and M. Mahmoodi, "A micro-scale modeling of kirchhoff plate based on modified strain-gradient elasticity theory," *European Journal of Mechanics - A/Solids*, vol. 40, pp. 50–59, jul 2013.

[6] D. Lam, F. Yang, A. Chong, J. Wang, and P. Tong, "Experiments and theory in strain gradient elasticity," *Journal of the Mechanics and Physics of Solids*, vol. 51, pp. 1477–1508, aug 2003.

[7] R. Stefanini, M. Chatras, P. Blondy, and G. M. Rebeiz, "Miniature MEMS switches for RF applications," *Journal of Microelectromechanical Systems*, vol. 20, pp. 1324–1335, dec 2011.

[8] C. Patel and G. Rebeiz, "Rf mems metal-contact switches with mn-contact and restoring forces and low process sensitivity," *IEEE Transactions on Microwave Theory and Techniques*, vol. 59, pp. 1230–1237, 2011.

[9] S. Alper and T. Akin, “A single-crystal silicon symmetrical and decoupled MEMS gyroscope on an insulating substrate,” *Journal of Microelectromechanical Systems*, vol. 14, pp. 707–717, aug 2005.

[10] C. Berry, N. Wang, M. Hashemi, M. Unlu, , and M. Jarrahi, “Significant performance enhancement in photoconductive terahertz optoelectronics by incorporating plasmonic contact electrodes,” *Nature Communications*, vol. 4, p. 1622, 2013.

[11] M. Bourne, *A Consumer's Guide to MEMS and Nanotechnology, 1st edition*. 2007.

[12] M. Kangul, E. Aydin, F. Gokce, O. Zorlu, and H. Kulah, “Analysis and elimination of the capacitive feedthrough current on electrostatically actuated and sensed resonance-based MEMS sensors,” *Journal of Microelectromechanical Systems*, vol. 26, pp. 1272–1278, dec 2017.

[13] H. Kulah and K. Najafi, “Energy scavenging from low-frequency vibrations by using frequency up-conversion for wireless sensor applications,” *IEEE Sensors J.*, vol. 8, no. 3, pp. 261–268, 2008.

[14] K. Lam, E. Johnson, M. Chiao, and L. Lin, “A MEMS photosynthetic electrochemical cell powered by subcellular plant photosystems,” *Journal of Microelectromechanical Systems*, vol. 15, pp. 1243–1250, oct 2006.

[15] L. Luo, “Attitude angular measurement system based on MEMS accelerometer,” *7th International Symposium on Advanced Optical Manufacturing and Testing Technologies: Large Mirrors and Telescopes*, sep 2014.

[16] P. Mitcheson, E. Yeatman, G. Rao, A. Holmes, and T. Green, “Energy harvesting from human and machine motion for wireless electronic devices,” *Proceedings of the IEEE*, vol. 96, pp. 1457–1486, sep 2008.

[17] J. Palesko and D. Bernstein, *Modeling MEMS and NEMS*. Chapman and Hall CRC, 2003.

[18] G. M. Rebeiz, *RF MEMS*. Wiley-Blackwell, 2003.

[19] A. Sinding, A. Parent, I. E. Ocak, W. U. Syed, A. N. Chatterjee, C. Welham, S. Liu, J. Yan, S. Breit, and H.-K. e. a. Chang, “A novel squeezed-film damping model for mems comb structures,” *2017 19th International Conference on Solid-State Sensors, Actuators and Microsystems (TRANSDUCERS)*, 2017.

[20] M. Unlu, M. Hashemi, C. W. Berry, S. Li, S.-H. Yang, and M. Jarrahi, “Switchable scattering meta-surfaces for broadband terahertz modulation,” *Nature Scientific Reports*, vol. 4, p. 5708, 2014.

[21] Y. Wang and J. Bokor, “Ultra-high-resolution monolithic thermal bubble inkjet print head,” *J. Micro/Nanolith. MEMS MOEMS*, vol. 6, p. 043009, 2007.

[22] N. Fleck, G. Muller, M. Ashby, and J. Hutchinson, “Strain gradient plasticity: Theory and experiment,” *Acta Metallurgica et Materialia*, vol. 42, pp. 475–487, feb 1994.

[23] Q. Ma and D. R. Clarke, “Size dependent hardness of silver single crystals,” *Journal of Materials Research*, vol. 10, pp. 853–863, apr 1995.

[24] K. W. McElhaney, J. J. Vlassak, and W. D. Nix, “Determination of indenter tip geometry and indentation contact area for depth-sensing indentation experiments,” *Journal of Materials Research*, vol. 13, pp. 1300–1306, may 1998.

[25] W. Poole, M. Ashby, and N. Fleck, “Micro-hardness of annealed and work-hardened copper polycrystals,” *Scripta Materialia*, vol. 34, pp. 559–564, feb 1996.

[26] N. Stelmashenko, M. Walls, L. Brown, and Y. Milman, “Microindentations on w and mo oriented single crystals: An STM study,” *Acta Metallurgica et Materialia*, vol. 41, pp. 2855–2865, oct 1993.

[27] J. Stölken and A. Evans, “A microbend test method for measuring the plasticity length scale,” *Acta Materialia*, vol. 46, pp. 5109–5115, sep 1998.

[28] D. C. Miller, C. F. Herrmann, H. J. Maier, S. M. George, C. R. Stoldt, and K. Gall, “Thermo-mechanical evolution of multilayer thin films: Part i. mechanical behavior of au/cr/si microcantilevers,” *Thin Solid Films*, vol. 515, pp. 3208–3223, feb 2007.

[29] F. Richter, "Mechanical properties of solid bulk materials and thin films," *A Lecture Series for the Teaching Programme of the International Research Training Group "Materials and Concepts for Advanced Interconnects"*, 2010.

[30] E. Salas, R. J. Riobóo, C. Prieto, and A. Every, "Surface acoustic wave velocity of gold films deposited on silicon substrates at different temperatures," *J. Appl. Phys.*, vol. 110, p. 023503, 2011.

[31] E. Hall, "The deformation and ageing of mild steel: Iii discussion of results," *Proceedings of the Physical Society. Section B*, vol. 64 (9), p. 747–753, 1951.

[32] N. Petch, "The cleavage strength of polycrystals," *J. Iron Steel Inst.*, vol. 174, pp. 25–28, 1953.

[33] I. Chasiotis, C. Bateson, K. Timpano, A. McCarty, N. Barker, and J. Stanec, "Strain rate effects on the mechanical behavior of nanocrystalline au films," *Thin Solid Films*, vol. 515(6), pp. 3183–3189, 2007.

[34] K. Gall, M. Dunn, Y.Zhang, and B. Corff, "Thermal cycling response of layered gold/polysilicon mems structures," *Mechanics of Materials*, vol. 36, pp. 45–55, 2006.

[35] K. Kim, J. Song, E. Chung, J. Park, and S. Hong, "Relationship between mechanical properties and microstructure of ultra-fine gold bonding wires," *Mechanics of Materials*, vol. 38, pp. 119–127, 2006.

[36] J. Mulloni, V. Giacomozzi, and B. Margesin, "Controlling stress and stress gradient during the release process in gold suspended micro-structures," *Sensors Actuators A: Physical*, vol. 162, pp. 93–99, 2010.

[37] G. Schmid and B. Corain, "Nanoparticulated gold: Syntheses, structures, electronics, and reactivities," *European Journal of Inorganic Chemistry*, vol. 17, p. 3081–3098, 2003.

[38] A. Soma and M. Saleem, "Modeling and experimental verification of thermally induced residual stress in rf-mems," *J. Micromech. Microeng.*, vol. 25, p. 055007, 2015.

[39] C. Thompson, “Structure evolution during processing of polycrystalline films,” *Annu. Rev. Mater. Sci.*, vol. 30, pp. 159–190, 2000.

[40] I. Chasiotis and W. G. Knauss, “A new microtensile tester for the study of MEMS materials with the aid of atomic force microscopy,” *Experimental Mechanics*, vol. 42, pp. 51–57, mar 2002.

[41] D. Gianola and W. Sharpe, “Techniques for testing thin films in tensions,” *Experimental Techniques*, vol. 28, pp. 23–27, sep 2004.

[42] J. Greer and W. Nix, “Size dependence of mechanical properties of gold at the sub-micron scale,” *Appl. Phys. A*, vol. 80, pp. 1625–1629, mar 2005.

[43] J. R. Greer, W. C. Oliver, and W. D. Nix, “Size dependence of mechanical properties of gold at the micron scale in the absence of strain gradients,” *Acta Materialia*, vol. 53, pp. 1821–1830, apr 2005.

[44] S. Gudlavalleti, *Mechanical Testing of Solid Materials at the Micro-Scale*. PhD thesis, Massachusetts Institute of Technology, 2001.

[45] L. Wang, C. Liang, and B. Prorok, “A comparison of testing methods in assessing the elastic properties of sputter-deposited gold films,” *Thin Solid Films*, vol. 515, pp. 7911–7918, jul 2007.

[46] T. P. Weihs, S. Hong, J. C. Bravman, and W. D. Nix, “Mechanical deflection of cantilever microbeams: A new technique for testing the mechanical properties of thin films,” *Journal of Materials Research*, vol. 3, pp. 931–942, oct 1988.

[47] J. Biener, A. Hodge, J. Hayes, C. Volkert, L. Zepeda-Ruiz, A. Hamza, and F. Abraham, “Size effects on the mechanical behavior of nanoporous au,” *Nano Letters*, vol. 6, pp. 2379–2382, 2006.

[48] G. de Pasquale, A. Soma, and A. Ballestra, “Mechanical fatigue on gold mems devices: Experimental results,” *Symposium on Design, Test, Integration and Packaging of MEMS/MOEMS*, vol. 1, 2008.

[49] D. Faurie, P.-O. Renault, E. L. Bourhis, and P. Goudeau, “Study of texture effect on elastic properties of au thin films by x-ray diffraction and in situ tensile testing,” *Acta Materialia*, vol. 54, p. 4503–4513, 2006.

[50] D. Faurie, P. Djemia, E. L. Bourhis, P.-O. Renault, Y. Roussigne, S. Cherif, R. Brenner, O. Castelnau, G. Patriarche, and P. Goudeau, "Elastic anisotropy of polycrystalline au films: Modeling and respective contributions of x-ray diffraction, nanoindentation and brillouin light scattering," *Acta Materialia*, vol. 58, p. 4998–5008, 2010.

[51] C. Freeze, X. Ji, A. Kingon, and D. Irving, "Impact of joule heating, roughness, and contaminants on the relative hardness of polycrystalline gold," *Journal of Physics: Condensed Matter*, vol. 25, p. 472202, 2013.

[52] Y.-H. Huh, D.-I. Kim, D.-J. Kim, H.-M. Lee, and J.-H. Park, "Dependency of micromechanical properties of gold thin films on grain size," *Engineering Against Fracture*, vol. 1, pp. 339–346, 2009.

[53] S. Sun, X. Chen, N. Badwe, and K. Sieradzki, "Potential-dependent dynamic fracture of nanoporous gold," *Nature Materials*, vol. 14, p. 894–898, 2015.

[54] K. Wang and J. Weissmüller, "Composites of nanoporous gold and polymer," *Advanced Materials*, vol. 25, p. 1280–1284, 2013.

[55] W. Voigt, "Theoretische studien über die elasticitätsverhältnisse der krystalle. i. ableitung der grundgleichungen aus der annahme mit polarität begabter moleküle," *Abhandlungen der Mathematischen Classe der Königlichen Gesellschaft der Wissenschaften zu Göttingen*, vol. 24, pp. 3–52, 1887.

[56] H. Askes and E. C. Aifantis, "Gradient elasticity in statics and dynamics: An overview of formulations, length scale identification procedures, finite element implementations and new results," *International Journal of Solids and Structures*, vol. 48, pp. 1962–1990, jun 2011.

[57] R. D. Mindlin and H. F. Tiersten, "Effects of couple-stresses in linear elasticity," *Archive for Rational Mechanics and Analysis*, vol. 11, no. 1, pp. 415–448, 1962.

[58] G. Grioli, "Elasticità asimmetrica," *Annali di Matematica Pura ed Applicata, Series 4*, vol. 50, pp. 389–417, dec 1960.

[59] E. Aero and E. Kuvshinskii, "Fundamental equations of the theory of elastic media with rotationally interacting particles," *Fizika Tverdogo Tela*, vol. 2, pp. 1399–1409, 1960.

[60] R. Toupin, "Elastic materials with couple stress," *Arch. Rational Mech. Anal*, vol. 11, pp. 385–414, 1962.

[61] A. Eringen, "Theory of micropolar continua," *Proceedings of the ninth midwestern mechanics conference, Wisconsin*, 1965.

[62] R. Mindlin, "Second gradient of strain and surface-tension in linear elasticity," *International Journal of Solids and Structures*, vol. 1, pp. 417–438, nov 1965.

[63] W. Nowacki, *Theory of Micropolar Elasticity*. Springer Science and Business Media, 1970.

[64] A. Eringen, "Theory of micropolar elasticity," *Fracture*, vol. 1, pp. 621–729, 1968.

[65] A. Eringen, "Nonlocal polar elastic continua," *International Journal of Engineering Science*, vol. 10, pp. 1–16, jan 1972.

[66] A. C. Eringen, ed., *Nonlocal Continuum Field Theories*. Springer Science and Business Media, 2004.

[67] A. Eringen and D. Edelen, "On nonlocal elasticity," *International Journal of Engineering Science*, vol. 10, pp. 233–248, mar 1972.

[68] J. Reddy, "Nonlocal theories for bending, buckling and vibration of beams," *International Journal of Engineering Science*, vol. 45, pp. 288–307, feb 2007.

[69] C. Roque, A. Ferreira, and J. Reddy, "Analysis of timoshenko nanobeams with a nonlocal formulation and meshless method," *International Journal of Engineering Science*, vol. 49, pp. 976–984, sep 2011.

[70] J. Phadikar and S. Pradhan, "Variational formulation and finite element analysis for nonlocal elastic nanobeams and nanoplates," *Computational Materials Science*, vol. 49, pp. 492–499, sep 2010.

[71] N. Challamel and C. M. Wang, "The small length scale effect for a non-local cantilever beam: a paradox solved," *Nanotechnology*, vol. 19, p. 345703, jul 2008.

[72] C. M. Wang, S. Kitipornchai, C. W. Lim, and M. Eisenberger, "Beam bending solutions based on nonlocal timoshenko beam theory," *J. Eng. Mech.*, vol. 134, pp. 475–481, jun 2008.

[73] C. M. Wang, Y. Y. Zhang, S. S. Ramesh, and S. Kitipornchai, "Buckling analysis of micro- and nano-rods/tubes based on nonlocal timoshenko beam theory," *Journal of Physics D: Applied Physics*, vol. 39, pp. 3904–3909, aug 2006.

[74] C. Lim, "Equilibrium and static deflection for bending of a nonlocal nanobeam," *Advances in Vibration Engineering*, vol. 8, pp. 277–300, 2009.

[75] Y. Y. Zhang, C. M. Wang, and N. Challamel, "Bending, buckling, and vibration of micro/nanobeams by hybrid nonlocal beam model," *J. Eng. Mech.*, vol. 136, pp. 562–574, may 2010.

[76] S. Pradhan, "Nonlocal finite element analysis and small scale effects of CNTs with timoshenko beam theory," *Finite Elements in Analysis and Design*, vol. 50, pp. 8–20, mar 2012.

[77] F.-Y. Huang, B.-H. Yan, J.-L. Yan, and D.-U. Yang, "Bending analysis of micropolar elastic beam using a 3-D finite element method," *International Journal of Engineering Science*, vol. 38, pp. 275–286, feb 2000.

[78] L. Li and S. Xie, "Finite element method for linear micropolar elasticity and numerical study of some scale effects phenomena in MEMS," *International Journal of Mechanical Sciences*, vol. 46, pp. 1571–1587, nov 2004.

[79] S. Ramezani, R. Naghdabadi, and S. Sohrabpour, "Analysis of micropolar elastic beams," *European Journal of Mechanics - A/Solids*, vol. 28, pp. 202–208, mar 2009.

[80] X.-Q. Fang and C.-S. Zhu, "Size-dependent nonlinear vibration of nonhomogeneous shell embedded with a piezoelectric layer based on surface/interface theory," *Composite Structures*, vol. 160, pp. 1191–1197, jan 2017.

[81] C.-S. Zhu, X.-Q. Fang, and J.-X. Liu, "Surface energy effect on buckling behavior of the functionally graded nano-shell covered with piezoelectric nanolayers under torque," *International Journal of Mechanical Sciences*, vol. 133, pp. 662–673, nov 2017.

[82] R. Mindlin, "Micro-structure in linear elasticity," *Archive for Rational Mechanics and Analysis*, vol. 16, no. 1, 1964.

[83] R. Mindlin and N. Eshel, "On first strain-gradient theories in linear elasticity," *International Journal of Solids and Structures*, vol. 4, pp. 109–124, jan 1968.

[84] W. Koiter, "Couple stresses in the theory of elasticity," *I and II.Proc.K.Ned.Akad.Wet. (B)*, vol. 67, pp. 17–44, 1964.

[85] N. A. Fleck and J. W. Hutchinson, "A phenomenological theory for strain gradient effects in plasticity," *Journal of the Mechanics and Physics of Solids*, vol. 41, pp. 1825–1857, dec 1993.

[86] N. A. Fleck and J. W. Hutchinson, "Strain gradient plasticity," *Advances in Applied Mechanics*, vol. 33, pp. 296–358, 1997.

[87] N. A. Fleck and J. W. Hutchinson, "A reformulation of strain gradient plasticity," *Journal of the Mechanics and Physics of Solids*, vol. 49, pp. 2245–2271, oct 2001.

[88] C.W.Lim, G. Zhang, and J. Reddy, "A higher-order nonlocal elasticity and strain gradient theory and its applications in wave propagation," *Journal of the Mechanics and Physics of Solids*, vol. 78, pp. 298–313, 2015.

[89] F. Yang, A. Chong, D. Lam, and P. Tong, "Couple stress based strain gradient theory for elasticity," *International Journal of Solids and Structures*, vol. 39, pp. 2731–2743, may 2002.

[90] S. Kong, S. Zhou, Z. Nie, and K. Wang, "Static and dynamic analysis of micro beams based on strain gradient elasticity theory," *International Journal of Engineering Science*, vol. 47, pp. 487–498, apr 2009.

[91] B. Wang, J. Zhao, and S. Zhou, "A micro scale timoshenko beam model based

on strain gradient elasticity theory," *European Journal of Mechanics - A/Solids*, vol. 29, pp. 591–599, jul 2010.

[92] M. Kahrobaiyan, M. Asghari, and M. Ahmadian, "Strain gradient beam element," *Finite Elements in Analysis and Design*, vol. 68, pp. 63–75, jun 2013.

[93] M. Kahrobaiyan, M. Asghari, M. Rahaeifard, and M. Ahmadian, "A nonlinear strain gradient beam formulation," *International Journal of Engineering Science*, vol. 49, pp. 1256–1267, nov 2011.

[94] B. Akgöz and Ömer Civalek, "A size-dependent shear deformation beam model based on the strain gradient elasticity theory," *International Journal of Engineering Science*, vol. 70, pp. 1–14, 2013.

[95] B. Akgöz and Ömer Civalek, "Strain gradient elasticity and modified couple stress models for buckling analysis of axially loaded micro-scaled beams," *International Journal of Engineering Science*, vol. 49, pp. 1268–1280, nov 2011.

[96] J. Zhao, S. Zhou, B. Wang, and X. Wang, "Nonlinear microbeam model based on strain gradient theory," *Applied Mathematical Modelling*, vol. 36, pp. 2674–2686, jun 2012.

[97] M. Asghari, M. H. Kahrobaiyan, M. Nikfar, and M. T. Ahmadian, "A size-dependent nonlinear timoshenko microbeam model based on the strain gradient theory," *Acta Mechanica*, vol. 223, pp. 1233–1249, mar 2012.

[98] R. Vatankhah, M. Kahrobaiyan, A. Alasty, and M. Ahmadian, "Nonlinear forced vibration of strain gradient microbeams," *Applied Mathematical Modelling*, vol. 37, pp. 8363–8382, oct 2013.

[99] A. Triantafyllou and A. Giannakopoulos, "Structural analysis using a dipolar elastic timoshenko beam," *European Journal of Mechanics - A/Solids*, vol. 39, pp. 218–228, may 2013.

[100] M. H. Ghayesh, M. Amabili, and H. Farokhi, "Nonlinear forced vibrations of a microbeam based on the strain gradient elasticity theory," *International Journal of Engineering Science*, vol. 63, pp. 52–60, feb 2013.

[101] B. Zhang, Y. He, D. Liu, Z. Gan, and L. Shen, "Non-classical timoshenko beam element based on the strain gradient elasticity theory," *Finite Elements in Analysis and Design*, vol. 79, pp. 22–39, feb 2014.

[102] M. Rahaeifard, M. Ahmadian, and K. Firoozbakhsh, "A strain gradient based yield criterion," *International Journal of Engineering Science*, vol. 77, pp. 45–54, apr 2014.

[103] E. Taati, M. M. Najafabadi, and H. B. Tabrizi, "Size-dependent generalized thermoelasticity model for timoshenko microbeams," *Acta Mechanica*, vol. 225, pp. 1823–1842, nov 2013.

[104] S. K. Park and X.-L. Gao, "Bernoulli-euler beam model based on a modified couple stress theory," *J. Micromech. Microeng.*, vol. 16, pp. 2355–2359, sep 2006.

[105] S. Kong, S. Zhou, Z. Nie, and K. Wang, "The size-dependent natural frequency of bernoulli–Euler micro-beams," *International Journal of Engineering Science*, vol. 46, pp. 427–437, may 2008.

[106] H. Ma, X. L. Gao, and J. N. Reddy, "A microstructure-dependent timoshenko beam model based on a modified couple stress theory," *Journal of the Mechanics and Physics of Solids*, vol. 56, pp. 3379–3391, 2008.

[107] M. Asghari, M. Kahrobaiyan, and M. Ahmadian, "A nonlinear timoshenko beam formulation based on the modified couple stress theory," *International Journal of Engineering Science*, vol. 48, pp. 1749–1761, dec 2010.

[108] J. Reddy, "Microstructure-dependent couple stress theories of functionally graded beams," *Journal of the Mechanics and Physics of Solids*, vol. 59, pp. 2382–2399, nov 2011.

[109] H.-L. Lee and W.-J. Chang, "Sensitivity of v-shaped atomic force microscope cantilevers based on a modified couple stress theory," *Microelectronic Engineering*, vol. 88, pp. 3214–3218, nov 2011.

[110] M. Baghani, "Analytical study on size-dependent static pull-in voltage of microcantilevers using the modified couple stress theory," *International Journal of Engineering Science*, vol. 54, pp. 99–105, may 2012.

[111] H. Farokhi, M. H. Ghayesh, and M. Amabili, “Nonlinear dynamics of a geometrically imperfect microbeam based on the modified couple stress theory,” *International Journal of Engineering Science*, vol. 68, pp. 11–23, jul 2013.

[112] M. Mohammad-Abadi and A. Daneshmehr, “Size dependent buckling analysis of microbeams based on modified couple stress theory with high order theories and general boundary conditions,” *International Journal of Engineering Science*, vol. 74, pp. 1–14, jan 2014.

[113] M. Shaat and S. Mohamed, “Nonlinear-electrostatic analysis of micro-actuated beams based on couple stress and surface elasticity theories,” *International Journal of Mechanical Sciences*, vol. 84, pp. 208–217, jul 2014.

[114] M. Shaat, F. Mahmoud, X.-L. Gao, and A. Faheem, “Size-dependent bending analysis of kirchhoff nano-plates based on a modified couple-stress theory including surface effects,” *International Journal of Mechanical Sciences*, vol. 79, pp. 31–37, 2014.

[115] M. Kahrobaiyan, M. Asghari, M. Rahaeifard, and M. Ahmadian, “Investigation of the size-dependent dynamic characteristics of atomic force microscope microcantilevers based on the modified couple stress theory,” *International Journal of Engineering Science*, vol. 48, pp. 1985–1994, dec 2010.

[116] M. Kahrobaiyan, M. Rahaeifard, and M. Ahmadian, “A size-dependent yield criterion,” *International Journal of Engineering Science*, vol. 74, pp. 151–161, jan 2014.

[117] B. Zhao, T. Liu, J. Chen, X. Peng, and Z. Song, “A new bernoulli–euler beam model based on modified gradient elasticity.,” *Archive of Applied Mechanics*, vol. 89, pp. 277–289, 2019.

[118] B. Akgöz and Ömer Civalek, “A microstructure-dependent sinusoidal plate model based on the strain gradient elasticity theory,” *Acta Mechanica*, vol. 226, pp. 2277–2294, feb 2015.

[119] A. Li, S. Zhou, S. Zhou, and B. Wang, “A size-dependent model for bi-layered kirchhoff micro-plate based on strain gradient elasticity theory,” *Composite Structures*, vol. 113, pp. 272–280, jul 2014.

[120] S. Sahmani and R. Ansari, "On the free vibration response of functionally graded higher-order shear deformable microplates based on the strain gradient elasticity theory," *Composite Structures*, vol. 95, pp. 430–442, jan 2013.

[121] B. Wang, S. Zhou, J. Zhao, and X. Chen, "A size-dependent kirchhoff microplate model based on strain gradient elasticity theory," *European Journal of Mechanics - A/Solids*, vol. 30, pp. 517–524, jul 2011.

[122] B. Wang, S. Huang, J. Zhao, and S. Zhou, "Reconsiderations on boundary conditions of kirchhoff micro-plate model based on a strain gradient elasticity theory," *Applied Mathematical Modelling*, vol. 40, pp. 7303–7317, aug 2016.

[123] J. L. Batoz and M. B. Tahar, "Evaluation of a new quadrilateral thin plate bending element," *International Journal for Numerical Methods in Engineering*, vol. 18, pp. 1655–1677, 1982.

[124] S. Kapuria and S. Kulkarni, "An improved discrete kirchhoff quadrilateral element based on third-order zigzag theory for static analysis of composite and sandwich plates," *International Journal for Numerical Methods in Engineering*, vol. 69, pp. 1948–1981, 2007.

[125] R. Clough and C. Felippa, "A refined quadrilateral element for analysis of plate bending," *2nd Conference on Matrix Methods in Structural Mechanics*, 1968.

[126] B. M. Fraeijs de Veubeke, "A conforming finite element for plate bending," *International Journal of Solids and Structures*, vol. 4, pp. 95–108, 01 1968.

[127] M. Bischoff and E. Ramm, "Shear deformable shell elements for large strains and rotations," *International Journal for Numerical Methods in Engineering*, vol. 40, pp. 4427–4449, 1997.

[128] M. Bishcoff, K.-U. Bletzinger, W. Wall, and E. Ramm, "Models and finite elements for thin-walled structures," *Encyclopedia of Computational Mechanics. Part 2. Solids and Structures*, vol. 1, 2004.

[129] K.-U. Bletzinger, M. Bischoff, and E. Ramm, "A unified approach for shear-locking-free triangular and rectangular shell finite elements," *Computers and Structures*, vol. 75, pp. 321–334, 2000.

[130] T. J. R. Hughes, R. Taylor, and W. Kanok-Nukulchai, "A simple and efficient fe for plate bending," *International Journal for Numerical Methods in Engineering*, vol. 11, pp. 1529 – 1543, 01 1977.

[131] R. H. Macneal, "A simple quadrilateral shell element," *Computers and Structures*, vol. 8, pp. 175–183, 04 1978.

[132] A. Tessler and T. J.R. Hughes, "Three-node mindlin plate element with improved transverse shear," *Computer Methods in Applied Mechanics and Engineering*, vol. 50, pp. 71–101, 07 1985.

[133] E. Ramm, E. Rank, R. Rannacher, K. Schweizerhof, E. Stein, W. Wendland, G. Wittum, P. Wriggers, W. Wunderlich, and E. Stein, *Error-controlled Adaptive Finite Elements in Solid Mechanics (1st Ed).* 2002.

[134] G. Bazeley, Y. Cheung, B. Irons, and O. Zienkiewicz, "Triangular elements in plate bending— conforming and non-conforming solutions," *Proceedings of the First Conference on Matrix Methods in Structural Mechanics, Wright Patterson AFB, Dayton, Ohio*, 1965.

[135] K. Bell, "A refined triangular plate bending finite element," *International Journal for Numerical Methods in Engineering*, vol. 1, pp. 101–122, 1969.

[136] L. S. D. Morley, "The constant-moment plate-bending element," *The Journal of Strain Analysis for Engineering Design*, vol. 6, pp. 20–24, 1971.

[137] R. W. Clough and J. L. Tocher, "Finite element stiffness matrices for analysis of plates in bending," *Proc. Conf. Matrix Methods in Struct. Mech., Air Force Inst. Tech.*, 1965.

[138] G. Bazeley, Y. Cheung, B. Irons, and O. Zienkiewicz, "Triangular elements in bending-conforming and non-conforming solutions proc. conf. matrix meth. in struct. mech.," *Proc. Conf. Matrix Methods in Struct. Mech., Air Force Inst. Tech.*, 1965.

[139] T. Hughes and R. Taylor, "The linear triangular bending element," *J.R. Whiteman, ed., IV-MAFELAP*, pp. 127–142, 1981.

[140] A. Tessler, “A priori identification of shear locking and stiffening in triangular mindlin elements,” *Computer Methods in Applied Mechanics and Engineering*, vol. 53, pp. 183–200, 1985.

[141] I. Fried, A. Johnson, and A. Tessler, “Minimal degree thin triangular plate bending finite elements of order two and four,” *Computer Methods in Applied Mechanics and Engineering*, vol. 3, pp. 283–307, 1986.

[142] J. Batoz and I. Katili, “On a simple triangular reissner/mindlin plate element based on incompatible modes and discrete constraints,” *International Journal for Numerical Methods in Engineering*, vol. 35, pp. 1603–1632, 1992.

[143] S. Brasile, “An isostatic assumed stress triangular element for the reissner–mindlin plate-bending problem,” *International Journal for Numerical Methods in Engineering*, vol. 74, pp. 971–995, 2008.

[144] Y. Cai, L. Tian, and S. Atluri, “A simple locking-free discrete shear triangular plate element,” *Computer Modeling in Engineering and Sciences*, vol. 4, pp. 221–238, 2011.

[145] W. Chen and Y. Cheung, “Refined 9-dof triangular mindlin plate elements,” *International Journal for Numerical Methods in Engineering*, vol. 51, pp. 1259–1281, 2001.

[146] Y. Choo, N. Choi, and B. Lee, “A new hybrid-trefftz triangular and quadrilateral plate elements,” *Applied Mathematical Modelling*, vol. 34, pp. 14–23, 2010.

[147] I. Katili, “A new discrete kirchhoff-mindlin element based on mindlin- reissner plate theory and assumed shear strain fields—part i: an extended dkt element for thick-plate bending analysis,” *International Journal for Numerical Methods in Engineering*, vol. 36, pp. 1859–1883, 1993.

[148] X. Nguyen, T. Rabczuk, B. Stephane, and J. Debongnie, “A smoothed finite element method for plate analysis,” *Computer Methods in Applied Mechanics and Engineering*, vol. 197, p. 1184–1203, 2008.

[149] A. Adini and R. W. Clough, “Analysis of plate bending by the finite element method,” *NSF Report*, vol. 7337, 1961.

[150] R. Melosh, “Basis for derivation of matrices for the direct stiffness method,” *AIAA Journal*, vol. 1, pp. 1631–1637, 1963.

[151] F. Bogner, R. Fox, and L. Schmit, “The generation of interelement compatible stiffness and mass matrices by the use of interpolation formulas,” *Proceedings of the Conference on Matrix Methods in Structural Mechanics, Wright-Patterson Air Force Base, Ohio*, p. 397–444, 1965.

[152] P. Wriggers, *Nonlinear finite element methods*. Springer, 2008.

[153] R. Cook, D. Malkus, M. Plesha, and R. Witt, *Concepts and applications of finite element analysis*. Wiley, 2002.

[154] B. Akgöz and O. Civalek, “Analysis of micro-sized beams for various boundary conditions based on the strain gradient elasticity theory,” *Archive of Applied Mechanics*, vol. 82, pp. 423–443, 2012.

[155] A. Dehrouyeh-Semnani and M. Nikkhah-Bahrami, “A discussion on incorporating the poisson effect in microbeam models based on modified couple stress theory,” *International Journal of Engineering Science*, vol. 86, pp. 20–25, 2015.

[156] O. C. Zienkiewicz and R. L. Taylor, eds., *The Finite Element Method, 5th Ed.* Butterworth-Heinemann, 2000.

[157] M. Kandaz and H. Dal, “A comparative study of modified strain gradient theory and modified couple stress theory for gold microbeams,” *Archive of Applied Mechanics*, vol. 88, pp. 2051–2070, 2018.

[158] S. Jardin, “A triangular finite element with first-derivative continuity applied to fusion mhd applications,” *Journal of Computational Physics*, vol. 200, p. 133–152, 2004.

[159] L. Ferreira and M. Bittencourt, “Hierarchical high-order conforming c1 bases for quadrangular and triangular finite elements,” *International Journal for Numerical Methods in Engineering*, vol. 109, p. 936–964, 2016.

[160] S. Timoshenko and S. Woinowsky-Krieger, *Theory of Plates and Shells*. McGraw-Hill, 1959.

[161] A. Ugural, *Stresses in Plates and Shells, 3rd Ed.* CRC Press, 2009.

[162] Y. Gao, Y. Sun, and T. Zhang, "Highly reliable and efficient atomic force microscopy based bending test for assessing young's modulus of one-dimensional nanomaterials," *Applied Physics Letters*, vol. 108, p. 123104, 2016.

[163] D. Lee, X. Wei, X. Chen, M. Zhao, S. Jun, J. Hone, E. G. Herbert, W. C. Oliver, and J. W. Kysar, "Microfabrication and mechanical properties of nanoporous gold at the nanoscale," *Scripta Materialia*, vol. 56, p. 437–440, Mar 2007.

[164] "Nanomagnetics instruments, hpafm." `https://www.nanomagnetics-inst.com/product/high-performance-afm-mfm-hpafm/`. Accessed: 2019-12-12.

[165] "Afm workshop acla probes, acla-10." `https://www.afmworkshop.com/~afmworks/images/datasheets/ProbeACLA-10_Datasheet_FINAL_1.pdf`. Accessed: 2019-12-12.

Appendix A

TENSOR OPERATORS

The tensor operators used in Section 2 are summarized in the table below.

Table A.1: Description of tensor operators used in Section 2, i.e. $(\cdot)$, $(:)$, $(\vdots)$, $(\otimes)$, $(\bullet)^T$ and $(\bullet)^{\overset{13}{T}}$ in compact and indicial notation

Operator	Symbol	Compact notation	Indicial notation
Dot product	$(\cdot)$	$\mathbf{a} \cdot \mathbf{b}$	$a_i b_i$
Double contraction	$(:)$	$\sigma : \varepsilon$	$\sigma_{ij}\varepsilon_{ij}$
Triple contraction	$(\vdots)$	$\eta \vdots \eta$	$\eta_{ijk}\eta_{ijk}$
Dyadic product	$(\otimes)$	$\mathbf{a} \otimes \mathbf{b}$	$a_i b_j$
Transpose operator (Second order)	$(\bullet)^T$	σ^T	$(\sigma^T)_{ij} = \sigma_{ji}$
Transpose operator (Third order)	$(\bullet)^{\overset{13}{T}}$	$\eta^{\overset{13}{T}}$	$(\eta^{\overset{13}{T}})_{ijk} = \eta_{kij}$

Appendix B

DERIVATION OF STRESS AND STRAIN METRICS IN MSGT FOR KIRCHHOFF PLATES

The internal energy equation with the strain and stress metrics of MSGT can be written as

$$\Pi^{int} = \frac{1}{2}\int_{\mathcal{B}} \left(\boldsymbol{\sigma} : \boldsymbol{\varepsilon} + \mathbf{p} \cdot \nabla\boldsymbol{\varepsilon} + \boldsymbol{\tau} \vdots \boldsymbol{\eta}^{\mathbf{1}} + \mathbf{m} \cdot \boldsymbol{\chi}\right) dV. \tag{B.1}$$

Equation B.1 can be rewritten in indicial notation as:

$$\Pi^{int} = \frac{1}{2}\int_{\mathcal{B}} \left(\sigma_{ij}\varepsilon_{ij} + p_i\gamma_i + \tau_{ijk}\eta_{ijk} + m_{ij}\chi_{ij}\right) dV, \tag{B.2}$$

where γ is expressed as the dilation gradient vector as

$$\gamma = \nabla\varepsilon \text{ (compact notation)}, \quad \gamma_i = \varepsilon_{mm,i} \text{ (indicial notation)} \tag{B.3}$$

in compact notation and indicial notation respectively. Then, for a general plate structure,

$$\begin{aligned}
\delta\Pi^{int} = \int_V \quad & (\sigma_{xx}\delta\varepsilon_{xx} + 2\sigma_{xy}\delta\varepsilon_{xy} + \sigma_{yy}\delta\varepsilon_{yy} + p_x\delta\gamma_x + p_y\delta\gamma_y + p_z\delta\gamma_z \\
& + \tau^1_{xxx}\delta\eta^1_{xxx} + 3\tau^1_{xxy}\delta\eta^1_{xxy} + 3\tau^1_{xxz}\delta\eta^1_{xxz} + 3\tau^1_{xyy}\delta\eta^1_{xyy} \\
& + \tau^1_{yyy}\delta\eta^1_{yyy} + 3\tau^1_{yyz}\delta\eta^1_{yyz} + 3\tau^1_{xzz}\delta\eta^1_{xzz} + 3\tau^1_{yzz}\delta\eta^1_{yzz} \\
& + \tau^1_{zzz}\delta\eta^1_{zzz} + 6\tau^1_{xyz}\delta\eta^1_{xyz} + m_{xx}\delta\chi_{xx} + 2m_{xy}\delta\chi_{xy} \\
& + m_{yy}\delta\chi_{yy})\, dV.
\end{aligned} \tag{B.4}$$

In order to evaluate above, the terms are identified. Using the displacement field of a Kirchhoff plate given in Equation 2.46 the classical strain terms can be found as:

$$\varepsilon_{xx} = -z\, w_{,xx}, \quad \varepsilon_{yy} = -z\, w_{,yy}, \quad \varepsilon_{xy} = -z\, w_{,xy}. \tag{B.5}$$

The dilatation gradient terms can then be derived as:

$$\gamma_x = \varepsilon_{mm,x} = -z\frac{\partial}{\partial x}\left(\nabla^2 w\right) = -z\left(w_{,xxx} + w_{,yyx}\right), \tag{B.6}$$

$$\gamma_y = \varepsilon_{mm,y} = -z\frac{\partial}{\partial y}\left(\nabla^2 w\right) = -z\left(w,_{yxx} + w,_{yyy}\right), \tag{B.7}$$

$$\gamma_z = \varepsilon_{mm,z} = \nabla^2 w = w,_{xx} + w,_{yy}\,. \tag{B.8}$$

The indicial expression for deviatoric stretch gradient terms (η^1) is:

$$\eta^1_{ijk} = \eta^S_{ijk} - \frac{1}{5}\left(\delta_{ij}\eta^S_{mmk} + \delta_{jk}\eta^S_{mmi}\delta_{ki}\eta^S_{mmj}\right) \tag{B.9}$$

where

$$\eta^S_{ijk} = \frac{1}{3}\left(u_{i,jk} + u_{j,ki} + u_{k,ij}\right), \tag{B.10}$$

and where δ_{ij} is the Kronecker's delta. After several steps,

$$\eta^1_{xxx} = \frac{z}{5}\left(-2\frac{\partial^3 w}{\partial x^3} + 3\frac{\partial^3 w}{\partial y^2 \partial x}\right), \tag{B.11}$$

$$\eta^1_{xxy} = \frac{z}{5}\left(-4\frac{\partial^3 w}{\partial x^2 \partial y} + \frac{\partial^3 w}{\partial y^3}\right), \tag{B.12}$$

$$\eta^1_{xyy} = \frac{z}{5}\left(-4\frac{\partial^3 w}{\partial x \partial y^2} + \frac{\partial^3 w}{\partial x^3}\right), \tag{B.13}$$

$$\eta^1_{yyy} = \frac{z}{5}\left(-2\frac{\partial^3 w}{\partial y^3} + 3\frac{\partial^3 w}{\partial x^2 \partial y}\right), \tag{B.14}$$

$$\eta^1_{xxz} = \frac{1}{15}\left(-4\frac{\partial^2 w}{\partial x^3} + \frac{\partial^2 w}{\partial y^2}\right), \tag{B.15}$$

$$\eta^1_{xzz} = \frac{z}{5}\left(\frac{\partial^3 w}{\partial x^3} + \frac{\partial^3 w}{\partial x \partial y^2}\right) = \frac{z}{5}\frac{\partial}{\partial x}\left(\nabla^2 w\right), \tag{B.16}$$

$$\eta^1_{yzz} = \frac{z}{5}\left(\frac{\partial^3 w}{\partial y^3} + \frac{\partial^3 w}{\partial y \partial x^2}\right) = \frac{z}{5}\frac{\partial}{\partial y}\left(\nabla^2 w\right), \tag{B.17}$$

$$\eta^1_{zzz} = \frac{1}{5}\left(\frac{\partial^2 w}{\partial x^2} + \frac{\partial^2 w}{\partial y^2}\right) = \frac{1}{5}\nabla^2 w, \tag{B.18}$$

$$\eta^1_{xyz} = -\frac{1}{3}\frac{\partial^2 w}{\partial x \partial y}, \tag{B.19}$$

with

$$\eta^1_{xyx} = \eta^1_{yxx} = \eta^1_{xxy}, \tag{B.20}$$

$$\eta^1_{xzx} = \eta^1_{zxx} = \eta^1_{xxz}, \tag{B.21}$$

$$\eta^1_{yxy} = \eta^1_{yyx} = \eta^1_{xyy}, \tag{B.22}$$

$$\eta^1_{zxz} = \eta^1_{zzx} = \eta^1_{xzz}, \tag{B.23}$$

$$\eta^1_{zyz} = \eta^1_{zzy} = \eta^1_{yzz}, \tag{B.24}$$

$$\eta^1_{yzx} = \eta^1_{zxy} = \eta^1_{zyx} = \eta^1_{yxz} = \eta^1_{xzy} = \eta^1_{xyz}. \tag{B.25}$$

The indicial expression for the rotation gradient terms (χ) is:

$$\chi_{ij} = \frac{1}{4}\left(e_{imn}\, u_{n,mj} + e_{jmn}\, u_{n,mi}\right) \tag{B.26}$$

where e_{ijk} is the Levi-Civita symbol. Hence, again after several steps:

$$\chi_{xx} = \frac{\partial^2 w}{\partial x \partial y}, \tag{B.27}$$

$$\chi_{yy} = -\frac{\partial^2 w}{\partial x \partial y}, \tag{B.28}$$

$$\chi_{xy} = \frac{1}{2}\left(\frac{\partial^2 w}{\partial y^2} - \frac{\partial^2 w}{\partial x^2}\right), \tag{B.29}$$

with

$$\chi_{zz} = \chi_{zx} = \chi_{xz} = \chi_{yz} = \chi_{zy} = 0. \tag{B.30}$$

Taking the variations of above expressions and multiplying with their stress conjugates as appearing in Equation B.4, the following are acquired:

$$\sigma_{xx}\, \delta\varepsilon_{xx} = -\sigma_{xx} z\, \delta w_{,xx}, \tag{B.31}$$

$$2\sigma_{xy}\, \delta\varepsilon_{xy} = -2\sigma_{xy} z\, \delta w_{,xy}, \tag{B.32}$$

$$\sigma_{yy}\, \delta\varepsilon_{yy} = -\sigma_{yy} z\, \delta w_{,yy}, \tag{B.33}$$

$$p_x\,\delta\gamma_x = -p_x z\,\delta w_{,xxx} - p_x z\,\delta w_{,xyy} \tag{B.34}$$

$$p_y\,\delta\gamma_y = -p_y z\,\delta w_{,yyy} - p_y z\,\delta w_{,xxy} \tag{B.35}$$

$$p_z\,\delta\gamma_z = -p_z\,\delta w_{,xx} - p_z\,\delta w_{,yy} \tag{B.36}$$

$$\tau^1_{xxx}\,\delta\eta^1_{xxx} = -\frac{2}{5}z\tau^1_{xxx}\,\delta w_{,xxx} + \frac{3}{5}z\tau^1_{xxx}\,\delta w_{,xyy} \tag{B.37}$$

$$3\tau^1_{xxy}\,\delta\eta^1_{xxy} = -\frac{12}{5}z\tau^1_{xxy}\,\delta w_{,xxy} + \frac{3}{5}z\tau^1_{xxy}\,\delta w_{,yyy} \tag{B.38}$$

$$3\tau^1_{xxz}\,\delta\eta^1_{xxz} = -\frac{-4}{5}\tau^1_{xxz}\,\delta w_{,xx} + \frac{1}{5}\tau^1_{xxz}\,\delta w_{,yy} \tag{B.39}$$

$$3\tau^1_{xyy}\,\delta\eta^1_{xyy} = -\frac{12}{5}z\tau^1_{xyy}\,\delta w_{,xyy} + \frac{3}{5}z\tau^1_{xyy}\,\delta w_{,xxx} \tag{B.40}$$

$$\tau^1_{yyy}\,\delta\eta^1_{yyy} = \frac{3}{5}z\tau^1_{yyy}\,\delta w_{,xxy} - \frac{1}{5}z\tau^1_{yyy}\,\delta w_{,yyy} \tag{B.41}$$

$$3\tau^1_{yyz}\,\delta\eta^1_{yyz} = \frac{1}{5}\tau^1_{yzz}\,\delta w_{,xx} - \frac{4}{5}\tau^1_{yyz}\,\delta w_{,yy} \tag{B.42}$$

$$\tau^1_{xzz}\,\delta\eta^1_{xzz} = \frac{3}{5}z\tau^1_{xzz}\,\delta w_{,xxx} - \frac{3}{5}z\tau^1_{xzz}\,\delta w_{,xyy} \tag{B.43}$$

$$\tau^1_{yzz}\,\delta\eta^1_{yzz} = \frac{3}{5}z\tau^1_{yzz}\,\delta w_{,xxy} - \frac{1}{5}z\tau^1_{yzz}\,\delta w_{,yyy} \tag{B.44}$$

$$\tau^1_{zzz}\,\delta\eta^1_{zzz} = \frac{1}{5}\tau^1_{zzz}\,\delta w_{,xx} - \frac{1}{5}\tau^1_{zzz}\,\delta w_{,yy} \tag{B.45}$$

$$6\tau^1_{xyz}\,\delta\eta^1_{xyz} = -2\tau^1_{xyz}\,\delta w_{,xy} \tag{B.46}$$

$$m_{xx}\,\delta\chi_{xx} = m_{xx}\,\delta w_{,xy} \tag{B.47}$$

$$2m_{xy}\,\delta\chi_{xy} = m_{xy}\,\delta w_{,yy} - m_{xy}\,\delta w_{,xx} \tag{B.48}$$

$$m_{yy}\,\delta\chi_{yy} = -m_{yy}\,\delta w_{,xy} \tag{B.49}$$

Given the above expressions, Equation B.4 can now we written as:

$$\begin{aligned}\delta\Pi^{int} = \int_\Omega & \left(M_{xx}\,\delta w_{,xx} + M_{xy}\,\delta w_{,xy} + M_{yy}\,\delta w_{,yy}\right.\\ & \left. + Q_{xxx}\,\delta w_{,xxx} + Q_{xxy}\,\delta w_{,xxy} + Q_{xyy}\,\delta w_{,xyy} + Q_{yyy}\,\delta w_{,yyy}\right) d\Omega.\end{aligned} \tag{B.50}$$

where Ω is 2D domain of the undeformed mid-plane of the plate bounded by a piece-wise smooth curve Γ. Then

$$M_{xx} = \int_{-h/2}^{h/2}\left[-\sigma_{xx}z - p_z - \frac{4}{5}\tau^1_{xxz} + \frac{1}{5}\tau^1_{yyz} + \frac{1}{5}\tau^1_{zzz} - m_{xy}\right] dz \tag{B.51}$$

$$M_{xy} = \int_{-h/2}^{h/2}\left[-2\sigma_{xy}z - 2\tau^1_{xyz} + m_{xx} - m_{yy}\right] dz \tag{B.52}$$

$$M_{yy} = \int_{-h/2}^{h/2}\left[-\sigma_{yy}z - p_z + \frac{1}{5}\tau^1_{xxz} - \frac{4}{5}\tau^1_{yyz} + \frac{1}{5}\tau^1_{zzz} + m_{xy}\right] dz \tag{B.53}$$

$$Q_{xxx} = \int_{-h/2}^{h/2}\left[\frac{z}{5}\left(-5p_x - 2\tau^1_{xxx} + 3\tau^1_{xyy} + 3\tau^1_{xzz}\right)\right] dz \tag{B.54}$$

$$Q_{xxy} = \int_{-h/2}^{h/2}\left[\frac{z}{5}\left(-5p_x + 2\tau^1_{xxx} - 12\tau^1_{xyy} + 3\tau^1_{xzz}\right)\right] dz \tag{B.55}$$

$$Q_{xyy} = \int_{-h/2}^{h/2}\left[\frac{z}{5}\left(-5p_y - 12\tau^1_{xxy} + 3\tau^1_{yyy} + 3\tau^1_{yzz}\right)\right] dz \tag{B.56}$$

$$Q_{yyy} = \int_{-h/2}^{h/2}\left[\frac{z}{5}\left(-5p_y + 3\tau^1_{xxy} - 2\tau^1_{yyy} + 3\tau^1_{yzz}\right)\right] dz \tag{B.57}$$

Inserting the stress metrics,

$$\begin{aligned}M_{xx} = \;& \mu h\left(\frac{h^2}{6(1-\nu)} + 2\mu l_0^2 + \frac{8}{15}\mu l_1^2 + \mu l_2^2\right) w_{,xx} +\\ & \mu h\left(\frac{\nu h^2}{6(1-\nu)} + 2\mu l_0^2 - \frac{2}{15}\mu l_1^2 - \mu l_2^2\right) w_{,yy}\end{aligned} \tag{B.58}$$

$$M_{xy} = \; \mu h\left(\frac{h^2}{3} + \frac{4}{3}\mu l_1^2 + 4\mu l_2^2\right) w_{,xy} \tag{B.59}$$

$$M_{yy} = \mu h \left(\frac{h^2}{6(1-\nu)} + 2\mu l_0^2 - \frac{2}{15}\mu l_1^2 + \mu l_2^2 \right) w_{,xx} + \mu h \left(\frac{\nu h^2}{6(1-\nu)} + 2\mu l_0^2 + \frac{8}{15}\mu l_1^2 - \mu l_2^2 \right) w_{,yy} \tag{B.60}$$

$$Q_{xxx} = \frac{\mu h^3}{6} \left(l_0^2 + \frac{2}{5} l_1^2 \right) w_{,xxx} + \frac{\mu h^3}{6} \left(l_0^2 - \frac{3}{5} l_1^2 \right) w_{,xyy} \tag{B.61}$$

$$Q_{xxy} = \frac{\mu h^3}{6} \left(l_0^2 + \frac{12}{5} l_1^2 \right) w_{,xxy} + \frac{\mu h^3}{6} \left(l_0^2 - \frac{3}{5} l_1^2 \right) w_{,yyy} \tag{B.62}$$

$$Q_{xyy} = \frac{\mu h^3}{6} \left(l_0^2 - \frac{3}{5} l_1^2 \right) w_{,xxx} + \frac{\mu h^3}{6} \left(l_0^2 + \frac{12}{5} l_1^2 \right) w_{,xyy} \tag{B.63}$$

$$Q_{yyy} = \frac{\mu h^3}{6} \left(l_0^2 - \frac{3}{5} l_1^2 \right) w_{,xxy} + \frac{\mu h^3}{6} \left(l_0^2 + \frac{2}{5} l_1^2 \right) w_{,yyy} \tag{B.64}$$

Now, using the divergence theorem for Equation B.50 and minimum potential energy principle with

$$\Pi^{ext} = \int_\Omega q(x, y)\, \delta w d\Omega \tag{B.65}$$

the following equation is found:

$$M_{xx,xx} + M_{xy,xy} + M_{yy,yy} - Q_{xxx,xxx} - Q_{xxy,xxy} - Q_{xyy,xyy} - Q_{yyy,yyy} = q \tag{B.66}$$

Inserting Equations B.58-B.64 to above also leads to Equation 2.63.

Appendix C

6 DOF HIGHER ORDER BEAM ELEMENT - ANALYTICAL EXPRESSIONS OF SHAPE FUNCTIONS N_1^1 TO N_3^1

The first three elements of the shape function $\boldsymbol{N}$ for MSGT, i.e. N_1^1, N_2^1, and N_3^1 are as given below. N_1^2, N_2^2, and N_3^2 are symmetric with N_1^1, N_2^1, and N_3^1 respectively as given in Figure 3.3.

$$
\begin{aligned}
N_1^1 = \quad & [12\text{cosh}(q(s-1)) - 12\text{cosh}(qs) + 12\text{cosh}(q) + 6q^2s^2 - 4q^2s^3 \\
& +8q^2\text{cosh}(q) - q^3\text{sinh}(q) + 6q\text{sinh}(qs) - 6q^2s - 18q\text{sinh}(q) + 4q^2 \\
& +6q\text{sinh}(q(s-1)) + 12qs\text{sinh}(q) - 6q^2s\text{cosh}(q) - 6q^2s^2\text{cosh}(q) \\
& +4q^2s^3\text{cosh}(q) + 3q^3s^2\text{sinh}(q) - 2q^3s^3\text{sinh}(q) - 12]/D\,,
\end{aligned}
$$

$$
\begin{aligned}
N_2^1 = \quad & -[12\text{sinh}(q(s-1)) - 12\text{sinh}(qs) + 12\text{sinh}(q) - 2q^3s^3 + 4q^2\text{sinh}(q) \\
& -12qs + 4q^2\text{sinh}(q(s-1)) + 2q^3s - 12q\text{cosh}(q) + 12q\text{cosh}(q(s-1)) \\
& +2q^2\text{sinh}(qs) + 12qs\text{cosh}(q) + 4q^3s\text{cosh}(q) - 12q^2s\text{sinh}(q) - q^4s\text{sinh}(q) \\
& -6q^3s^2\text{cosh}(q) + 2q^3s^3\text{cosh}(q) + 6q^2s^2\text{sinh}(q) + 2q^4s^2\text{sinh}(q) \\
& -q^4s^3\text{sinh}(q)]L/(-qD)\,,
\end{aligned}
$$

$$
\begin{aligned}
N_3^1 = \quad & -[6\text{sinh}(q(s-1)) - 2q - 6\text{sinh}(qs) + 6\text{sinh}(q) + q^3s^2 - q^3s^3 + q^2\text{sinh}(q) \\
& +6qs + q^2\text{sinh}(q(s-1)) + 2q\text{cosh}(qs) - 12qs^2 + 4qs^3 - 4q\text{cosh}(q) \\
& +4q\text{cosh}(q(s-1)) - 6qs\text{cosh}(q) + 12qs^2\text{cosh}(q) - 4qs^3\text{cosh}(q) \\
& -q^3s\text{cosh}(q) + 4q^2s\text{sinh}(q) + 2q^3s^2\text{cosh}(q) - q^3s^3\text{cosh}(q) - 9q^2s^2\text{sinh}(q) \\
& +4q^2s^3\text{sinh}(q)]L^2/(-qD)\,.
\end{aligned}
\tag{C.1}
$$

where:

$$
\begin{aligned}
&q = L/\sqrt{c_1/c_2},\ s = x/L, \\
&D = 24\cosh(q) + 8q^2\cosh(q) - q^3\sinh(q) - 24q\sinh(q) + 4q^2 - 24
\end{aligned}
\tag{C.2}
$$

Appendix D

12 DOF CLASSICAL PLATE ELEMENT ANALYTICAL EXPRESSIONS OF SHAPE FUNCTIONS N_1^1 TO N_3^1

The first three elements of the shape function $\boldsymbol{N}$ for classical theory, which are shown in Figure 3.5, are as given below.

$$
\begin{aligned}
N_1^1 =& -2x^3y + 2x^3 + 3x^2y - 3x^2 - 2xy^3 + 2y^3 + 3xy^2 - 3y^2 - xy + 1 \\
N_2^1 =& -xy^3 + y^3 + 2xy^2 - 2y^2 - xy + y \\
N_3^1 =& x^3y - x^3 - 2x^2y + 2x^2 + xy - x
\end{aligned}
\tag{D.1}
$$

Appendix E

20 DOF PLATE ELEMENT ANALYTICAL EXPRESSIONS OF SHAPE FUNCTIONS N_1^1 TO N_5^1

The first five elements of the shape function $\boldsymbol{N}$ for MSGT, which are shown in Figure 3.7, are as given below.

$$
\begin{aligned}
N_1^1 = \quad & -(144A\sinh(A\xi_1) - 288\xi_2 - 288\cosh(A\xi_1) - 288\cosh(B\xi_2) - 288\xi_1 \\
& +144B\sinh(B\xi_2) + 576\xi_1\xi_2 + 288\xi_2\cosh(A\xi_1) + 288\xi_1\cosh(B\xi_2) \\
& -144A\sinh(A) - 144B\sinh(B) - 96A^2\xi_1 - 96B^2\xi_2 + 288\xi_1\cosh(A) \\
& +48B^2\cosh(A\xi_1) + 288\xi_1\cosh(B) + 288\xi_2\cosh(A) + 48A^2\cosh(B\xi_2) \\
& +288\xi_2\cosh(B) + 288\cosh(A\xi_1)\cosh(A) + 288\cosh(A\xi_1)\cosh(B) \\
& +288\cosh(B\xi_2)\cosh(A) + 288\cosh(B\xi_2)\cosh(B) \\
& -288\sinh(A\xi_1)\sinh(A) - 288\sinh(B\xi_2)\sinh(B) + 48A^2 - 16A^2B^2 \\
& +48B^2 + 96A^2\cosh(A) - 48A^2\cosh(B) - 48B^2\cosh(A) \\
& +96B^2\cosh(B) - 12A^3\sinh(A) - 12B^3\sinh(B) + 144A^2\xi_1^2 - 96A^2\xi_1^3 \\
& +144B^2\xi_2^2 - 96B^2\xi_2^3 + 288\xi_2\sinh(A\xi_1)\sinh(A) \\
& +288\xi_1\sinh(B\xi_2)\sinh(B) + 24A^2B^2\xi_1 + 24A^2B^2\xi_2 - 48A^2\xi_1\cosh(A) \\
& +96A^2\xi_1\cosh(B) + 96B^2\xi_2\cosh(A) - 48B^2\xi_2\cosh(B) \\
& -48B^2\cosh(A\xi_1)\cosh(A) - 288\xi_1\cosh(A)\cosh(B) \\
& +96B^2\cosh(A\xi_1)\cosh(B) + 96A^2\cosh(B\xi_2)\cosh(A) \\
& -288\xi_2\cosh(A)\cosh(B) - 48A^2\cosh(B\xi_2)\cosh(B) \\
& -288\cosh(A\xi_1)\cosh(A)\cosh(B) - 12A^3\xi_1\sinh(A) - 12B^3\xi_2\sinh(B) \\
& -12B^3\cosh(A\xi_1)\sinh(B) - 12A^3\cosh(B\xi_2)\sinh(A) \\
& +48B^2\sinh(A\xi_1)\sinh(A) + 48A^2\sinh(B\xi_2)\sinh(B) \\
& +288\sinh(B\xi_2)\cosh(A)\sinh(B) - 144A^2\xi_1^2\xi_2 + 96A^2\xi_1^3\xi_2 - 144B^2\xi_1\xi_2^2 \\
& +96B^2\xi_1\xi_2^3 - 32A^2B^2\cosh(A) - 32A^2B^2\cosh(B) \\
& -96A^2\cosh(A)\cosh(B) - 96B^2\cosh(A)\cosh(B) + 4A^3B^2\sinh(A)
\end{aligned}
$$

$$+4A^2B^3\sinh(B)+12A^3\cosh(B)\sinh(A)+12B^3\cosh(A)\sinh(B)$$
$$-24A^2B^2\xi_1^2+16A^2B^2\xi_1^3-24A^2B^2\xi_2^2+16A^2B^2\xi_2^3$$
$$-144A^2\xi_1^2\cosh(A)+96A^2\xi_1^3\cosh(A)-144A^2\xi_1^2\cosh(B)$$
$$+96A^2\xi_1^3\cosh(B)-144B^2\xi_2^2\cosh(A)+96B^2\xi_2^3\cosh(A)$$
$$-144B^2\xi_2^2\cosh(B)+96B^2\xi_2^3\cosh(B)+72A^3\xi_1^2\sinh(A)$$
$$-48A^3\xi_1^3\sinh(A)+72B^3\xi_2^2\sinh(B)-48B^3\xi_2^3\sinh(B)$$
$$-144A\xi_2\sinh(A\xi_1)-144B\xi_1\sinh(B\xi_2)-24AB^2\sinh(A\xi_1)$$
$$-144A\xi_2\sinh(A)-144B\xi_1\sinh(B)-144A\cosh(A\xi_1)\sinh(A)$$
$$+144A\sinh(A\xi_1)\cosh(A)-24A^2B\sinh(B\xi_2)$$
$$-144A\sinh(A\xi_1)\cosh(B)-288B\cosh(A\xi_1)\sinh(B)$$
$$-288A\cosh(B\xi_2)\sinh(A)-144B\sinh(B\xi_2)\cosh(A)$$
$$-144B\cosh(B\xi_2)\sinh(B)+144B\sinh(B\xi_2)\cosh(B)$$
$$+48A^2\xi_1\xi_2+48B^2\xi_1\xi_2-576\xi_1\xi_2\cosh(A)-48A^2\xi_1\cosh(B\xi_2)$$
$$-48B^2\xi_2\cosh(A\xi_1)-576\xi_1\xi_2\cosh(B)-288\xi_2\cosh(A\xi_1)\cosh(A)$$
$$-288\xi_1\cosh(B\xi_2)\cosh(A)-288\xi_2\cosh(A\xi_1)\cosh(B)$$
$$-288\xi_1\cosh(B\xi_2)\cosh(B)+72AB^2\sinh(A)+72A^2B\sinh(B)$$
$$+144A\cosh(B)\sinh(A)+144B\cosh(A)\sinh(B)$$
$$-A^3B^3\sinh(A)\sinh(B)+24A^2B^2\xi_1^2\cosh(A)$$
$$-16A^2B^2\xi_1^3\cosh(A)-48A^2B^2\xi_1^2\cosh(B)+32A^2B^2\xi_1^3\cosh(B)$$
$$-48A^2B^2\xi_2^2\cosh(A)+32A^2B^2\xi_2^3\cosh(A)+24A^2B^2\xi_2^2\cosh(B)$$
$$-16A^2B^2\xi_2^3\cosh(B)+144A^2\xi_1^2\cosh(A)\cosh(B)$$
$$-96A^2\xi_1^3\cosh(A)\cosh(B)+144AB\sinh(A\xi_1)\sinh(B)$$
$$+144B^2\xi_2^2\cosh(A)\cosh(B)-96B^2\xi_2^3\cosh(A)\cosh(B)$$
$$+144AB\sinh(B\xi_2)\sinh(A)-12A^3B^2\xi_1^2\sinh(A)+8A^3B^2\xi_1^3\sinh(A)$$
$$+6A^2B^3\xi_1^2\sinh(B)-4A^2B^3\xi_1^3\sinh(B)+6A^3B^2\xi_2^2\sinh(A)$$
$$-4A^3B^2\xi_2^3\sinh(A)-12A^2B^3\xi_2^2\sinh(B)+8A^2B^3\xi_2^3\sinh(B)$$
$$-72A^3\xi_1^2\cosh(B)\sinh(A)+48A^3\xi_1^3\cosh(B)\sinh(A)$$
$$-72B^3\xi_2^2\cosh(A)\sinh(B)+48B^3\xi_2^3\cosh(A)\sinh(B)$$
$$+288A\xi_1\xi_2\sinh(A)+24AB^2\xi_2\sinh(A\xi_1)+24A^2B\xi_1\sinh(B\xi_2)$$
$$+288B\xi_1\xi_2\sinh(B)+144A\xi_2\cosh(A\xi_1)\sinh(A)$$
$$-144A\xi_2\sinh(A\xi_1)\cosh(A)+288A\xi_1\cosh(B\xi_2)\sinh(A)$$
$$+144A\xi_2\sinh(A\xi_1)\cosh(B)+144B\xi_1\sinh(B\xi_2)\cosh(A)$$

$$
\begin{aligned}
&+288B\xi_2\cosh(A\xi_1)\sinh(B) + 144B\xi_1\cosh(B\xi_2)\sinh(B)\\
&-144B\xi_1\sinh(B\xi_2)\cosh(B) - 288AB\sinh(A)\sinh(B)\\
&-48AB^2\xi_1\sinh(A) - 120A^2B\xi_1\sinh(B) - 120AB^2\xi_2\sinh(A)\\
&-48A^2B\xi_2\sinh(B) + 24AB^2\cosh(A\xi_1)\sinh(A)\\
&-24AB^2\sinh(A\xi_1)\cosh(A) - 48AB^2\sinh(A\xi_1)\cosh(B)\\
&+144B\xi_1\cosh(A)\sinh(B) + 144A\xi_2\cosh(B)\sinh(A)\\
&-48A^2B\sinh(B\xi_2)\cosh(A) + 144A\cosh(A\xi_1)\cosh(B)\sinh(A)\\
&-144A\sinh(A\xi_1)\cosh(A)\cosh(B) + 24A^2B\cosh(B\xi_2)\sinh(B)\\
&-24A^2B\sinh(B\xi_2)\cosh(B) + 288B\cosh(A\xi_1)\cosh(A)\sinh(B)\\
&+288A\cosh(B\xi_2)\cosh(B)\sinh(A) + 144B\cosh(B\xi_2)\cosh(A)\sinh(B)\\
&-144B\sinh(B\xi_2)\cosh(A)\cosh(B) + 6AB^3\sinh(A\xi_1)\sinh(B)\\
&+6A^3B\sinh(B\xi_2)\sinh(A) - 32A^2B^2\xi_1\xi_2 - 48A^2\xi_1\xi_2\cosh(A)\\
&-48A^2\xi_1\xi_2\cosh(B) - 48B^2\xi_1\xi_2\cosh(A) - 48B^2\xi_1\xi_2\cosh(B)\\
&-96A^2\xi_1\cosh(B\xi_2)\cosh(A) + 48B^2\xi_2\cosh(A\xi_1)\cosh(A)\\
&+576\xi_1\xi_2\cosh(A)\cosh(B) + 48A^2\xi_1\cosh(B\xi_2)\cosh(B)\\
&-96B^2\xi_2\cosh(A\xi_1)\cosh(B) - 288B\sinh(A\xi_1)\sinh(A)\sinh(B)\\
&+288\xi_2\cosh(A\xi_1)\cosh(A)\cosh(B) - 288A\sinh(B\xi_2)\sinh(A)\sinh(B)\\
&+24A^3\xi_1\xi_2\sinh(A) + 24B^3\xi_1\xi_2\sinh(B) + 12A^3\xi_1\cosh(B\xi_2)\sinh(A)\\
&+288\xi_1\cosh(B\xi_2)\cosh(A)\cosh(B) + 144AB^2\cosh(B)\sinh(A)\\
&+144A^2B\cosh(A)\sinh(B) + 288\sinh(A\xi_1)\cosh(B)\sinh(A)\\
&-288\cosh(B\xi_2)\cosh(A)\cosh(B) + 12B^3\xi_2\cosh(A\xi_1)\sinh(B)\\
&-48B^2\xi_2\sinh(A\xi_1)\sinh(A) - 18AB^3\sinh(A)\sinh(B)\\
&-18A^3B\sinh(A)\sinh(B) - 48A^2\xi_1\sinh(B\xi_2)\sinh(B)\\
&-288\xi_2\sinh(A\xi_1)\cosh(B)\sinh(A) - 288\xi_1\sinh(B\xi_2)\cosh(A)\sinh(B)\\
&+24A^2B^2\xi_1\cosh(A) + 48A^2B^2\xi_1\cosh(B) + 48A^2B^2\xi_2\cosh(A)\\
&+24A^2B^2\xi_2\cosh(B) + 48A^2\xi_1\cosh(A)\cosh(B)\\
&+48B^2\xi_2\cosh(A)\cosh(B) - 96B^2\cosh(A\xi_1)\cosh(A)\cosh(B)\\
&-96A^2\cosh(B\xi_2)\cosh(A)\cosh(B) + 144A^2B\xi_1^2\sinh(B)\\
&-96A^2B\xi_1^3\sinh(B) - 6A^2B^3\xi_1\sinh(B) + 144AB^2\xi_2^2\sinh(A)\\
&-96AB^2\xi_2^3\sinh(A) - 6A^3B^2\xi_2\sinh(A) + 12A^3\xi_1\cosh(B)\sinh(A)\\
&+12B^3\xi_2\cosh(A)\sinh(B) + 12B^3\cosh(A\xi_1)\cosh(A)\sinh(B)\\
&+12A^3\cosh(B\xi_2)\cosh(B)\sinh(A) + 96B^2\sinh(A\xi_1)\cosh(B)\sinh(A)
\end{aligned}
$$

$$
\begin{aligned}
&+96A^2\sinh(B\xi_2)\cosh(A)\sinh(B) + 24A^2B^2\xi_1\xi_2^2 + 24A^2B^2\xi_1^2\xi_2 \\
&-16A^2B^2\xi_1\xi_2^3 - 16A^2B^2\xi_1^3\xi_2 + 144A^2\xi_1^2\xi_2\cosh(A) - 96A^2\xi_1^3\xi_2\cosh(A) \\
&+144A^2\xi_1^2\xi_2\cosh(B) + 144B^2\xi_1\xi_2^2\cosh(A) - 96A^2\xi_1^3\xi_2\cosh(B) \\
&-96B^2\xi_1\xi_2^3\cosh(A) + 144B^2\xi_1\xi_2^2\cosh(B) - 96B^2\xi_1\xi_2^3\cosh(B) \\
&-64A^2B^2\cosh(A)\cosh(B) - 12B^3\sinh(A\xi_1)\sinh(A)\sinh(B) \\
&-12A^3\sinh(B\xi_2)\sinh(A)\sinh(B) - 72A^3\xi_1^2\xi_2\sinh(A) \\
&+48A^3\xi_1^3\xi_2\sinh(A) - 72B^3\xi_1\xi_2^2\sinh(B) + 48B^3\xi_1\xi_2^3\sinh(B) \\
&+8A^2B^3\cosh(A)\sinh(B) + 8A^3B^2\cosh(B)\sinh(A) \\
&+288A\xi_1\sinh(B\xi_2)\sinh(A)\sinh(B) + 288B\xi_2\sinh(A\xi_1)\sinh(A)\sinh(B) \\
&-96AB^2\xi_1\cosh(B)\sinh(A) - 96A^2B\xi_1\cosh(A)\sinh(B) \\
&-96AB^2\xi_2\cosh(B)\sinh(A) - 96A^2B\xi_2\cosh(A)\sinh(B) \\
&+48AB^2\cosh(A\xi_1)\cosh(B)\sinh(A) - 48AB^2\sinh(A\xi_1)\cosh(A)\cosh(B) \\
&+48A^2B\cosh(B\xi_2)\cosh(A)\sinh(B) - 48A^2B\sinh(B\xi_2)\cosh(A)\cosh(B) \\
&+12AB^3\xi_1\sinh(A)\sinh(B) - 6A^3B\xi_1\sinh(A)\sinh(B) \\
&-6AB^3\xi_2\sinh(A)\sinh(B) + 12A^3B\xi_2\sinh(A)\sinh(B) \\
&-6AB^3\cosh(A\xi_1)\sinh(A)\sinh(B) + 6AB^3\sinh(A\xi_1)\cosh(A)\sinh(B) \\
&-6A^3B\cosh(B\xi_2)\sinh(A)\sinh(B) + 6A^3B\sinh(B\xi_2)\cosh(B)\sinh(A) \\
&-40A^2B^2\xi_1\xi_2\cosh(A) - 40A^2B^2\xi_1\xi_2\cosh(B) + 48A^2\xi_1\xi_2\cosh(A)\cosh(B) \\
&+48B^2\xi_1\xi_2\cosh(A)\cosh(B) + 96A^2\xi_1\cosh(B\xi_2)\cosh(A)\cosh(B) \\
&+96B^2\xi_2\cosh(A\xi_1)\cosh(A)\cosh(B) - 144AB^2\xi_1\xi_2^2\sinh(A) \\
&+96AB^2\xi_1\xi_2^3\sinh(A) + 2A^3B^2\xi_1\xi_2\sinh(A) - 144A^2B\xi_1^2\xi_2\sinh(B) \\
&+96A^2B\xi_1^3\xi_2\sinh(B) + 2A^2B^3\xi_1\xi_2\sinh(B) - 24A^3\xi_1\xi_2\cosh(B)\sinh(A) \\
&-24B^3\xi_1\xi_2\cosh(A)\sinh(B) - 12A^3\xi_1\cosh(B\xi_2)\cosh(B)\sinh(A) \\
&-12B^3\xi_2\cosh(A\xi_1)\cosh(A)\sinh(B) - 96A^2\xi_1\sinh(B\xi_2)\cosh(A)\sinh(B) \\
&-96B^2\xi_2\sinh(A\xi_1)\cosh(B)\sinh(A) + 48A^2B^2\xi_1\cosh(A)\cosh(B) \\
&+48A^2B^2\xi_2\cosh(A)\cosh(B) + 12A^3\xi_1\sinh(B\xi_2)\sinh(A)\sinh(B) \\
&+12B^3\xi_2\sinh(A\xi_1)\sinh(A)\sinh(B) - 144A^2B\xi_1^2\cosh(A)\sinh(B) \\
&+96A^2B\xi_1^3\cosh(A)\sinh(B) - 6A^2B^3\xi_1\cosh(A)\sinh(B) \\
&-144AB^2\xi_2^2\cosh(B)\sinh(A) + 96AB^2\xi_2^3\cosh(B)\sinh(A) \\
&-6A^3B^2\xi_2\cosh(B)\sinh(A) + 72A^3B\xi_1^2\sinh(A)\sinh(B) \\
&-48A^3B\xi_1^3\sinh(A)\sinh(B) + 72AB^3\xi_2^2\sinh(A)\sinh(B) \\
&-48AB^3\xi_2^3\sinh(A)\sinh(B) + 48A^2B^2\xi_1\xi_2^2\cosh(A) - 24A^2B^2\xi_1^2\xi_2\cosh(A)
\end{aligned}
$$

$$
\begin{aligned}
&-32A^2B^2\xi_1\xi_2^3\cosh(A) + 16A^2B^2\xi_1^3\xi_2\cosh(A) - 24A^2B^2\xi_1\xi_2^2\cosh(B)\\
&+48A^2B^2\xi_1^2\xi_2\cosh(B) + 16A^2B^2\xi_1\xi_2^3\cosh(B) - 32A^2B^2\xi_1^3\xi_2\cosh(B)\\
&-144A^2\xi_1^2\xi_2\cosh(A)\cosh(B) + 96A^2\xi_1^3\xi_2\cosh(A)\cosh(B)\\
&-144B^2\xi_1\xi_2^2\cosh(A)\cosh(B) + 96B^2\xi_1\xi_2^3\cosh(A)\cosh(B)\\
&-144AB\xi_1\sinh(B\xi_2)\sinh(A) - 144AB\xi_2\sinh(A\xi_1)\sinh(B)\\
&-6A^3B^2\xi_1\xi_2^2\sinh(A) + 12A^3B^2\xi_1^2\xi_2\sinh(A) + 4A^3B^2\xi_1\xi_2^3\sinh(A)\\
&-8A^3B^2\xi_1^3\xi_2\sinh(A) + 12A^2B^3\xi_1\xi_2^2\sinh(B) - 6A^2B^3\xi_1^2\xi_2\sinh(B)\\
&-8A^2B^3\xi_1\xi_2^3\sinh(B) + 4A^2B^3\xi_1^3\xi_2\sinh(B) + 72A^3\xi_1^2\xi_2\cosh(B)\sinh(A)\\
&-48A^3\xi_1^3\xi_2\cosh(B)\sinh(A) + 72B^3\xi_1\xi_2^2\cosh(A)\sinh(B)\\
&-48B^3\xi_1\xi_2^3\cosh(A)\sinh(B) + 48A^2B^2\xi_1^2\cosh(A)\cosh(B)\\
&-32A^2B^2\xi_1^3\cosh(A)\cosh(B) + 144AB\xi_1\sinh(A)\sinh(B)\\
&+48A^2B^2\xi_2^2\cosh(A)\cosh(B) - 32A^2B^2\xi_2^3\cosh(A)\cosh(B)\\
&+144AB\xi_2\sinh(A)\sinh(B) - 144AB\cosh(A\xi_1)\sinh(A)\sinh(B)\\
&+144AB\sinh(A\xi_1)\cosh(A)\sinh(B) - 144AB\cosh(B\xi_2)\sinh(A)\sinh(B)\\
&+144AB\sinh(B\xi_2)\cosh(B)\sinh(A) - 6A^2B^3\xi_1^2\cosh(A)\sinh(B)\\
&-24A^3B^2\xi_1^2\cosh(B)\sinh(A) + 4A^2B^3\xi_1^3\cosh(A)\sinh(B)\\
&+16A^3B^2\xi_1^3\cosh(B)\sinh(A) - 24A^2B^3\xi_2^2\cosh(A)\sinh(B)\\
&-6A^3B^2\xi_2^2\cosh(B)\sinh(A) + 16A^2B^3\xi_2^3\cosh(A)\sinh(B)\\
&+4A^3B^2\xi_2^3\cosh(B)\sinh(A) + 96AB^2\xi_1\xi_2\sinh(A)\\
&+96A^2B\xi_1\xi_2\sinh(B) + 3A^3B^3\xi_1^2\sinh(A)\sinh(B)\\
&-2A^3B^3\xi_1^3\sinh(A)\sinh(B) - 24AB^2\xi_2\cosh(A\xi_1)\sinh(A)\\
&+24AB^2\xi_2\sinh(A\xi_1)\cosh(A) - 288A\xi_1\xi_2\cosh(B)\sinh(A)\\
&+3A^3B^3\xi_2^2\sinh(A)\sinh(B) - 2A^3B^3\xi_2^3\sinh(A)\sinh(B)\\
&+48AB^2\xi_2\sinh(A\xi_1)\cosh(B) + 48A^2B\xi_1\sinh(B\xi_2)\cosh(A)\\
&-288B\xi_1\xi_2\cosh(A)\sinh(B) - 24A^2B\xi_1\cosh(B\xi_2)\sinh(B)\\
&+24A^2B\xi_1\sinh(B\xi_2)\cosh(B) - 144A\xi_2\cosh(A\xi_1)\cosh(B)\sinh(A)\\
&+144A\xi_2\sinh(A\xi_1)\cosh(A)\cosh(B) - 288A\xi_1\cosh(B\xi_2)\cosh(B)\sinh(A)\\
&-288B\xi_2\cosh(A\xi_1)\cosh(A)\sinh(B) - 144B\xi_1\cosh(B\xi_2)\cosh(A)\sinh(B)\\
&+144B\xi_1\sinh(B\xi_2)\cosh(A)\cosh(B) - 6AB^3\xi_2\sinh(A\xi_1)\sinh(B)\\
&-6A^3B\xi_1\sinh(B\xi_2)\sinh(A) - 48A^2B^2\xi_1\xi_2^2\cosh(A)\cosh(B)\\
&-48A^2B^2\xi_1^2\xi_2\cosh(A)\cosh(B) + 32A^2B^2\xi_1\xi_2^3\cosh(A)\cosh(B)\\
&+32A^2B^2\xi_1^3\xi_2\cosh(A)\cosh(B) + 144AB\xi_2\cosh(A\xi_1)\sinh(A)\sinh(B)
\end{aligned}
$$

$$
\begin{aligned}
&-144AB\xi_2\sinh(A\xi_1)\cosh(A)\sinh(B)+144AB\xi_1\cosh(B\xi_2)\sinh(A)\sinh(B)\\
&-144AB\xi_1\sinh(B\xi_2)\cosh(B)\sinh(A)+24A^2B^3\xi_1\xi_2^2\cosh(A)\sinh(B)\\
&+6A^2B^3\xi_1^2\xi_2\cosh(A)\sinh(B)+6A^3B^2\xi_1\xi_2^2\cosh(B)\sinh(A)\\
&+24A^3B^2\xi_1^2\xi_2\cosh(B)\sinh(A)-16A^2B^3\xi_1\xi_2^3\cosh(A)\sinh(B)\\
&-4A^2B^3\xi_1^3\xi_2\cosh(A)\sinh(B)-4A^3B^2\xi_1\xi_2^3\cosh(B)\sinh(A)\\
&-16A^3B^2\xi_1^3\xi_2\cosh(B)\sinh(A)-3A^3B^3\xi_1\xi_2^2\sinh(A)\sinh(B)\\
&-3A^3B^3\xi_1^2\xi_2\sinh(A)\sinh(B)+2A^3B^3\xi_1\xi_2^3\sinh(A)\sinh(B)\\
&+2A^3B^3\xi_1^3\xi_2\sinh(A)\sinh(B)+48AB^2\xi_1\xi_2\cosh(B)\sinh(A)\\
&+48A^2B\xi_1\xi_2\cosh(A)\sinh(B)-48AB^2\xi_2\cosh(A\xi_1)\cosh(B)\sinh(A)\\
&+48AB^2\xi_2\sinh(A\xi_1)\cosh(A)\cosh(B)-48A^2B\xi_1\cosh(B\xi_2)\cosh(A)\sinh(B)\\
&+48A^2B\xi_1\sinh(B\xi_2)\cosh(A)\cosh(B)+12AB^3\xi_1\xi_2\sinh(A)\sinh(B)\\
&+12A^3B\xi_1\xi_2\sinh(A)\sinh(B)+6AB^3\xi_2\cosh(A\xi_1)\sinh(A)\sinh(B)\\
&-6AB^3\xi_2\sinh(A\xi_1)\cosh(A)\sinh(B)+6A^3B\xi_1\cosh(B\xi_2)\sinh(A)\sinh(B)\\
&-6A^3B\xi_1\sinh(B\xi_2)\cosh(B)\sinh(A)-32A^2B^2\xi_1\xi_2\cosh(A)\cosh(B)\\
&+144AB^2\xi_1\xi_2^2\cosh(B)\sinh(A)+144A^2B\xi_1^2\xi_2\cosh(A)\sinh(B)\\
&-96AB^2\xi_1\xi_2^3\cosh(B)\sinh(A)-96A^2B\xi_1^3\xi_2\cosh(A)\sinh(B)\\
&-2A^2B^3\xi_1\xi_2\cosh(A)\sinh(B)-2A^3B^2\xi_1\xi_2\cosh(B)\sinh(A)\\
&-72AB^3\xi_1\xi_2^2\sinh(A)\sinh(B)-72A^3B\xi_1^2\xi_2\sinh(A)\sinh(B)\\
&+48AB^3\xi_1\xi_2^3\sinh(A)\sinh(B)+48A^3B\xi_1^3\xi_2\sinh(A)\sinh(B)\\
&+A^3B^3\xi_1\xi_2\sinh(A)\sinh(B))/D_C\,,
\end{aligned}
$$

$$
\begin{aligned}
N_2^1 = \quad & ((\xi_2-1)(12\sinh(A)-12\sinh(A\xi_1)+12\sinh(A(\xi_1-1))-12A\xi_1\\
&-12A\cosh(A)+2A^3\xi_1+12A\cosh(A(\xi_1-1))+2A^2\sinh(A\xi_1)\\
&+4A^2\sinh(A)-2A^3\xi_1^3+4A^2\sinh(A(\xi_1-1))+4A^3\xi_1\cosh(A)\\
&-12A^2\xi_1\sinh(A)-A^4\xi_1\sinh(A)-6A^3\xi_1^2\cosh(A)+2A^3\xi_1^3\cosh(A)\\
&+6A^2\xi_1^2\sinh(A)+2A^4\xi_1^2\sinh(A)-A^4\xi_1^3\sinh(A)+12A\xi_1\cosh(A)))\\
&/(D_A/L)\,,
\end{aligned}
$$

$$
\begin{aligned}
N_3^1 = \quad & ((\xi_1-1)(12\sinh(B)-12\sinh(B\xi_2)+12\sinh(B(\xi_2-1))-12B\xi_2\\
&-12B\cosh(B)+2B^3\xi_2+12B\cosh(B(\xi_2-1))+2B^2\sinh(B\xi_2)\\
&+4B^2\sinh(B)-2B^3\xi_2^3+4B^2\sinh(B(\xi_2-1))+4B^3\xi_2\cosh(B)\\
&-12B^2\xi_2\sinh(B)-B^4\xi_2\sinh(B)-6B^3\xi_2^2\cosh(B)+2B^3\xi_2^3\cosh(B)\\
&+6B^2\xi_2^2\sinh(B)+2B^4\xi_2^2\sinh(B)-B^4\xi_2^3\sinh(B)+12B\xi_2\cosh(B)))
\end{aligned}
$$

$/(D_B/W)\,,$

$$
\begin{aligned}
N_4^1 = \ & ((\xi_2-1)(6\sinh(A)-6\sinh(A\xi_1)-2A+6\sinh(A(\xi_1-1))+6A\xi_1 \\
& +2A\cosh(A\xi_1)-4A\cosh(A)-12A\xi_1^2+4A\xi_1^3+4A\cosh(A(\xi_1-1)) \\
& +A^2\sinh(A)+A^3\xi_1^2-A^3\xi_1^3+A^2\sinh(A(\xi_1-1))+12A\xi_1^2\cosh(A) \\
& -4A\xi_1^3\cosh(A)-A^3\xi_1\cosh(A)+4A^2\xi_1\sinh(A)+2A^3\xi_1^2\cosh(A) \\
& -A^3\xi_1^3\cosh(A)-9A^2\xi_1^2\sinh(A)+4A^2\xi_1^3\sinh(A)-6A\xi_1\cosh(A))) \\
& /(D_A/L^2)\,,
\end{aligned}
$$

$$
\begin{aligned}
N_5^1 = \ & ((\xi_1-1)(6\sinh(B)-6\sinh(B\xi_2)-2B+6\sinh(B(\xi_2-1))+6B\xi_2 \\
& +2B\cosh(B\xi_2)-4B\cosh(B)-12B\xi_2^2+4B\xi_2^3+4B\cosh(B(\xi_2-1)) \\
& +B^2\sinh(B)+B^3\xi_2^2-B^3\xi_2^3+B^2\sinh(B(\xi_2-1))+12B\xi_2^2\cosh(B) \\
& -4B\xi_2^3\cosh(B)-B^3\xi_2\cosh(B)+4B^2\xi_2\sinh(B)+2B^3\xi_2^2\cosh(B)- \\
& B^3\xi_2^3\cosh(B)-9B^2\xi_2^2\sinh(B)+4B^2\xi_2^3\sinh(B)-6B\xi_2\cosh(B))) \\
& /(D_B/W^2)\,.
\end{aligned}
$$

(E.1)

where

$$A = L\sqrt{d_1/d_4},\ B = W\sqrt{d_1/d_4},\ \xi_1 = x/L,\ \xi_2 = y/W\,, \tag{E.2}$$

with the terms in the denominators defined as

$$
\begin{aligned}
D_A = \ & (24A-24A\cosh(A)-4A^3-8A^3\cosh(A) \\
& +24A^2\sinh(A)+A^4\sinh(A))\,, \\
D_B = \ & (24B-24B\cosh(B)-4B^3-8B^3\cosh(B) \\
& +24B^2\sinh(B)+B^4\sinh(B))\,, \\
D_C = \ & (24\cosh(A)-24A\sinh(A)+4A^2+8A^2\cosh(A)-A^3\sinh(A)-24) \\
& (24\cosh(B)-24B\sinh(B)+4B^2+8B^2\cosh(B)-B^3\sinh(B)-24))\,.
\end{aligned}
\tag{E.3}
$$

Appendix F

STRAIN-DISPLACEMENT MATRICES FOR MSGT

The expression for the elements of the strain dislacement matrices $\boldsymbol{B}$ (3 x 20 in size) and $\boldsymbol{B}'$ (4 x 20 in size) are given in this section. Null elements are also indicated. $\boldsymbol{B}$ converges to the classical strain-displacement matrix, and $\boldsymbol{B}'$, i.e. the higher order strain-displacement matrix converges to zero, when l_0=l_1=l_2=0.

The strain-displacement matrix $\boldsymbol{B}$ similar to the classical counterpart and higher order strain-displacement matrix $\boldsymbol{B}'$ are given as below.

$$\boldsymbol{B} = \nabla_C \boldsymbol{N} = \begin{bmatrix} \boldsymbol{B}_1 & \boldsymbol{B}_2 & \boldsymbol{B}_3 & \boldsymbol{B}_4 \end{bmatrix} , \tag{F.1}$$

where

$$\boldsymbol{B}_j = \begin{bmatrix} \dfrac{\partial^2 N_1^j}{\partial x^2} & 0 & \dfrac{\partial^2 N_3^j}{\partial x^2} & 0 & \dfrac{\partial^2 N_5^j}{\partial x^2} \\ \dfrac{\partial^2 N_1^j}{\partial y^2} & \dfrac{\partial^2 N_2^j}{\partial y^2} & 0 & \dfrac{\partial^2 N_4^j}{\partial y^2} & 0 \\ 2\dfrac{\partial^2 N_1^j}{\partial x \partial y} & 2\dfrac{\partial^2 N_2^j}{\partial x \partial y} & 2\dfrac{\partial^2 N_3^j}{\partial x \partial y} & 2\dfrac{\partial^2 N_4^j}{\partial x \partial y} & 2\dfrac{\partial^2 N_5^j}{\partial x \partial y} \end{bmatrix} , \tag{F.2}$$

and

$$\boldsymbol{B}' = \nabla_H \boldsymbol{N} = \begin{bmatrix} \boldsymbol{B}'_1 & \boldsymbol{B}'_2 & \boldsymbol{B}'_3 & \boldsymbol{B}'_4 \end{bmatrix} , \tag{F.3}$$

where

$$
\boldsymbol{B}'_j = \begin{bmatrix}
\dfrac{\partial^3 N_1^j}{\partial x^3} & 0 & \dfrac{\partial^3 N_3^j}{\partial x^3} & 0 & \dfrac{\partial^2 N_5^j}{\partial x^3} \\[2ex]
3\dfrac{\partial^3 N_1^j}{\partial x^2 \partial y} & 0 & 3\dfrac{\partial^3 N_3^j}{\partial x^2 \partial y} & 0 & 3\dfrac{\partial^3 N_5^j}{\partial x^2 \partial y} \\[2ex]
3\dfrac{\partial^3 N_1^j}{\partial x \partial y^2} & 3\dfrac{\partial^3 N_2^j}{\partial x \partial y^2} & 0 & 3\dfrac{\partial^3 N_4^j}{\partial x \partial y^2} & 0 \\[2ex]
\dfrac{\partial^3 N_1^j}{\partial y^3} & \dfrac{\partial^3 N_2}{\partial y^3} & 0 & \dfrac{\partial^3 N_4^j}{\partial y^3} & 0
\end{bmatrix}. \tag{F.4}
$$

VITA

PERSONAL INFORMATION

Name and Surname:	Murat Kandaz
Nationality:	Turkish
Date of Birth:	21.05.1982
Place of Birth:	Ankara
Marital Status:	Married
Phone:	+90 532 773 71 85
email:	muratkandaz@gmail.com, e120093@metu.edu.tr

EDUCATION

Degree	**Institution**	**Year of Graduation**
M.Sc.	METU Mechanical Engineering	2006
B.Sc.	METU Mechanical Engineering	2003
High School	TED Ankara College	1999

EXPERIENCE

Years	**Company / Institution**	**Role**
2019-present	Numesys Advanced Engineering	Technical Manager
2018-2019	Enwave Australia	Project Manager
2016-2018	Tekfen Construction	Interface Manager
2010-2016	Calik Energy	Project Manager
2008-2009	AES-IC Energy	Lead Engineer
2005-2008	Calik Energy	Mechanical Engineer
2003-2005	BTC Pipeline Directorate	Mechanical Engineer

KEY PAPERS AND PRESENTATIONS

- M. Kandaz, H. Dal. Two novel Kirchhoff plate finite elements for the modified strain gradient theory. Proceedings in Applied Mathematics and Mechanics. 19, 1, doi.org/10.1002/pamm.201900194 (2019)

- M. Kandaz, H. Dal. A novel Kirchhoff plate finite element for the modified strain gradient theory. Submitted for Publication

- M. Kandaz, H. Dal. A comparative study of modified strain gradient theory and modified couple stress theory for gold microbeams. Archive of Applied Mechanics. 88, 11, pp 2051–2070 doi.org/10.1007/s00419-018-1436-0 (2018)

- H. Dal, M. Kandaz. Higher order beam and plate finite element models for analysis of microstructures. COMMAS Summer School, September 25-29, Stuttgart, Germany (2017)

- M. Kandaz, H. Dal, M. Unlu. Analysis of gold microbeams with higher order continuum theories. Proceedings in Applied Mathematics and Mechanics. 17, 1, pp 421, doi.org/10.1002/pamm.201710180 (2017)

- M. Kandaz. Powering up the future steps in Europe. PowerGen Europe, Cologne, Germany (2009)

- M. Kandaz. Load forecast of European countries. PowerGen Europe, Milano, Italy (2008)